

# Designing Mechanisms with Shape Memory Alloys and Permanent Magnets

by

Nicholas E. Kottenstette  
B.S., Mechanical Engineering (1995)  
The Catholic University of America

Submitted to the Department of Mechanical Engineering  
in Partial Fulfillment of the Requirements for the Degree of  
Master of Science

at the

Massachusetts Institute of Technology

February 1997

© 1997 Massachusetts Institute of Technology. All rights reserved.

Signature of Author .....

Department of Mechanical Engineering

February 4, 1997

Certified by .....

Woodie C. Flowers

Pappalardo Professor of Mechanical Engineering

Thesis Supervisor

Accepted by .....

Ain A. Sonin

Chairman, Department Committee on Graduate Students

MASSACHUSETTS INSTITUTE  
OF TECHNOLOGY

APR 16 1997

LIBRARIES



# Designing Mechanisms with Shape Memory Alloys and Permanent Magnets

by

Nicholas E. Kottenstette

Submitted to the Department of Mechanical Engineering  
on February 3, 1997, in Partial Fulfillment of the  
Requirements for the Degree of  
Master of Science

## ABSTRACT

A computer program has been created which assists an engineer to develop mechanisms which use Shape Memory Alloys (SMAs) and permanent magnets. The computer program simulates the following systems:

1. An electrically-heated  $\text{Ni}_{49}\text{Ti}_{51}$  wire actuating a constant force bias spring.
2. An electrically-heated  $\text{Ni}_{49}\text{Ti}_{51}$  wire actuating a linear bias spring.
3. A bi-stable mechanism employing  $\text{Ni}_{49}\text{Ti}_{51}$  wires and permanent magnets.

The simulations aid the engineer in creating reliable Shape Memory Alloy actuators for specific life-cycle and environmental temperature requirements.

Temperature-strain curves of three SMAs supplied by Dynalloy ( $\text{Ni}_{49}\text{Ti}_{51}$ ,  $\text{Ni}_{49}\text{Ti}_{44}\text{Hf}_7$  and  $\text{Ni}_{49}\text{Ti}_{44}\text{Cu}_7$ ) were experimentally obtained. The simulated temperature-strain curve for the  $\text{Ni}_{49}\text{Ti}_{51}$  wire approximately matched the experimental results, which led to the manufacturing predictions for Dynalloy's  $\text{Ni}_{49}\text{Ti}_{51}$  SMAs. The  $\text{Ni}_{49}\text{Ti}_{44}\text{Hf}_7$  wires shrank only 1.5% (4% shrink was expected) and their Martensite Finish temperature was no greater than that of the  $\text{Ni}_{49}\text{Ti}_{51}$  wires.

Life-cycle tests were performed on  $\text{Ni}_{49}\text{Ti}_{51}$  wire at an actuating stress of 160 MPa. Two  $\text{Ni}_{49}\text{Ti}_{51}$  wires cycled approximately 1,000,000 times under a 160 MPa stress; however, using the same apparatus, two other  $\text{Ni}_{49}\text{Ti}_{51}$  wires cycled approximately 10,000 times under the same 160 MPa stress.

Experimental force-gap curves were obtained for Ceramic, Samarium Cobalt, Neodymium Iron Boron, and Bonded Neodymium Iron Boron magnets. These experimental curves were used to create 2 correction factors for future force-gap curve simulations.

Thesis Supervisor: Woodie C. Flowers  
Pappalardo Professor of Mechanical Engineering

## **Acknowledgments**

My wife,  
Maryellen Kottenstette

Professor Woodie Flowers

DEKA Research and Development

Gustavo Buhacoff

Dr. Kingston Owens

Professor Frank McClintock

Professor David Trumper

Professor Anuradha Annaswamy

Raymond Hardin

Michael Bush

My parents,  
Mary and Eugene Kottenstette Jr.

# Designing Mechanisms with Shape Memory Alloys and Permanent Magnets

List of Figures .....	7
List of Tables .....	12
1 Shape Memory Alloys and permanent magnets .....	13
1.1 An introduction to Shape Memory Alloys .....	14
1.2 An introduction to permanent magnets .....	18
2 Modeling SMA-actuated systems .....	23
2.1 Modeling an electrically-heated Ni <sub>49</sub> Ti <sub>51</sub> wire actuating a constant force bias spring .....	24
2.2 Modeling an electrically-heated Ni <sub>49</sub> Ti <sub>51</sub> wire actuating a linear bias spring .....	26
2.3 Modeling a bi-stable mechanism employing Ni <sub>49</sub> Ti <sub>51</sub> wires and permanent magnets .....	28
3 Computer simulations of SMA-actuated systems .....	34
3.1 Simulation of an electrically-heated Ni <sub>49</sub> Ti <sub>51</sub> wire actuating a constant force bias spring .....	34
3.2 Simulation of an electrically-heated Ni <sub>49</sub> Ti <sub>51</sub> wire actuating a linear bias spring .....	39
3.3 Simulation of a bi-stable mechanism employing Ni <sub>49</sub> Ti <sub>51</sub> wires and permanent magnets .....	44
4 Conclusions and Recommendations .....	51
Appendix A: Users Manual for Design Program .....	53
Appendix B: Modeling Shape Memory Alloys .....	78
Appendix C: Shape Memory Alloy Experiments and Results .....	105

Appendix D: Model for Permanent Magnets . . . . .	129
Appendix E: Permanent Magnet Experiments and Results . . . . .	151
Bibliography . . . . .	161

<b>Figure</b>	<b>Page</b>
Figure 1.	Stress-strain curve for SMAs consisting of Nickel and Titanium . . . 15
Figure 2.	Arrangement required to create a SMA which can contract and elongate without being plastically deformed . . . . . 16
Figure 3.	Half of a Samarium Cobalt magnet and a low-carbon steel torus . . . 19
Figure 4.	B-H curves for Samarium Cobalt and low-carbon steel . . . . . 20
Figure 5.	An electrically-heated Ni <sub>49</sub> Ti <sub>51</sub> wire actuating a constant force bias spring . . . . . 24
Figure 6.	An electrically-heated Ni <sub>49</sub> Ti <sub>51</sub> wire actuating a linear bias spring . . 26
Figure 7.	A bi-stable mechanism employing Ni <sub>49</sub> Ti <sub>51</sub> wires and permanent magnets . . . . . 28
Figure 8.	Simulated and experimental temperature-position curves for a 4.3 MPa biased Flexinol 90-110 wire . . . . . 35
Figure 9.	Simulated and experimental temperature-position curves for a 47.3 MPa biased Flexinol 90-110 wire . . . . . 36
Figure 10.	Simulated and experimental temperature-position curves for a 86.0 MPa biased Flexinol 90-110 wire . . . . . 37
Figure 11.	Simulated and experimental temperature-position curves for a 150.4 MPa biased Flexinol 90-110 wire . . . . . 38
Figure 12.	Simulated temperature-time curve for Ni <sub>49</sub> Ti <sub>51</sub> wire . . . . . 40
Figure 13.	Simulated length-time curve for Ni <sub>49</sub> Ti <sub>51</sub> wire . . . . . 41
Figure 14.	Simulated stress-time curve for Ni <sub>49</sub> Ti <sub>51</sub> wire . . . . . 42
Figure 15.	Simulated temperature-strain curve for Ni <sub>49</sub> Ti <sub>51</sub> wire . . . . . 43
Figure 16.	Simulated magnetic force-gap curve for Samarium Cobalt . . . . . 44
Figure 17.	Resulting magnetic torque-angular position curve from Samarium Cobalt pendulum . . . . . 45
Figure 18.	Simulated angular position-time curve for steel lever . . . . . 47
Figure 19.	Simulated stress-time curve for Ni <sub>49</sub> Ti <sub>51</sub> wire (wire 2) . . . . . 48
Figure 20.	Simulated temperature-strain curve for Ni <sub>49</sub> Ti <sub>51</sub> wire (wire 1) . . . 49
Figure A1.	An electrically-heated Ni <sub>49</sub> Ti <sub>51</sub> wire actuating a constant force bias spring . . . . . 54
Figure A2.	Design menu used to simulate an electrically-heated Ni <sub>49</sub> Ti <sub>51</sub> wire . . 55
Figure A3.	The “Flexinol 90-110 Wires” screen . . . . . 57
Figure A4.	The “Mondo-tronics Ribbon Wires” screen . . . . . 58

<b>Figure</b>	<b>Page</b>
Figure A5.	The “Create Your Own Wires” screen . . . . . 59
Figure A6.	The “Create Force History” screen (constant force bias option) . . . 60
Figure A7.	Simulated temperature-strain curve for Ni <sub>49</sub> Ti <sub>51</sub> wire . . . . . 61
Figure A8.	An electrically-heated Ni <sub>49</sub> Ti <sub>51</sub> wire actuating a linear bias spring . . 62
Figure A9.	The “Create Force History” screen (linear spring bias option) . . . . 63
Figure A10.	Simulated stress-time curve for Ni <sub>49</sub> Ti <sub>51</sub> wire . . . . . 64
Figure A11.	A bi-stable mechanism employing Ni <sub>49</sub> Ti <sub>51</sub> wires and permanent magnets . . . . . 65
Figure A12.	Main menu used to simulate a bi-stable mechanism employing Ni <sub>49</sub> Ti <sub>51</sub> wires and permanent magnets . . . . . 66
Figure A13.	The “SMA Wires” screen . . . . . 67
Figure A14.	The “Bias Springs” screen . . . . . 68
Figure A15.	The “Assembly Dimensions” screen . . . . . 69
Figure A16.	The “Magnet and Friction Torque” screen . . . . . 70
Figure A17.	Magnetic torque-angular position and normal force-angular position curves . . . . . 71
Figure A18.	The “Heating The Wires” screen . . . . . 72
Figure A19.	Electrical square wave to heat Ni <sub>49</sub> Ti <sub>51</sub> wires . . . . . 73
Figure A20.	The “Lever Inertia” screen . . . . . 74
Figure A21.	The “Plot Results” screen . . . . . 75
Figure A22.	Simulated angular position-time curve for steel lever . . . . . 77
Figure B1.	Generalized model for a Shape Memory Alloy . . . . . 78
Figure B2.	Thermal conductivity-temperature curve for air . . . . . 80
Figure B3.	Prandtl-temperature curve for air . . . . . 81
Figure B4.	Curve relating $\log_{10}(g\beta/v^2)$ to temperature for air . . . . . 82
Figure B5.	Temperature-strain curve model for a SMA . . . . . 84
Figure B6.	Experimental temperature-strain curve of a 4.3 MPa biased Ni <sub>49</sub> Ti <sub>51</sub> wire . . . . . 86
Figure B7.	Experimental temperature-strain curve of a 47.3 MPa biased Ni <sub>49</sub> Ti <sub>51</sub> wire . . . . . 87
Figure B8.	Experimental temperature-strain curve of a 86.0 MPa biased Ni <sub>49</sub> Ti <sub>51</sub> wire . . . . . 88

<b>Figure</b>	<b>Page</b>
Figure B9. Experimental temperature-strain curve of a 150.4 MPa biased Ni <sub>49</sub> Ti <sub>51</sub> wire . . . . .	89
Figure B10. Experimental temperature-strain curve of a 4.3 MPa biased Ni <sub>49</sub> Ti <sub>44</sub> Cu <sub>7</sub> wire . . . . .	90
Figure B11. Experimental temperature-strain curve of a 43.0 MPa biased Ni <sub>49</sub> Ti <sub>44</sub> Cu <sub>7</sub> wire . . . . .	91
Figure B12. Experimental temperature-strain curve of a 86.0 MPa biased Ni <sub>49</sub> Ti <sub>44</sub> Cu <sub>7</sub> wire . . . . .	92
Figure B13. Experimental temperature-strain curve of a 150.4 MPa biased Ni <sub>49</sub> Ti <sub>44</sub> Cu <sub>7</sub> wire . . . . .	93
Figure B14. Transformation temperatures-stress curves (Ms, Mf, As, Af) for Ni <sub>49</sub> Ti <sub>51</sub> wire . . . . .	94
Figure B15. Austenite finish temperature-cycle curves for Ni <sub>49</sub> Ti <sub>51</sub> wires with different heat-treatments . . . . .	95
Figure B16. Martensite start temperature-cycle curves for Ni <sub>49</sub> Ti <sub>51</sub> wires with different heat-treatments . . . . .	96
Figure B17. Unrecovered strain-stress curve for Ni <sub>49</sub> Ti <sub>51</sub> wire . . . . .	98
Figure B18. Shrink loss-cycle curve for Ni <sub>49</sub> Ti <sub>51</sub> wire . . . . .	99
Figure B19. Creep-cycle curves of Ni <sub>49</sub> Ti <sub>51</sub> wires (400°C, 425°C and 600°C heat-treatments) under 69.0 Mpa . . . . .	101
Figure B20. Creep-cycle curves of Ni <sub>49</sub> Ti <sub>51</sub> wires (400°C, 425°C and 600°C heat-treatments) under 207.0 MPa . . . . .	102
Figure B21. Contraction-cycle curve for pre-creeped Ni <sub>49</sub> Ti <sub>51</sub> wire under 69.0 MPa. . . . .	103
Figure C1. Experimental apparatus used to obtain temperature-strain curves . . .	106
Figure C2. Experimental temperature-strain curve of a 4.3 MPa biased Ni <sub>49</sub> Ti <sub>51</sub> wire . . . . .	110
Figure C3. Experimental temperature-strain curve of a 47.3 MPa biased Ni <sub>49</sub> Ti <sub>51</sub> wire . . . . .	111
Figure C4. Experimental temperature-strain curve of a 86.0 MPa biased Ni <sub>49</sub> Ti <sub>51</sub> wire . . . . .	112

<b>Figure</b>	<b>Page</b>
Figure C5. Experimental temperature-strain curve of a 150.4 MPa biased Ni <sub>49</sub> Ti <sub>51</sub> wire . . . . .	113
Figure C6. Transformation temperatures-stress curves (Ms, Mf, As, Af) for Ni <sub>49</sub> Ti <sub>51</sub> wire . . . . .	114
Figure C7. Experimental temperature-strain curve of a 4.3 MPa biased Ni <sub>49</sub> Ti <sub>44</sub> Cu <sub>7</sub> wire . . . . .	116
Figure C8. Experimental temperature-strain curve of a 43.0 MPa biased Ni <sub>49</sub> Ti <sub>44</sub> Cu <sub>7</sub> wire . . . . .	117
Figure C9. Experimental temperature-strain curve of a 86.0 MPa biased Ni <sub>49</sub> Ti <sub>44</sub> Cu <sub>7</sub> wire . . . . .	118
Figure C10. Experimental temperature-strain curve of a 150.4 MPa biased Ni <sub>49</sub> Ti <sub>44</sub> Cu <sub>7</sub> wire . . . . .	119
Figure C11. Transformation temperatures-stress curves (Ms, Mf, As, Af) for Ni <sub>49</sub> Ti <sub>44</sub> Cu <sub>7</sub> wire . . . . .	120
Figure C12. Experimental temperature-strain curve of a 4.3 MPa biased Ni <sub>49</sub> Ti <sub>44</sub> Hf <sub>7</sub> wire . . . . .	122
Figure C13. Experimental temperature-strain curve of a 150.4 MPa biased Ni <sub>49</sub> Ti <sub>44</sub> Hf <sub>7</sub> wire . . . . .	123
Figure C14. Experimental apparatus used for life-cycle testing of a Ni <sub>49</sub> Ti <sub>51</sub> wire . . . . .	124
Figure C15. Digital electronic circuit used to thermally cycle Ni <sub>49</sub> Ti <sub>51</sub> wire . . . . .	125
Figure C16. Adjustable voltage supply used to electrically heat Ni <sub>49</sub> Ti <sub>51</sub> wire . . . . .	125
Figure D1. Magnetic fields of a permanent magnet located in free-space and on a steel block . . . . .	130
Figure D2. Demagnetization curves for permanent magnets . . . . .	133
Figure D3. Force-gap curves for Samarium Cobalt . . . . .	138
Figure D4. Force-gap curves for Neodymium Iron Boron . . . . .	139
Figure D5. Force-gap curves for Ceramic 5 . . . . .	140
Figure D6. Force-gap curves for Ceramic 8 . . . . .	141
Figure D7. Force-gap curves for Bonded Neodymium Iron Boron . . . . .	142
Figure D8. Experimental relationship between Cf <sub>1</sub> and D <sub>M</sub> /L <sub>M</sub> . . . . .	144
Figure D9. Experimental relationship between Cf <sub>2</sub> and D <sub>M</sub> /L <sub>M</sub> . . . . .	145
Figure D10. Corrected force-gap curves for Samarium Cobalt . . . . .	146

<b>Figure</b>	<b>Page</b>
Figure D11. Corrected force-gap curves for Neodymium Iron Boron . . . . .	147
Figure D12. Corrected force-gap curves for Ceramic 5 . . . . .	148
Figure D13. Corrected force-gap curves for Ceramic 8 . . . . .	149
Figure D14. Corrected force-gap curves for Bonded Neodymium Iron Boron . .	150
Figure E1. Experimental apparatus used for testing permanent magnets . . . . .	152
Figure E2. Experimental force-gap curve for Samarium Cobalt . . . . .	156
Figure E3. Experimental force-gap curve for Neodymium Iron Boron . . . . .	157
Figure E4. Experimental force-gap curve for Ceramic 5 . . . . .	158
Figure E5. Experimental force-gap curve for Ceramic 8 . . . . .	159
Figure E6. Experimental force-gap curve for Bonded Neodymium Iron Boron . . . . .	160

<b>Table</b>	<b>Page</b>
Table C1.	Experimental temperature-contraction results for Ni <sub>49</sub> Ti <sub>51</sub> wire . . . . 109
Table C2.	Experimental temperature-contraction results for Ni <sub>49</sub> Ti <sub>44</sub> Cu <sub>7</sub> wire. . 115
Table C3.	Experimental temperature-contraction results for Ni <sub>49</sub> Ti <sub>44</sub> Hf <sub>7</sub> wire. . 121
Table D1.	Residual flux densities and coercivities of permanent magnets . . . . 134
Table E1.	Experimental force-gap results for permanent magnets . . . . . 155

# 1 Shape Memory Alloys and permanent magnets

Shape Memory Alloys (SMAs) and permanent magnets are non-linear materials which can be described by hysteresis loops. Together, they can be used to form bi-stable mechanisms. SMAs can be electrically heated in order to move a permanent magnet between two stable states. Figure 7 illustrates a bi-stable mechanism in which two SMA wires are used to toggle a steel lever which is biased by a permanent magnet pendulum. The bi-stable mechanism utilizes the magnet's constant holding force capabilities, and the SMAs' actuating capabilities. The mechanism is energy efficient, because it eliminates the need for the SMA to be continuously heated in order to maintain a specific position. In order to simulate the bi-stable mechanism, methods to simulate SMAs and permanent magnets will be developed.

Shape Memory Alloys are alloys which, when properly manufactured, can contract and elongate approximately 4% of their initial length. This ability to contract and elongate allows SMAs to be used as actuators. In order for reliable SMA actuators to be developed, the engineer needs to be aware of the limitations associated with SMAs. For example, a properly designed SMA actuator will operate with environmental temperatures no greater than 50°C. These and other limitations of SMAs are discussed as this document shows how to simulate the following systems:

1. An electrically-heated  $\text{Ni}_{49}\text{Ti}_{51}$  wire actuating a constant force bias spring.
2. An electrically-heated  $\text{Ni}_{49}\text{Ti}_{51}$  wire actuating a linear bias spring.
3. A bi-stable mechanism employing  $\text{Ni}_{49}\text{Ti}_{51}$  wires and permanent magnets.

$\text{Ni}_{49}\text{Ti}_{51}$  wires are a primary SMA used in industry. The system simulations shown above are performed using the software package MATLAB<sup>®</sup>. These simulations illustrate how to manufacture  $\text{Ni}_{49}\text{Ti}_{51}$  wire, perform life cycle analysis, and tolerance studies on the systems. Section 1.1 provides a more detailed discussion of SMAs.

Permanent magnets are in many of the products people use. Permanent magnets can be found in speakers, electric motors for VCRs and blenders, on credit cards and on refrigerators holding up memos. This document discusses how to determine the resulting permanent magnetic holding force on a refrigerator with a low-carbon steel shell. It shows

how the holding force changes when various non-magnetic items with different thicknesses are placed between the permanent magnet and the refrigerator. It will show that, for the appropriate holding force to be obtained, the steel shell requires a minimum thickness in order to avoid magnetic saturation. Section 1.2 provide a more detailed discussion of this problem.

### **1.1 *An introduction to Shape Memory Alloys***

In the 1960s Buehler and Wiley invented the Shape Memory Alloy NiTiNOL (Nickel Titanium Naval Ordnance Laboratories); however, significant research involving SMAs did not occur until the early 90s. Baz (1990), Liang and Rogers (1990) began to investigate the dynamic behavior and modeling of SMAs. Thoma (1992) wrote a paper on manufacturing stable SMA wires consisting of  $\text{Ni}_{49}\text{Ti}_{51}$ . Baz developed an empirical dimensionless model to determine the resulting thermal time constants, and maximum displacement of a spring and mass biased actuator. Liang and Rogers developed a constitutive model for the phase transformation dynamics and stress-strain-temperature relations for SMAs. Thoma discussed the SMAs' changing properties due to cycling under an applied stress. Appendix B incorporates the work of Thoma, Liang and Rogers, along with recent experimental results (Appendix C), in order to develop a more complete dynamic model for  $\text{Ni}_{49}\text{Ti}_{51}$  wires.

A Shape Memory Alloy is an alloy which can be transformed between two phases by changing its temperature. The phase transformation occurs at temperatures which are below the recrystallization temperature. The two phases are known as the Martensite phase and Austenite phase. Figure 1 shows the resulting stress-strain history for a SMA consisting of Nickel and Titanium.

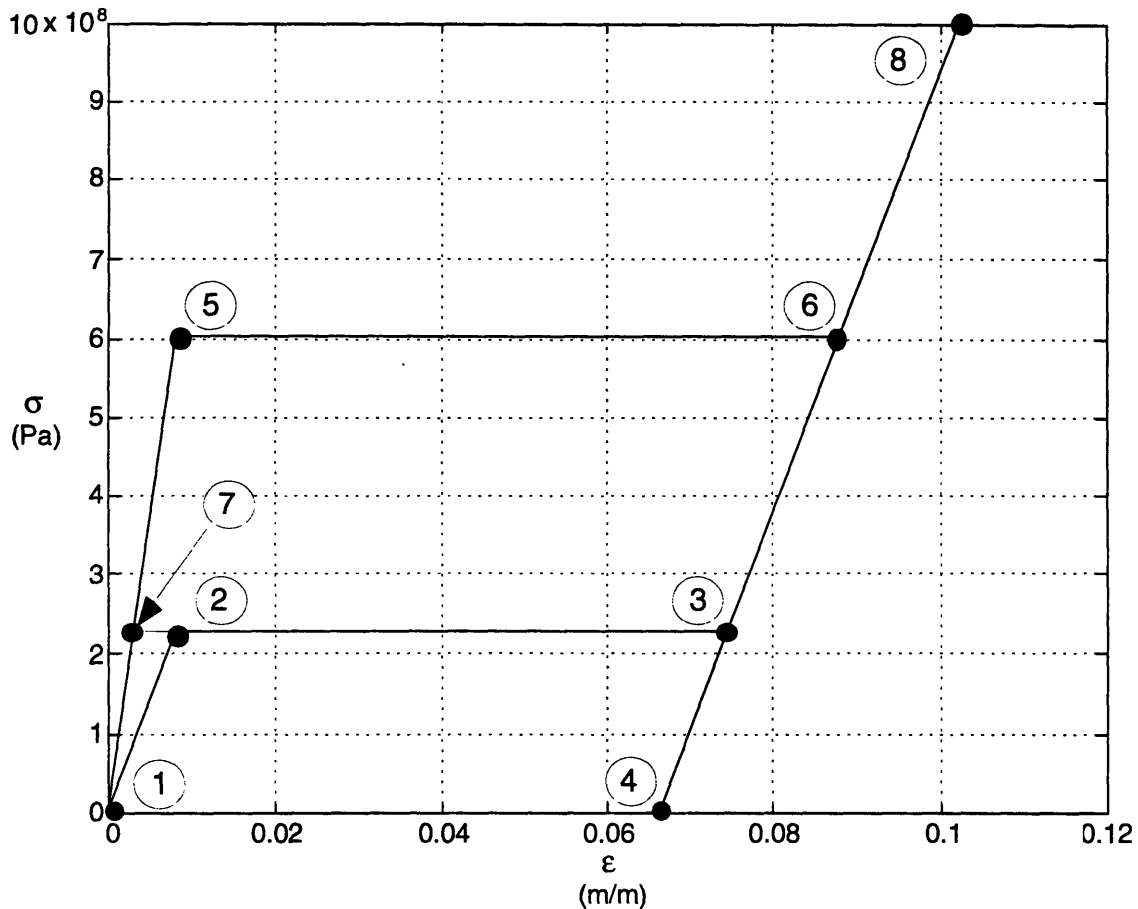


Figure 1. Stress-strain curve for SMAs consisting of Nickel and Titanium.

When the SMA is in its Martensite phase, it can be strained from point 1 to point 2, at which point the wire yields at 224 MPa with a strain of .008 m/m (note the SMAs' Young's modulus is 28 GPa). The SMA is further strained to point 3 (.0746 m/m) under a near constant stress (224 MPa). The SMA is then released as it recovers to point 4 with a final unrecoverable strain of .066 m/m. When the SMA is heated to its Austenite phase, the deformed SMA will recover the plastic strain from point 4 to point 1. When the SMA is in its Austenite phase it is in a super-elastic state. The SMA can be stretched from point 1 to point 5 at which point the wire yields at 600 MPa with a strain of .008 m/m (note the SMAs' Young's modulus is 75 GPa). The SMA continues to be strained under a constant 600 MPa stress until the strain is .088 m/m at point 6. The stress in the SMA is reduced in order for the wire to return to point 3 (note the SMAs' Young's modulus is now at 28 GPa because it is in a stress-induced Martensitic state). As the stress continues to be reduced, the SMA recovers its strain to point 7, and then to point 1 (in which the SMAs Young's modulus is now 75 GPa because it is no longer in a stress-induced Martensitic state). So

long as the SMA remains in its Austenite phase, it can be continually cycled from points 1 to 5 to 6 to 3 to 7 to 1. Point 8 represents the ultimate strength of the SMA before it breaks (1,000 MPa). This curve was approximated by information given by Gilbertson (1994), in which the maximum recovery stress (600 MPa), Martensite Young's modulus (28 GPa), Austenite Young's modulus (75 GPa) and the ultimate stress (1,000 MPa) are given. The Martensite yield stress was estimated by multiplying the yield strain of the Austenite by the Young's modulus of the Martensite. The behavior of the stress-strain curve is based on an article written by Wayman (1993). Figure 2 illustrates the arrangement required to create a Shape Memory Alloy which can contract and elongate without needing to be plastically deformed.

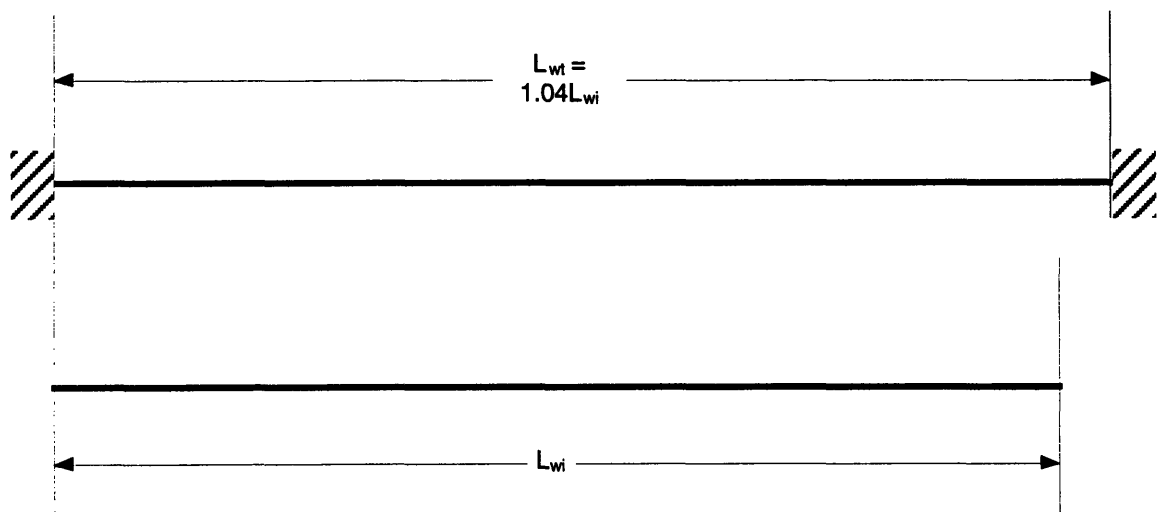


Figure 2. Arrangement required to create a SMA which can contract and elongate without being plastically deformed.

In its Martensite state, a SMA wire is elongated to a total length ( $L_{wt}$ ) which is approximately 4% of its initial length ( $L_{wi}$ ). The deformed wire is then constrained at both ends. The constrained wire is then heated to its Austenite finish temperature. Since the wire is constrained, it is unable to recover and remains in a stress-induced Martensite state. The wire is then cooled to below its Martensite finish temperature at which point it “remembers” its former stress-induced Martensite state. This heating and cooling of the constrained wire should be repeated approximately five more times. After the training is complete, the SMA is now capable of shrinking to  $L_{wi}$  and elongating 4% to  $L_{wt}$  with a 70 MPa bias stress.

This process generates in-built microstresses in the parent phase that in turn program the specimen to behave as in a stress-induced Martensitic transformation. That is, the microstresses favor only a single orientation of Martensite on subsequent cooling, which produces a spontaneous deformation.

- Wayman (1990)

There are over 10,000 United States patents on SMAs and their applications. Few of these patents have resulted in viable products.

- Zhang, Zee and Thoma (1996)

Some successful products are superelastic eyeglass frames, pipe couplings, and orthodontic arch wires. The eye glass frames can be bent around a finger and still return to their initial state. The pipe couplings, manufactured by Raychem, are shipped in liquid nitrogen in a deformed Martensitic state (point 4 of Figure 1). The coupling is then removed and placed around two pipes to be connected. As the coupling warms, it transforms into Austenite and attempts to recover to point 1 of Figure 1. If the pipes are the correct size, the superelastic coupling will still remain strained under a 224 MPa stress. This principle has also been applied to electrical connectors. The superelastic orthodontic arch wires are able to provide a constant bias stress in the patient's mouth as it changes shape, thus reducing the need for adjustments.

No high life cycle (over 10,000 cycles) SMA actuator currently exists which has made any significant market impact.

Failure in the application of SMAs is primarily due to the lack of knowledge of many scientists and engineers on the limitations of SMAs and how to process SMAs to achieve long lived and stable SMA members.

- Zhang, Zee and Thoma (1996)

The simulation programs presented address these limitations and enable engineers to design high life cycle SMA actuators.

## 1.2 *An introduction to permanent magnets*

Permanent magnetism has been observed since the Greeks discussed the repelling and attractive properties of magnes, otherwise known as a lodestone ( $\text{Fe}_3\text{O}_4$ ), which was discovered in Magnesia, an ancient city in Asia Minor. Some authors who have published texts specifically on permanent magnet design are Parker (1962), Moskowitz (1995), McCaig (1977) and Campbell (1994). Livingston (1996) provides numerous examples of permanent magnet applications. In his fifth edition of *Electric Machinery*, Fitzgerald (1990) introduced two new sections which provide a method for relating permanent magnetic fields to resulting mechanical torque and forces. The method introduces a fictitious coil wrapped around a permanent magnet which can reduce the flux density to zero. This enables the magnetic field energy and corresponding forces to be determined. Fitzgerald's method is applied to determine the magnetic pulling force on a steel block. The theoretical results are compared to experimental results in Appendix D. Two correction factors are determined in order to match the theoretical results to the experimental results.

The flux density ( $B$ ) and magnetizing force ( $H$ ) are used to describe magnetic materials. The flux density is the ratio of the total flux ( $\phi$ ) to the cross-sectional area through which it passes. The magnetizing force is the ratio of the mean magnetomotive force (mmf) to a given length of a closed path. The product of the flux (Webers) and the magnetomotive force (Ampere-turns) results in energy (Joules); hence, the product of  $B$  (Weber/m<sup>2</sup> or Tesla) with  $H$  (Ampere-turns/m) results in energy per unit volume (Joules/m<sup>3</sup>). Figure 3 shows a torus in which one half is a Samarium Cobalt magnet and the other half is a low carbon steel torus. Figure 4 illustrates their corresponding  $B$ - $H$  curves. Equations D1 and D2 are used to relate the flux density and magnetizing force of the permanent magnet to the low carbon steel.

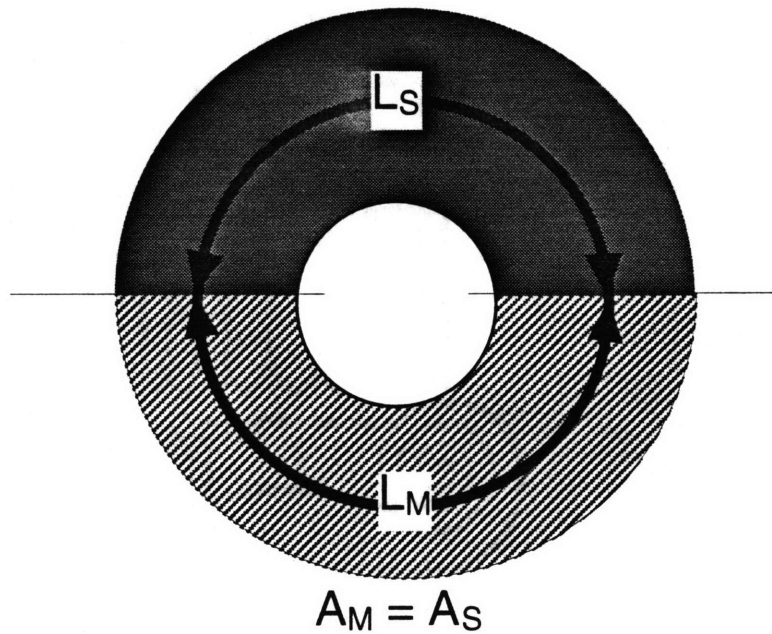


Figure 3. Half of a Samarium Cobalt magnet and a low-carbon steel torus.

The length of the flux path in the magnet is equal to the length of the flux path in the steel; hence, equation D1 implies that the magnetizing force of the magnet is equal to the negative magnetizing force of the steel. The cross-sectional area of the magnet is equal to the cross-sectional area of the steel; hence, equation D2 implies that the flux density of the magnet is equal to the flux density of the steel.

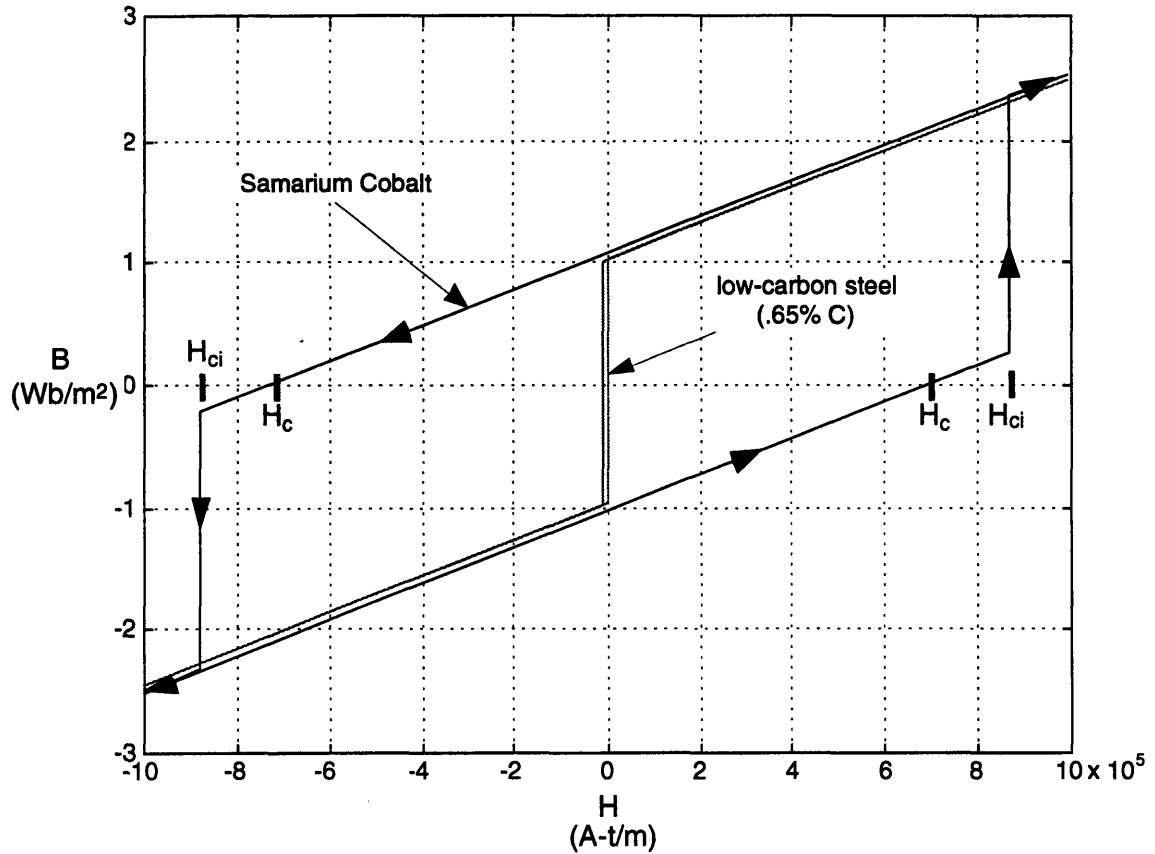


Figure 4. B-H curves for Samarium Cobalt and low-carbon steel.

Using the results from equations D1 and D2 in conjunction with B-H curves of Figure 4, the resulting flux density and magnetizing force for the permanent magnet and low carbon steel are as follows:

- $B_M = B_S = 1.025$  Tesla
- $H_M = -H_S = -17.0$  kA/m

Note that the results indicate that the steel became saturated. When the steel is unsaturated it can possess a flux density up to 1.0 Tesla with a corresponding magnetizing force of 3.33 kA/m. The flux density in this example has increased only by 2.5%; however, the resulting magnetizing force has increased by 410%. In order to maximize the flux density in a permanent magnet the magnetizing force needs to be minimized. In order to minimize the magnetizing force, the flux of the magnet needs to be directed by a “soft magnetic

material” (for example, a low-carbon steel torus). The “soft magnetic material” can not become saturated by the flux. This can be accomplished by making the cross sectional area of the “soft magnetic material” approximately equal to the cross-sectional area of the permanent magnet.

Figure 4 indicates two additional variables which define the shape of the curves: the coercivity ( $H_c$ ) and the intrinsic coercivity ( $H_{ci}$ ). A third variable, the remanent magnetization ( $B_r$ ), is also used to define the shape of the curves. The coercivity is the magnetizing force in which the flux density is zero. The intrinsic coercivity is the magnetizing force required to reverse the polarization of the magnet. The remanent magnetization is the flux density when the magnetizing force is zero. The arrows in Figure 4 indicate the path dependency of the magnetic hysteresis loop. For example, the polarity of the magnet in Figure 3 is reversed as follows:

1. The magnet has the following flux density and magnetizing force:
  - $B_M = 1.025$  Tesla
  - $H_M = -17.0$  kA/m (second quadrant)
  
2. A coil is wrapped around the magnet:
  - the coil has 10,000 turns
  - $L_M = .01$  meters
  - 1 Amp flowed through the coil
  - The resulting magnetizing force ( $H_M$ ) was -1,000 kA-turns/m
  - This magnetizing force is greater than the intrinsic coercivity; hence, the magnetic polarity was reversed.
  
3. The current was then brought back to 0 Amps leaving the magnet with the following values:
  - $B_M = -1.025$  Tesla
  - $H_M = 17.0$  kA/m (fourth quadrant)

Figure 4 indicates that the intrinsic coercivity equals the coercivity for the steel bar. Alnico magnets have a similar problem; hence, they will not be tested. Ceramic 5, Ceramic 8, Neodymium Iron Boron and Bonded Neodymium Iron Boron magnets have hysteresis

loops similar to the Samarium Cobalt magnet (linear in the second quadrant); hence, these magnets will be tested and compared. The predicted theoretical results and correction factors for these permanent magnets are discussed in Appendix D. The experimental permanent magnet pulling force results are presented in Appendix E.

## 2 Modeling SMA-actuated systems

Section two develops the models for the following systems:

1. An electrically-heated  $\text{Ni}_{49}\text{Ti}_{51}$  wire actuating a constant force bias spring.
2. An electrically-heated  $\text{Ni}_{49}\text{Ti}_{51}$  wire actuating a linear bias spring.
3. A bi-stable mechanism employing  $\text{Ni}_{49}\text{Ti}_{51}$  wires and permanent magnets.

The models for these systems can be applied if the actuating wire is a SMA which is not  $\text{Ni}_{49}\text{Ti}_{51}$ . The model requires additional experimental results for different SMA actuating wires. The different properties which SMAs exhibit can be seen in the experimental results of Appendix C. For example, a  $\text{Ni}_{49}\text{Ti}_{51}$  wire was able to contract 4% of its initial length; however, a  $\text{Ni}_{49}\text{Ti}_{44}\text{Hf}_7$  wire was able to contract only 1% of its initial length. These different properties are based not only on the materials used, but also on the manufacturing process. Thoma (1992) introduces results from various manufacturing processes for  $\text{Ni}_{49}\text{Ti}_{51}$  wires which are incorporated in determining the appropriate  $\text{Ni}_{49}\text{Ti}_{51}$  wire properties for the simulation models.

These systems will be simulated in the discrete time domain, using a forward difference approximation of the derivative. Equation 1 describes the forward difference equation resulting from transforming from the Laplace domain.

$$sX(s) = \frac{X(k+1) - X(k)}{kT} \quad (1)$$

$X(k)$  represents the sampled value of the state variable  $X$ . The value of  $X$  is sampled every time unit  $kT$ .  $X(k+1)$  represents the sampled value of  $X$  taken one time step  $kT$  after  $X(k)$  was sampled. Simulating the system in the discrete time domain allows the stress in the wire to be calculated for the previous sampled states of the wire. This stress is then used to assist in determining the appropriate transformation temperatures and strains in the SMA wire. Sections 2.1, 2.2 and 2.3 describe how to model the three respective systems listed at the beginning of Section 2.

2.1 Modeling an electrically-heated  $Ni_{49}Ti_{51}$  wire actuating a constant force bias spring

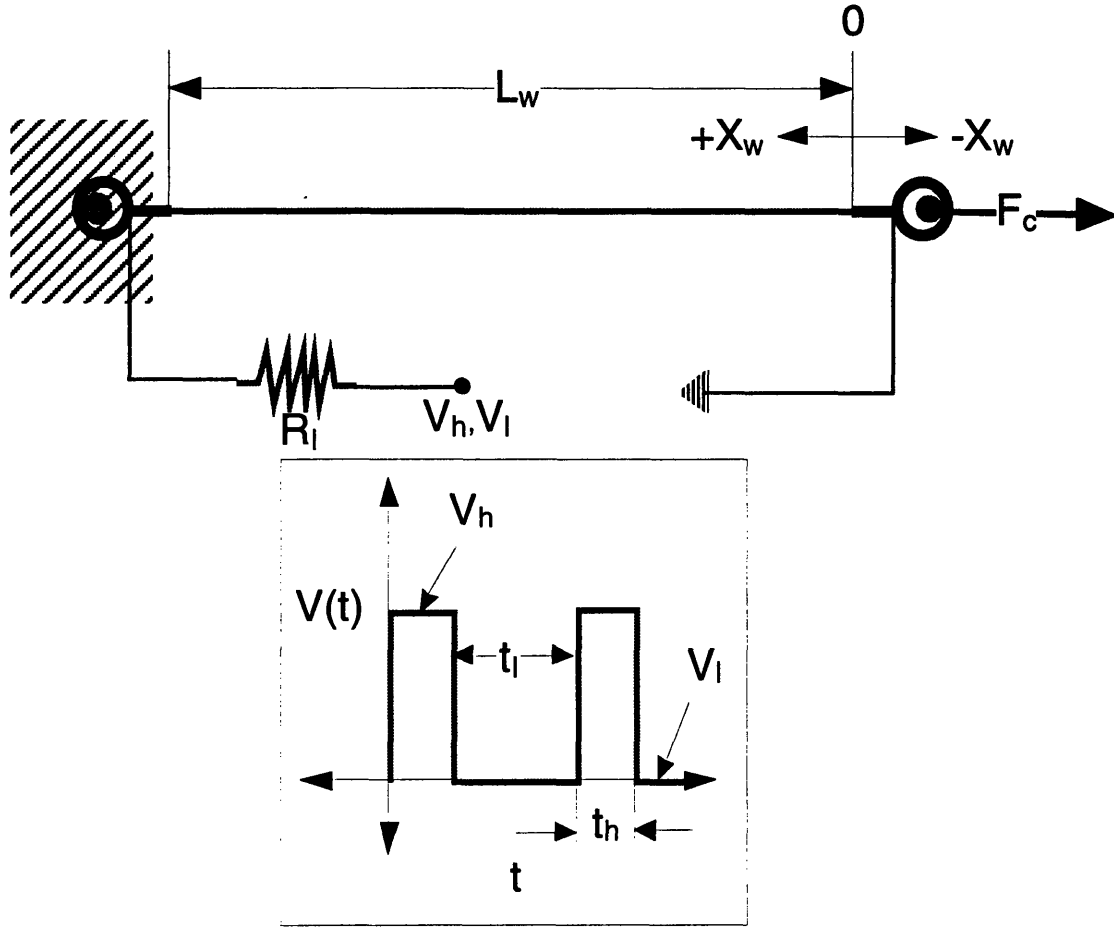


Figure 5. An electrically-heated  $Ni_{49}Ti_{51}$  wire actuating a constant force bias spring.

Figure 5 illustrates a  $Ni_{49}Ti_{51}$  wire under a constant force bias. The position of the wire ( $X_w$ ) is determined after the constant bias force ( $F_c$ ) elongates the wire. The wire is electrically heated by the square wave ( $V$ ). The voltage which heats the wire ( $V_w$ ) is determined as follows:

$$V_w = \frac{R_w}{R_w + R_l} V \quad (2)$$

$R_w$  is the resulting wire resistance and  $R_l$  is the load resistor in series with the wire and voltage source. The corresponding wire temperature ( $T_w(k)$ ) is then determined by applying the discrete form of equation B7. Next, the previous stress in the wire  $\sigma(k-1)$  is determined from the previous force in the wire  $F(k-1)$ .

$$\sigma(k-1) = \frac{F(k-1)}{A_w} \quad (3)$$

The previous stress and actuation cycle ( $N(k-1)$ ) allow the  $M_s$ ,  $M_f$ ,  $A_s$ ,  $A_f$ , unrecovered strain ( $\epsilon_U$ ) and shrink loss (SL) to be determined. These allow the resulting temperature strain ( $\epsilon_T(k)$ ) to be calculated (see Appendix B). The maximum stress and actuation cycle allow the creep ( $\epsilon_C$ ) in the wire to be calculated. The maximum stress is determined by cycling the wire on the first cycle before any creep can occur. Calculating the wire stiffness ( $K_w$ ) with equations B14 through B16 allows the resulting position of the wire ( $X_w$ ) to be determined.

$$X_w(k) = (\epsilon_T(k) - \epsilon_C(k))L_w - \frac{F_w(k-1)}{K_w} \quad (4)$$

The sign for the contracting temperature strain is positive. The sign for elongating creep is positive. The sign for a bias force which stretches out the wire is positive. The changing length of the wire is finally calculated as follows:

$$L_w(k) = L_{wi} - X_w(k) \quad (5)$$

Since the bias force is constant for this model, it is not critical to be aware of the previous force being required to calculate various properties of the wire; however, the force is not constant and the lagging estimate is necessary for the next two models.

## 2.2 Modeling an electrically-heated $Ni_{49}Ti_{51}$ wire actuating a linear bias spring

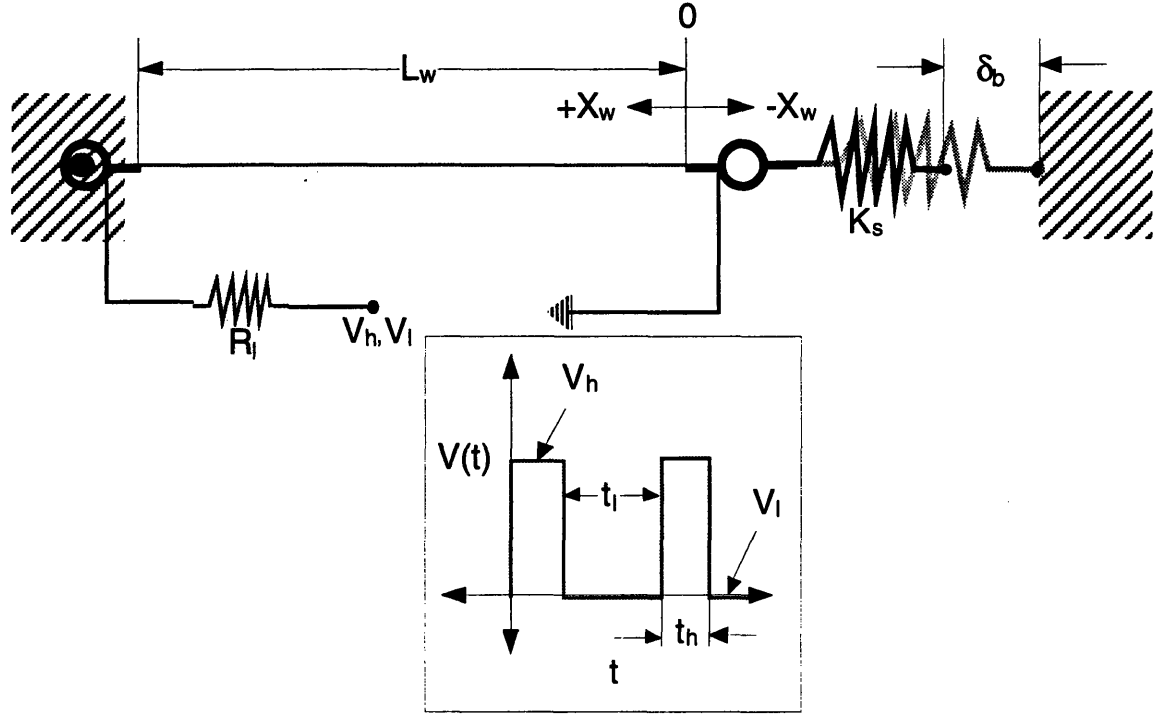


Figure 6. An electrically-heated  $Ni_{49}Ti_{51}$  wire actuating a linear bias spring.

Figure 6 shows the  $Ni_{49}Ti_{51}$  wire actuating a linear bias spring. The variable  $K_s$  represents the bias spring stiffness and  $\delta_b$  represents the net bias distance in the system. The model for the constant force biased  $Ni_{49}Ti_{51}$  wire is used for the linear spring-biased wire; however, the resulting wire position and force require different formulas. The resulting position of the wire is calculated as follows:

$$X_w(k) = \frac{1}{1 + \frac{K_s}{K_w}} \left[ \frac{-\delta_b K_s}{K_w} + (\epsilon_T(k) - \epsilon_C(k)) L_{wi} \right] \quad (6)$$

The wire position allows the corresponding force to be calculated as follows:

$$F_w(k) = K_s(X_w(k) + \delta_b) \quad (7)$$

Using equations 6 and 7 in conjunction with the analysis provided in Section 2.1 completes the model for this system.



Figure 7 illustrates the bi-stable mechanism employing  $\text{Ni}_{49}\text{Ti}_{51}$  wires and permanent magnets. The mechanism consists of two  $\text{Ni}_{49}\text{Ti}_{51}$  wires biased by two linear springs. These wires are electrically-heated in the same manner as the linear spring-biased system (a load resistor is still in series with the voltage source). When the wires are electrically heated they contract and move the low-carbon steel lever, which is biased by a permanent magnet pendulum. The magnet pendulum is mounted above the lever in such a way that the angular position of the magnet pendulum is equal to the angular position of the lever. The pendulum is also mounted so that its position is proportional to the angular position ( $\theta_L$ ) and one-quarter of the length ( $L_L$ ) of the steel lever. These assumptions allow the resulting magnetic torque ( $\tau_M$ ) to be calculated as follows:

$$\tau_M = \frac{L_L \theta_L}{4\theta_{\max}} F_M \quad (8)$$

The force of the magnet ( $F_M$ ) varies with angular position because the gap between the steel lever and the permanent magnet increases as the absolute value of the angular position approaches zero. The force will be held constant at the corresponding maximum angular position ( $\theta_{\max}$ ). Appendix D describes how to determine the resulting magnetic force for the minimum air gap and magnetic material. In order for the steel not to be saturated by a cylindrical magnet with a diameter ( $D_M$ ), the width ( $w_S$ ) and thickness ( $t_S$ ) need to have the minimal dimensions:

$$w_S = \sqrt{2}D_M \quad (9)$$

$$t_S = \frac{D_M}{4} \quad (10)$$

The magnetic and friction torques associated with the lever cause it to accelerate. The resulting lever position (independent of the bounding effects of the actuating wires) can be determined in the discrete time domain.

When the magnetic torque is positive (clockwise) the following angular position is calculated as follows:

$$\theta_L(k) = \theta_L(k-2) + 2\theta_L(k-1) - \frac{kT^2}{J}(\tau_M(k-2) - \tau_F(k-2)) \quad (11)$$

When the magnetic torque is negative (counterclockwise) the following angular position is calculated as follows:

$$\theta_L(k) = \theta_L(k-2) + 2\theta_L(k-1) - \frac{kT^2}{J}(\tau_M(k-2) - \tau_F(k-2)) \quad (12)$$

The resulting position ( $X_1$ ) in which wire 1 and the connector are pulling the pin of the lever is determined with the following equation:

$$X_1 = (L_{c1} + L_{c2} - L_p) + L_{w1} \quad (13)$$

In a similar manner the position of wire 2 and its connector ( $X_2$ ) is determined with the following equation:

$$X_2 = (L_{c1} + L_{c2} - L_p) + L_{w2} \quad (14)$$

The changing lengths of wires 1 and 2 ( $L_{w1}$  and  $L_{w2}$ ) are described by the following equation:

$$L_{w1} = L_{w1o} + \Delta X_{w1k} - \Delta X_{T1} \quad (15)$$

$$L_{w2} = L_{w2o} + \Delta X_{w2k} - \Delta X_{T2} \quad (16)$$

$L_{w1o}$  and  $L_{w2o}$  are the initial lengths of the wires.  $\Delta X_{T1}$  and  $\Delta X_{T2}$  represent the contracted change in length due to the temperature strain effect.  $\Delta X_{w1k}$  and  $\Delta X_{w2k}$  represent the change in the lengths of the two wires resulting from their changing stiffness.

The change in length due to the temperature strain effect is determined by the following equations:

$$\Delta X_{T1} = (\varepsilon_{T1} - \varepsilon_{c1})L_{w10} \quad (17)$$

$$\Delta X_{T2} = (\varepsilon_{T2} - \varepsilon_{c2})L_{w20} \quad (18)$$

The temperature strain for wires 1 and 2 ( $\varepsilon_{T1}$  and  $\varepsilon_{T2}$ ) will be determined using the previous determination of the force in the respective wires. The creep for wires 1 and 2 ( $\varepsilon_{c1}$  and  $\varepsilon_{c2}$ ) will be determined using the maximum stress in the wires and the simulation cycle. The change in the wire length due to the changing wire stiffness is determined by the following equations:

$$\Delta X_{w1k} = \frac{F_L - K_{S1}[(L_{c1} + L_{c2} + L_{c3}) + (L_{w10} + L_{S10}) - (L_p + L_{p1}) - \Delta X_{T1}]}{K_{w1} + K_{S1}} \quad (19)$$

$$\Delta X_{w2k} = \frac{F_L - K_{S2}[(L_{c1} + L_{c2} + L_{c3}) + (L_{w20} + L_{S20}) - (L_p + L_{p1}) - \Delta X_{T2}]}{K_{w2} + K_{S2}} \quad (20)$$

$F_L$  is the resulting lever force exerted on either wire 1 or 2.  $K_{S1}$  and  $K_{S2}$  are the corresponding stiffness for springs 1 and 2.  $L_{c1}$ ,  $L_{c2}$  and  $L_{c3}$  are the corresponding connector lengths indicated in Figure 7.  $L_{S10}$  and  $L_{S20}$  are the initial lengths for springs 1 and 2.  $L_p$  and  $L_{p1}$  are the respective lengths relative to the pivot pin and the anchors for the wires and springs as indicated in Figure 7.  $K_{w1}$  and  $K_{w2}$  are the changing stiffness for wires 1 and 2.  $K_{S1}$  and  $K_{S2}$  are the corresponding stiffness for springs 1 and 2. With the resulting positions of wire 1 and 2 determined, the model needs to determine if the wires are actually pulling each other. This can be determined by using the following check:

**if  $X_1 < -X_2 + D_p$  then wires are pulling each other**

**if  $X_1 \geq -X_2 + D_p$  then wires are not pulling each other**

If the wires are pulling each other, they will stretch a given amount ( $\Delta X_{s1}$  and  $\Delta X_{s2}$ ) in order to reach equilibrium.  $\Delta X_{s2}$  is determined first as follows:

$$\Delta X_{s2} = \frac{-(X_1 + X_2 - D_p)}{1 + \frac{K_{w2}R_2}{K_{w1}R_1}} \quad (21)$$

With  $\Delta X_{s2}$  calculated,  $\Delta X_{s1}$  is calculated next:

$$\Delta X_{s1} = \Delta X_{s2} \left( \frac{K_{w2}R_2}{K_{w1}R_1} \right) \quad (22)$$

$D_p$  is the diameter of the pins (on the lever) which are in contact with the actuating connectors for wires 1 and 2.  $R_1$  and  $R_2$  are the corresponding radii from the center of the two pins.

If the wires are pulling each other, then  $X_1$  and  $X_2$  need to be recalculated as follows:

$$X_1 = X_{1p} + \Delta X_{s1} \quad (23)$$

$$X_2 = X_{2p} + \Delta X_{s2} \quad (24)$$

The forces in wires 1 and 2 ( $F_{w1}$  and  $F_{w2}$ ) are then calculated as follows:

$$F_{w1} = (\Delta X_{w1k} + \Delta X_{s1})K_{w1} \quad (25)$$

$$F_{w2} = (\Delta X_{w2k} + \Delta X_{s2})K_{w2} \quad (26)$$

If the lever pin is in contact with wire 1, the corresponding lever angle is determined as follows:

$$\theta_L = \sin^{-1} \left( \frac{X_1 - \frac{D_p}{2}}{R_1} \right) \quad (27)$$

If the lever pin is in contact with wire 2, the corresponding lever angle is determined as follows:

$$\theta_L = \sin^{-1} \left( \frac{X_2 - \frac{D_p}{2}}{R_2} \right) \quad (28)$$

The lever angle is used to determine the corresponding magnetic torque ( $\tau_M$ ) and friction torque ( $\tau_F$ ), which are used to calculate the lever force ( $F_L$ ). If the lever is in contact with either wire 1 or 2, then the lever force for the wire in contact is calculated as follows:

$$F_L = \frac{|\tau_M| + |\tau_F|}{R_{1 \text{ or } 2}} \quad (29)$$

This and the previous two methods discussed will be used to create the computer simulations in Section 3.

### 3 Computer simulations of SMA-actuated systems

Computer simulations are performed on the SMA-actuated systems modeled in Section 2. Section 3.1 simulates 1 electrically-heated Flexinol 90-110 wire which actuates 4 different constant force bias springs. The wire is simulated in order to compare the theoretical temperature-position results to the experimental results discussed in Appendix C. Section 3.2 simulates a  $\text{Ni}_{49}\text{Ti}_{51}$  wire actuating a linear bias spring. The wire is given different manufacturing specifications in the simulation. The simulation illustrates and discusses the dynamic responses of the  $\text{Ni}_{49}\text{Ti}_{51}$  wire. Section 3.3 simulates a working bi-stable mechanism employing  $\text{Ni}_{49}\text{Ti}_{51}$  wires and a permanent magnet pendulum.

#### 3.1 *Simulation of an electrically-heated $\text{Ni}_{49}\text{Ti}_{51}$ wire actuating a constant force bias spring*

This computer simulation is used to compare the simulated temperature-contraction curves, to the experimental curves discussed in Appendix C. The following parameters for the wire were used in the simulation:

1. Wire type: Flexinol 90-110 wire
  - 425°C heat treatment for 1 hour
  - pre-cycled 200 times under a 207 MPa stress
  - temperature strain at  $A_s$  is 0.005
  - temperature strain at  $A_f$  is 0.040
  - temperature strain at  $M_f$  is 0.005
  - temperature strain is zero at  $T_0$  which is 25°C
  
2. Wire dimensions:
  - $L_w$  is 61.59 cm
  - $D_w$  is 75.0 microns

### 3. Wire stress:

- 4.3 MPa (2 grams or 0.0196 Newtons)
- 47.3 MPa (22 grams or 0.2158 Newtons)
- 86.0 MPa (40 grams or 0.3924 Newtons)
- 150.4 MPa (70 grams or 0.6867 Newtons)

Figures 8 through 11 compare the simulated wire temperature-position curve to the experimental curve.

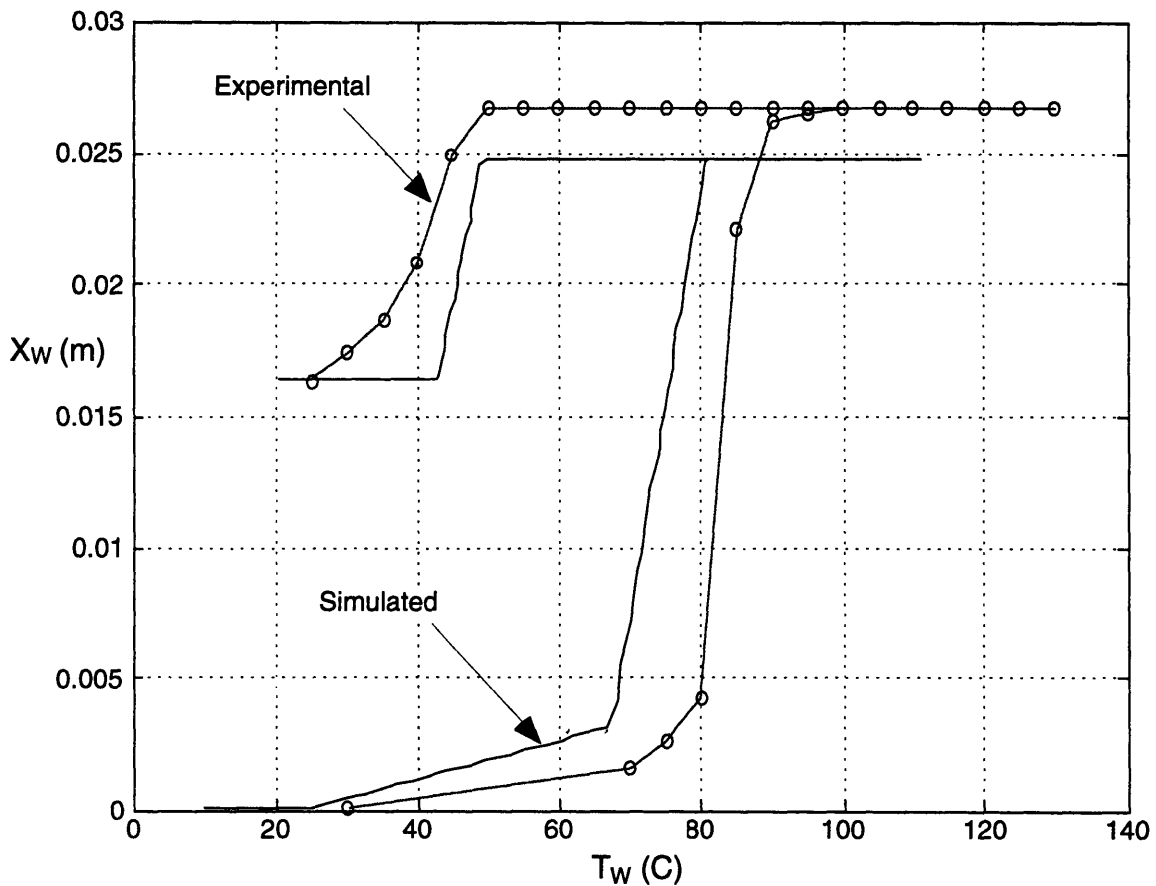


Figure 8. Simulated and experimental temperature-position curves for a 4.3 MPa biased Flexinol 90-110 wire.

Figure 8 indicates that the simulated As temperature is lower than the experimental. It also indicates that the temperature strain may be more than .04 since the experimental wire contracted more than the simulated wire. The unrecovered strain is correct; however, the

lagging recovery could be modeled more accurately to match the actual curve. Despite these differences, as the stress increases in the wires, the simulated and experimental curves tend to match each other more closely.

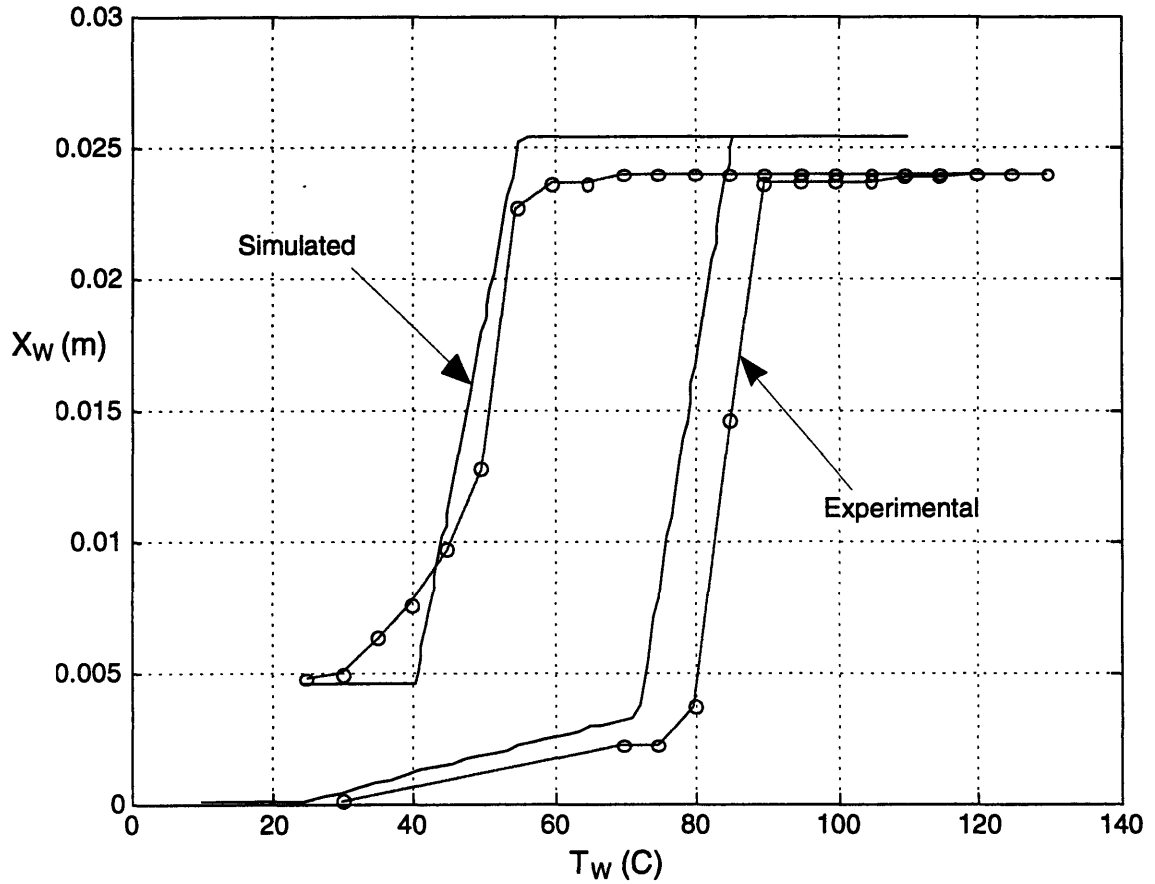


Figure 9. Simulated and experimental temperature-position curves for a 47.3 MPa biased Flexinol 90-110 wire.

Figure 9 indicates that the  $A_s$  temperature is still underestimated. It also indicates that unlike in Figure 8, the strain at  $A_f$  is overestimated. The simulated  $M_s$  temperature approximately matches the experimental. The unrecovered strain is also correct; however, the lagging recovery could still be modeled. Figures 10 and 11 indicate that the simulated wire results continue to match approximately to the experimental results.

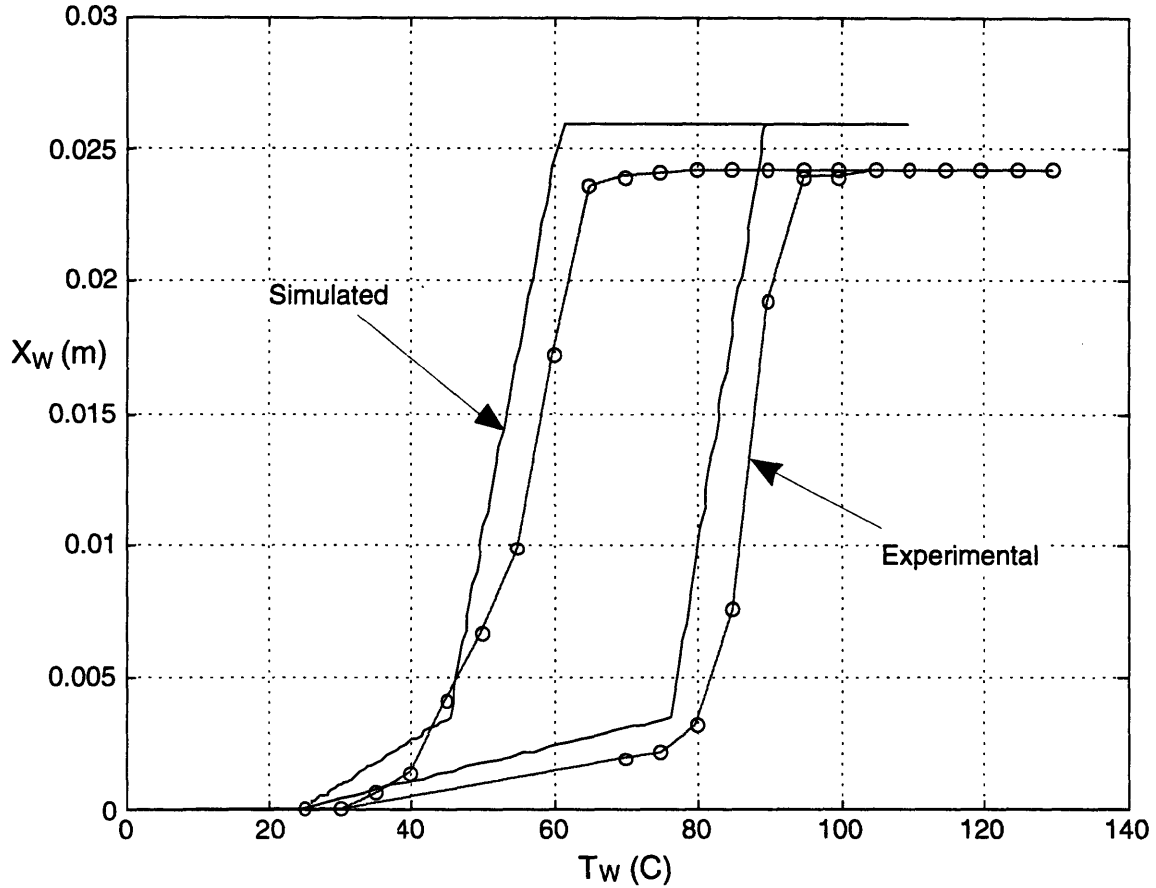


Figure 10. Simulated and experimental temperature-position curves for a 86.0 MPa biased Flexinol 90-110 wire.

Figure 10 indicates that the strain at Af is overestimated. The As temperature is still underestimated. The simulated curve correctly determines that the unrecovered strain should be zero. This simulated curve indicates that the lagging recovery is incorporated in the wire simulation. Figure 11 compares the final temperature-position curves for a 150.4 MPa biased Flexinol 90-110 wire.

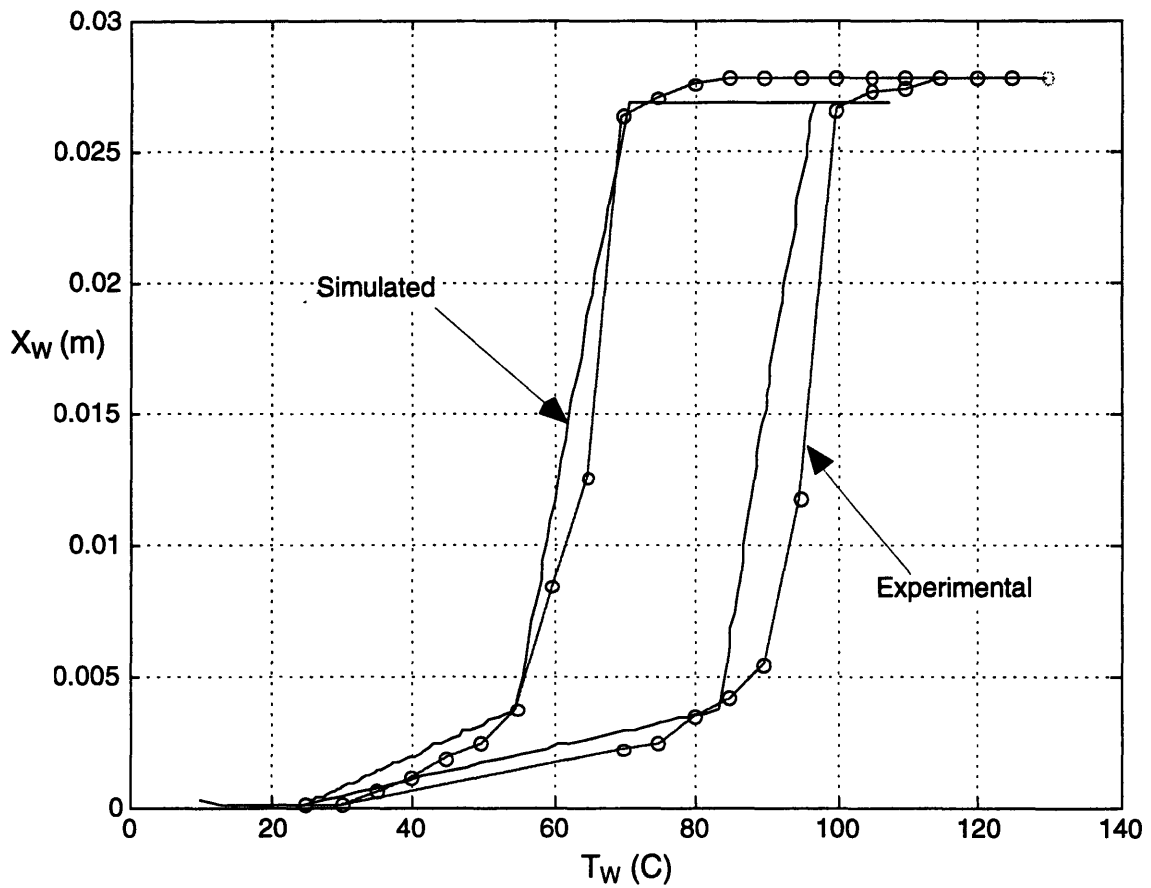


Figure 11. Simulated and experimental temperature-position curves for a 150.4 MPa biased Flexinol 90-110 wire.

Figure 11 indicates that the simulated temperature-position curve closely matches the experimental curve. Figures 8 through 11 indicate that the simulation model provides an adequate means for predicting performance. Section 3.2 simulates an electrically-heated  $\text{Ni}_{49}\text{Ti}_{51}$  wire actuating a linear bias spring, and discusses the dynamic results.

### ***3.2 Simulation of an electrically-heated Ni<sub>49</sub>Ti<sub>51</sub> wire actuating a linear bias spring***

This computer simulation is used to illustrate the dynamic results of a linear spring-biased wire. A wire is manufactured in the “Create Your Own Wires” menu and is given the following parameters for the simulation:

1. Wire type: Ni<sub>49</sub>Ti<sub>51</sub>
  - 400°C heat treatment for 1 hour
  - Is not pre-cycled 200 times under a 207 MPa stress
  - temperature strain at A<sub>s</sub> is .0025
  - temperature strain at A<sub>f</sub> is .05
  - temperature strain at M<sub>f</sub> is .005
  - temperature strain is zero at T<sub>0</sub> which is 25°C
  
2. Wire dimensions:
  - L<sub>w</sub> is 10.0 cm
  - D<sub>w</sub> is 75.0 microns
  
3. Wire bias spring:
  - K<sub>s</sub> is 30.0 N/m
  - δ<sub>b</sub> is .008 m
  
4. Heating parameters:
  - T<sub>env</sub> is 10°C
  - V<sub>h</sub> is 3.25 Volts
  - V<sub>l</sub> is 0.0 Volts
  - t<sub>h</sub> is 1.5 seconds
  - t<sub>l</sub> is 1.5 seconds
  - R<sub>j</sub> is 1.89 Ω

- $R_w$  is  $18.11 \Omega$

5. Simulation starts on cycle 10,000

The simulation results are plotted in Figures 12-15:

Figure 12: Simulated temperature-time curve for  $\text{Ni}_{49}\text{Ti}_{51}$  wire

Figure 13: Simulated length-time curve for  $\text{Ni}_{49}\text{Ti}_{51}$  wire

Figure 14: Simulated stress-time curve for  $\text{Ni}_{49}\text{Ti}_{51}$  wire

Figure 15: Simulated temperature-strain curve for  $\text{Ni}_{49}\text{Ti}_{51}$  wire

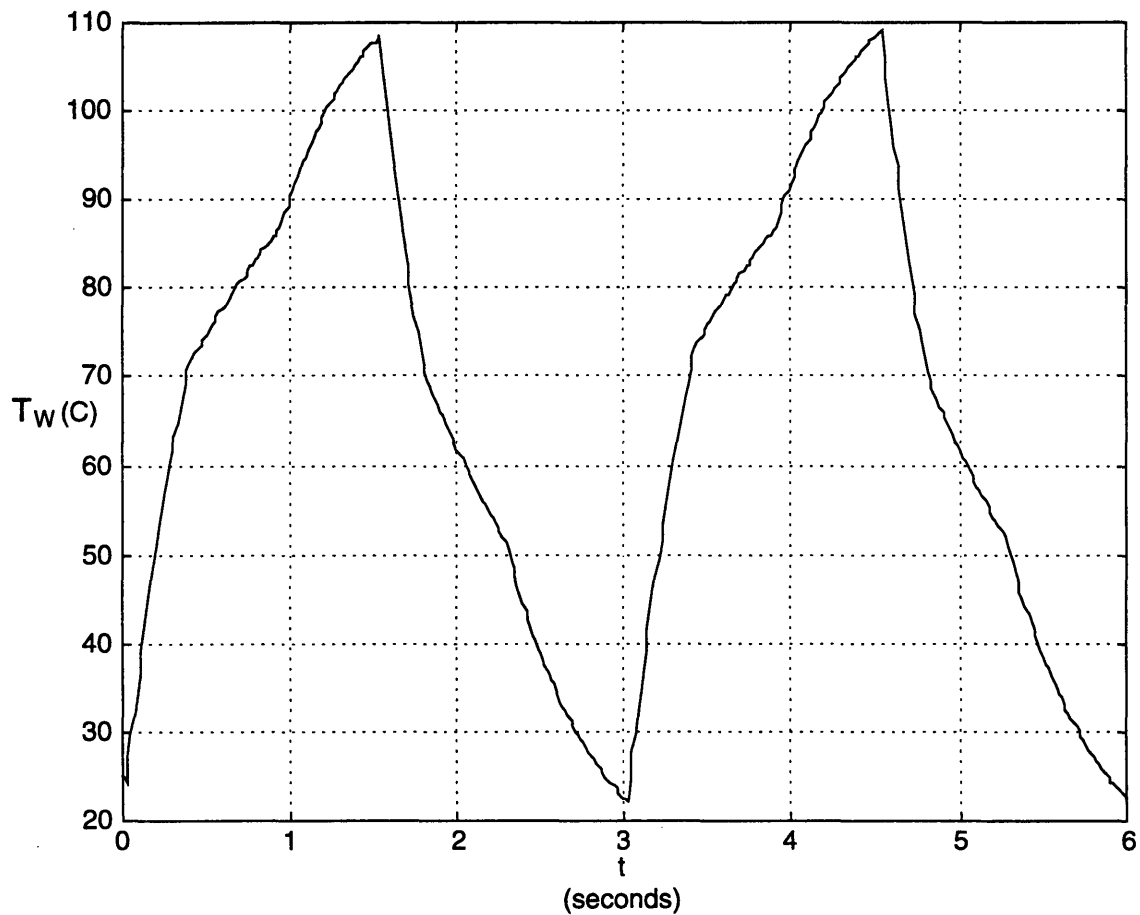


Figure 12. Simulated temperature-time curve for  $\text{Ni}_{49}\text{Ti}_{51}$  wire.

Figure 12 shows the changing wire temperature as a function of time. The changing temperature corresponds to the heating square wave. The wire temperature repeatedly increases for 1.5 seconds and then decreases for 1.5 seconds. The phase-change effects on

the specific heat are clearly illustrated when the temperature takes .5 seconds to rise from 70°C to 90°C (the  $A_s$  and  $A_f$  temperatures). In a similar manner, the temperature takes .4 seconds to drop from 70°C to 50°C (the  $M_s$  and  $M_f$  temperatures). Figure 13 illustrates the changing wire length with respect to time.

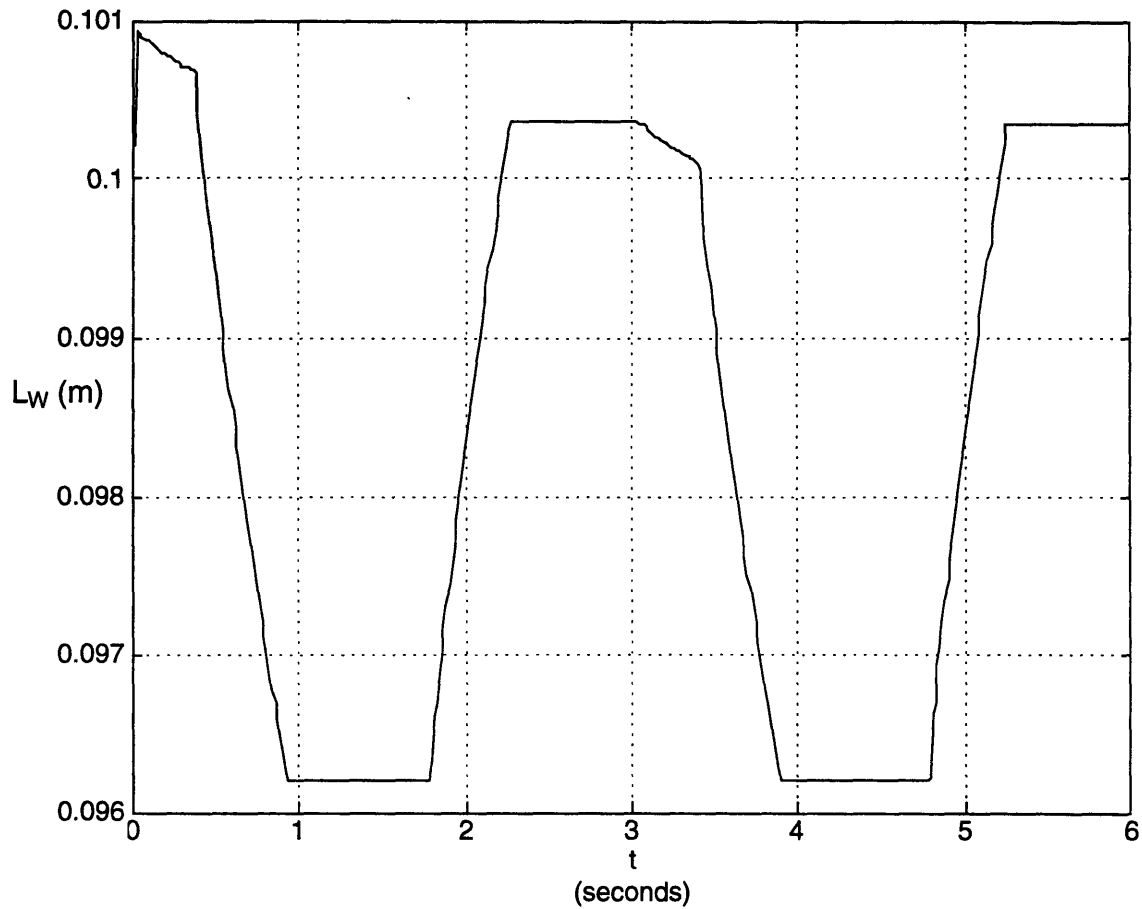


Figure 13. Simulated length-time curve for  $Ni_{49}Ti_{51}$  wire.

Figure 13 indicates that the wire elongated approximately 1.0 mm (the initial increase in length from .1 to .101 meters) due to creep. As a result, the bias stress in the wire is reduced and the wire is unable to elongate to its initial stretched-out length of .101 meters. Figure 14 displays the corresponding wire stress with respect to time.

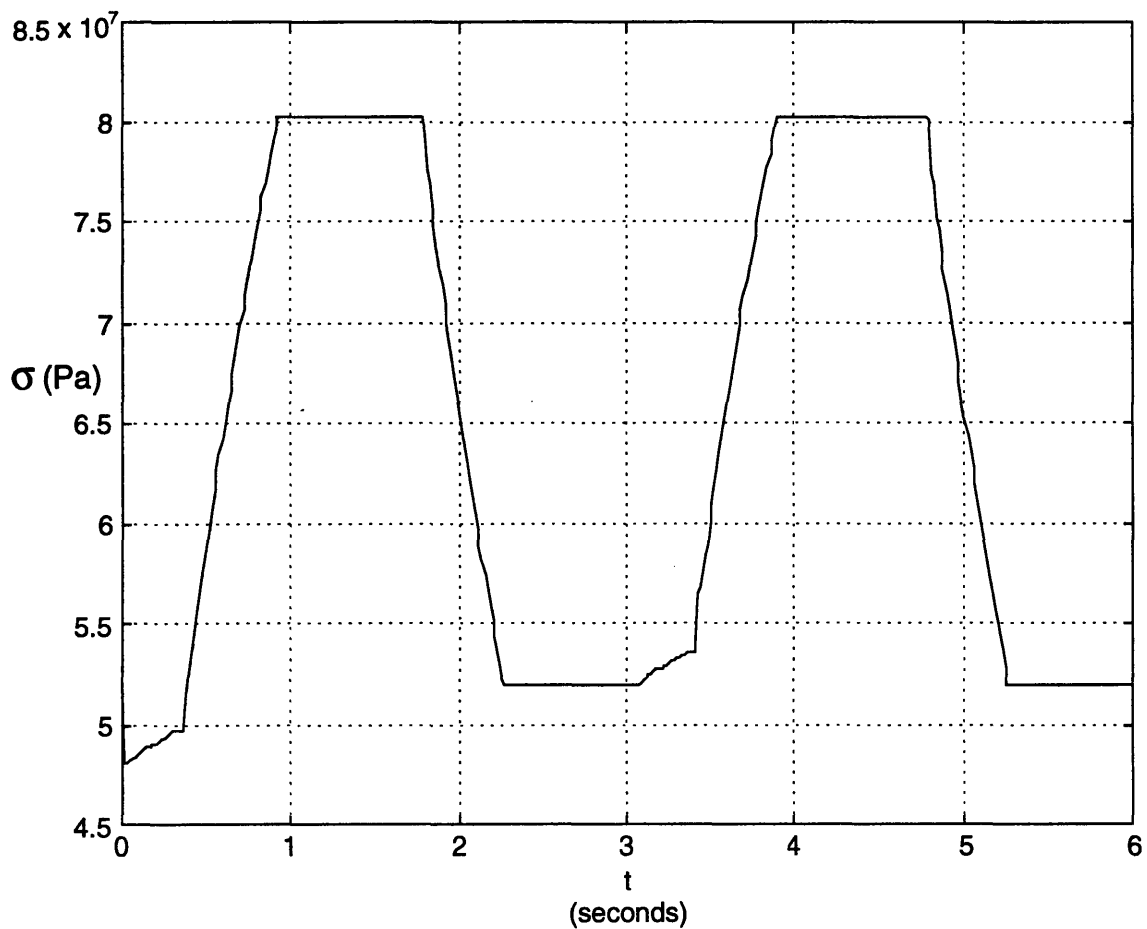


Figure 14. Simulated stress-time curve for  $\text{Ni}_{49}\text{Ti}_{51}$  wire.

Figure 14 illustrates that as the wire elongates, the stress decreases to a point beyond which it can not elongate any further. Due to the amount of creep and type of spring used, the wire was unable to continue elongating once the stress reached 52 MPa. Figure 15 illustrates the resulting temperature-strain curve.

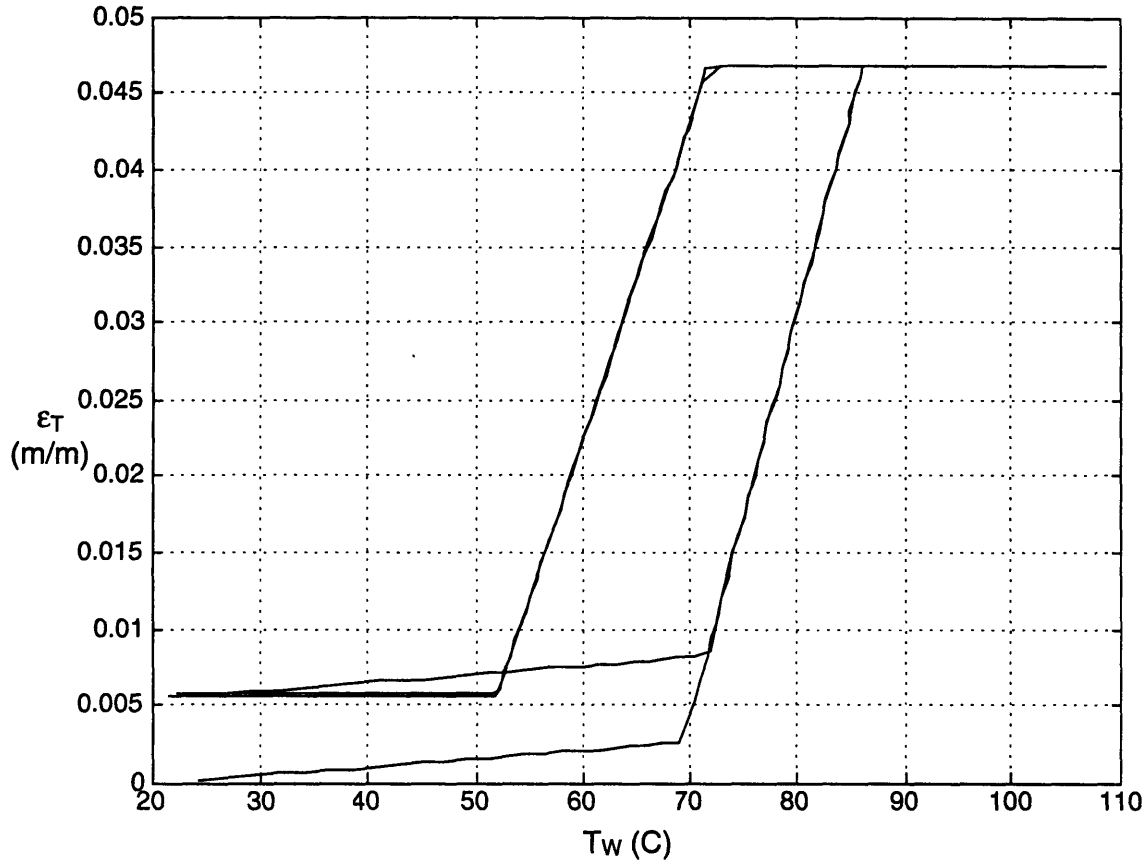


Figure 15. Simulated temperature-strain curve for  $\text{Ni}_{49}\text{Ti}_{51}$  wire.

The temperature-strain curve illustrates that the maximum strain has reduced from .05 to .047 after 10,000 cycles. The spring was unable to provide enough bias stress to insure complete elongation of the wire. The strain at As is now .0025. Finally, when the unrecovered wire's temperature increases, the strain increases in the same manner as if the wire were fully recovered. This final property of the hysteresis loop is unproven; however, this property is one possible explanation for the inner hysteresis loop. Another explanation could be that the wire does not contract at all until the temperature corresponds to the primary temperature-strain curve. Section 3.3 simulates a working bi-stable mechanism employing  $\text{Ni}_{49}\text{Ti}_{51}$  wires and a permanent magnet pendulum.

### 3.3 Simulation of a bi-stable mechanism employing $Ni_{49}Ti_{51}$ wires and permanent magnets

The bi-stable mechanism simulated in this Section is designed to move the magnet pendulum back and forth 1,000,000 times. The permanent magnet is Samarium Cobalt and has the following dimensions:

- $D_M$  is 5.08 millimeters
- $L_M$  is 5.08 millimeters

The resulting magnet force ( $F_M$ ) - gap ( $X_g$ ) curve is determined using the formulas and correction factors presented in Appendix D.

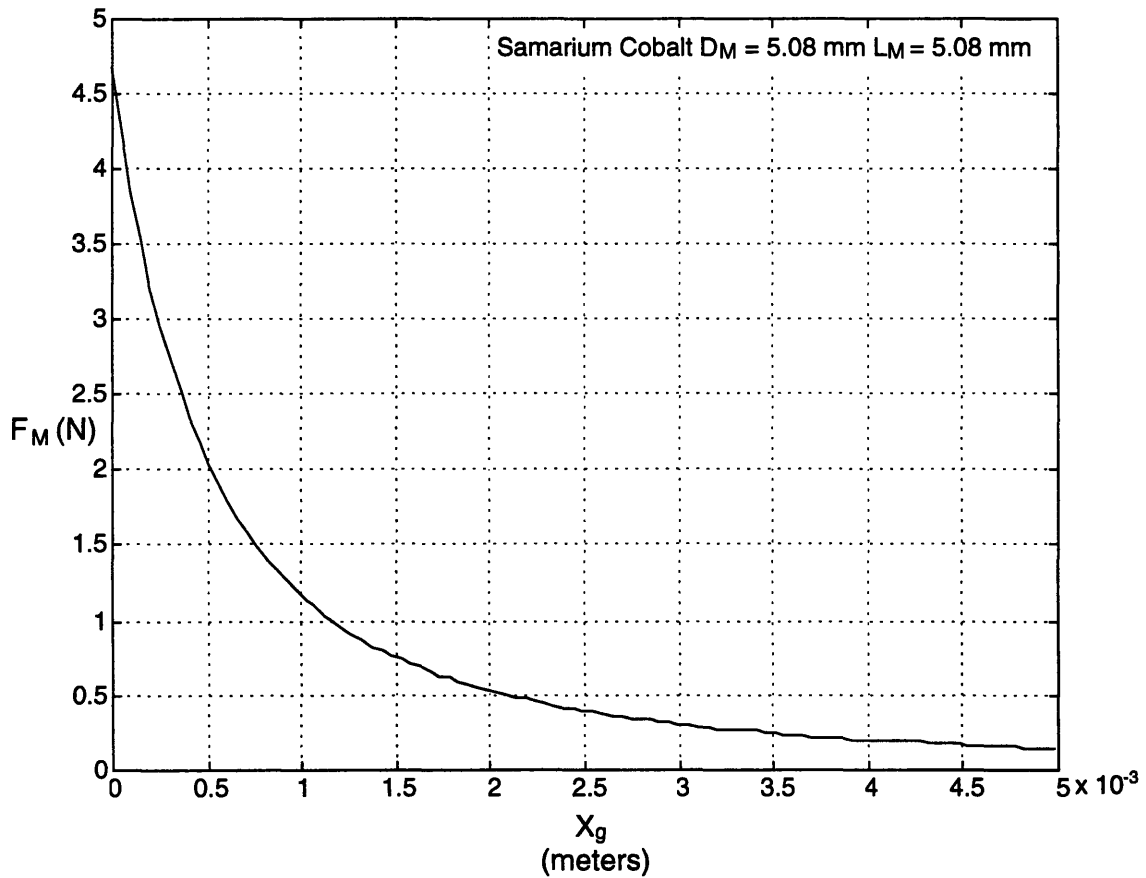


Figure 16. Simulated magnetic force-gap curve for Samarium Cobalt.

The minimum gap between the magnet and steel lever is 2.0 mm and the corresponding force is .5 Newtons. The lever length is defined in order to create the magnetic torque ( $\tau_M$ ) dependence on the lever's angular position ( $\theta_L$ ) (see equation 8).

- $L_L$  is 5.08 centimeters
- $w_s$  is .80 centimeters (see equation 9)
- $t_s$  is .20 centimeters (see equation 10)
- $\rho_s$  is 6,450 kg/m<sup>3</sup>

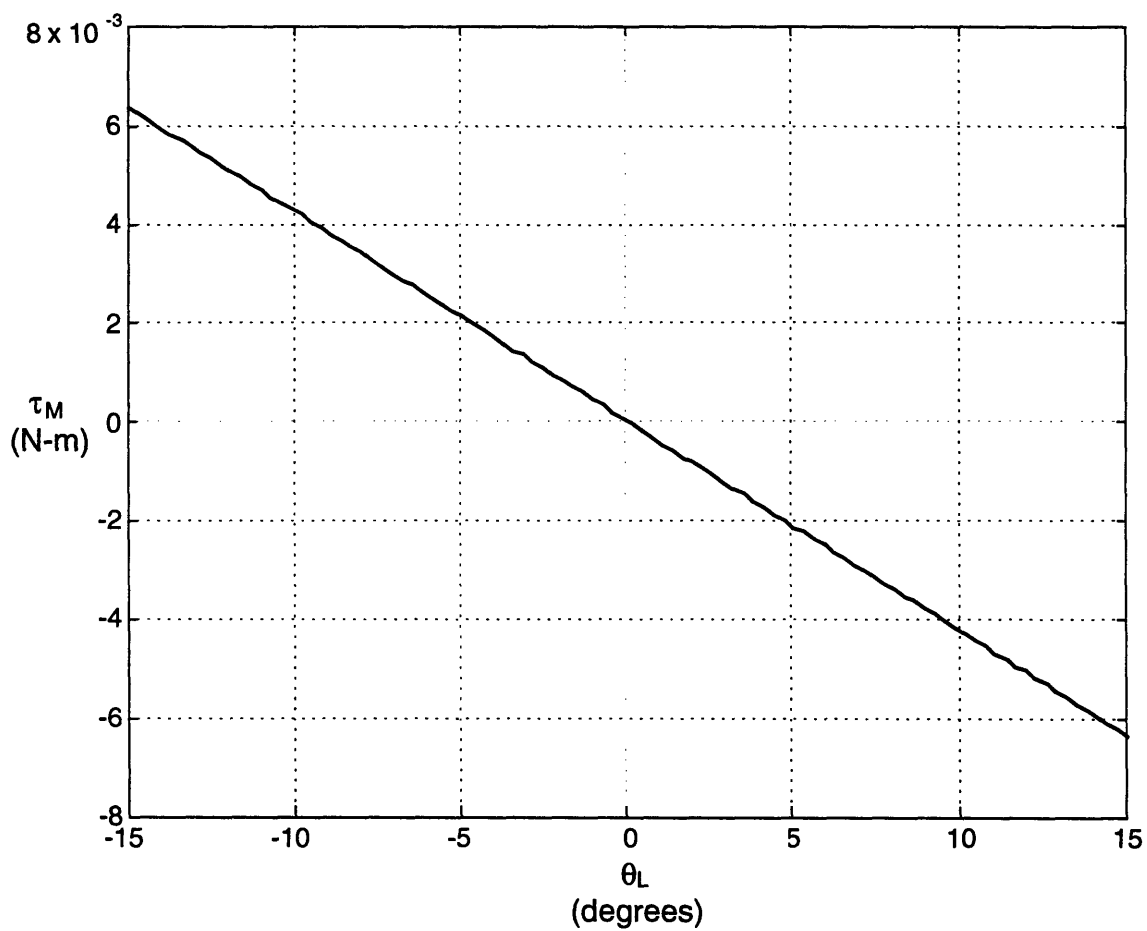


Figure 17. Resulting magnetic torque-angular position curve from Samarium Cobalt pendulum.

Friction losses at the rotating pin are neglected; however, the normal friction force ( $F_f$ ) of the steel lever will be incorporated in simulating any friction losses. The normal friction force is constant at all corresponding lever angles. The friction force, friction radius ( $R_f$ ), coefficient of static friction ( $\mu_s$ ) and coefficient of kinetic friction ( $\mu_k$ ) are chosen as follows:

- $F_f$  is .005 Newtons
- $R_f$  is 1.25 centimeters
- $\mu_s$  is .30
- $\mu_k$  is .10

Two Flexinol 90-110 wires were used with the following dimensions:

- $L_{w1}$  is equal to  $L_{w2}$  which is 18.0 centimeters
- $D_{w1}$  is equal to  $D_{w2}$  which is 100 micrometers

The springs which biased the wires have the following stiffness and lengths:

- $K_{s1}$  is equal to  $K_{s2}$  which is 25 N/m
- $L_{s1}$  is equal to  $L_{s2}$  which is 5.0 centimeters

The following assembly dimensions are used:

- $L_{c1}$  is 0.5 centimeters
- $L_{c2}$  is 2.0 centimeters
- $L_{c3}$  is 0.5 centimeters
- $D_p$  is .10 centimeters
- $R_1$  is 2.0 centimeters
- $R_2$  is 2.0 centimeters
- $L_p$  is 19.9 centimeters
- $L_{p1}$  is 8.1 centimeters

The following heating parameters are used for the wires:

- $T_{env}$  is  $25^{\circ}\text{C}$
- $V_{h1}$  is equal to  $V_{h2}$  which is 12.0 Volts
- $V_{l1}$  is equal to  $V_{l2}$  which is 0.0 Volts
- $t_{h1}$  is equal to  $t_{h2}$  which is 3.0 seconds
- $R_{l1}$  is equal to  $R_{l2}$  which is  $40.0\ \Omega$
- $t_c$  is 4.0 seconds

The following parameters are used to simulate the working system. Figure 18 illustrates the changing angular position of the lever with respect to time.

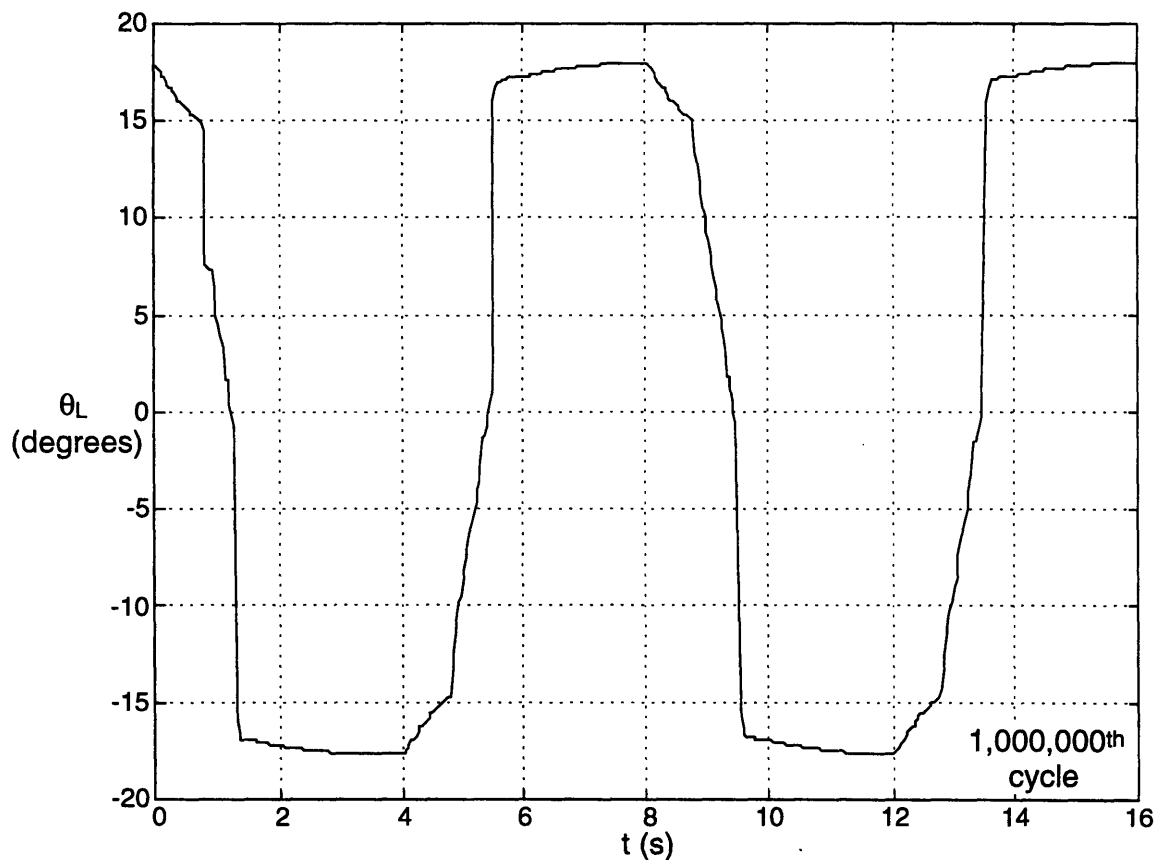


Figure 18. Simulated angular position-time curve for steel lever.

The resulting angular position is plotted with respect to time. Note that every 4 seconds ( $t_c$ ) one of the wires is being heated. The heated wire is contracting and pulling the lever past 0 degrees in order to allow the magnetic torque to accelerate the lever to the other side. At 0 seconds, wire 1 contracts and pulls the lever past 0 degrees. The lever then accelerates into wire two. At 4 seconds, wire 2 contracts and pulls the lever past 0 degrees, etc. Figure 19 illustrates the corresponding changing stress of wire 2 to the lever position.

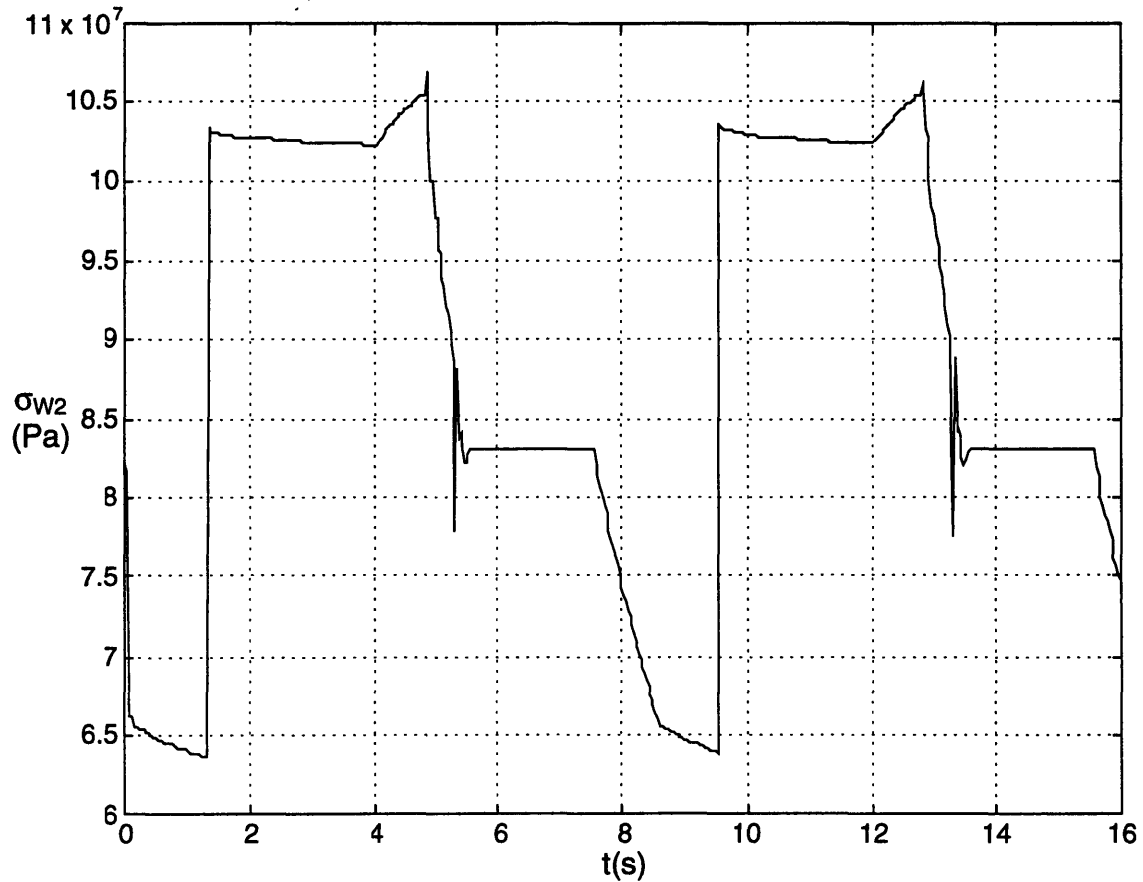


Figure 19. Simulated stress-time curve for  $\text{Ni}_{49}\text{Ti}_{51}$  wire (wire 2).

As the lever makes contact with wire 2 at 1.5 seconds, the stress increases approximately 40.0 MPa. As the wire begins to contract at 4 seconds, the stress begins to increase. This occurs because the magnetic torque is constant and does not begin to decrease until the absolute value of the angular position is less than 15 degrees. At 4.7 seconds the stress in the wire decreases because the wire force caused by the magnetic torque is decreasing at a faster rate than the spring force is increasing. At approximately 5.5 seconds the lever is no

longer in contact with wire 2 and the stress in the wire is dependent on the bias spring. In Figure 20 the temperature-strain curve for wire 1 is presented.

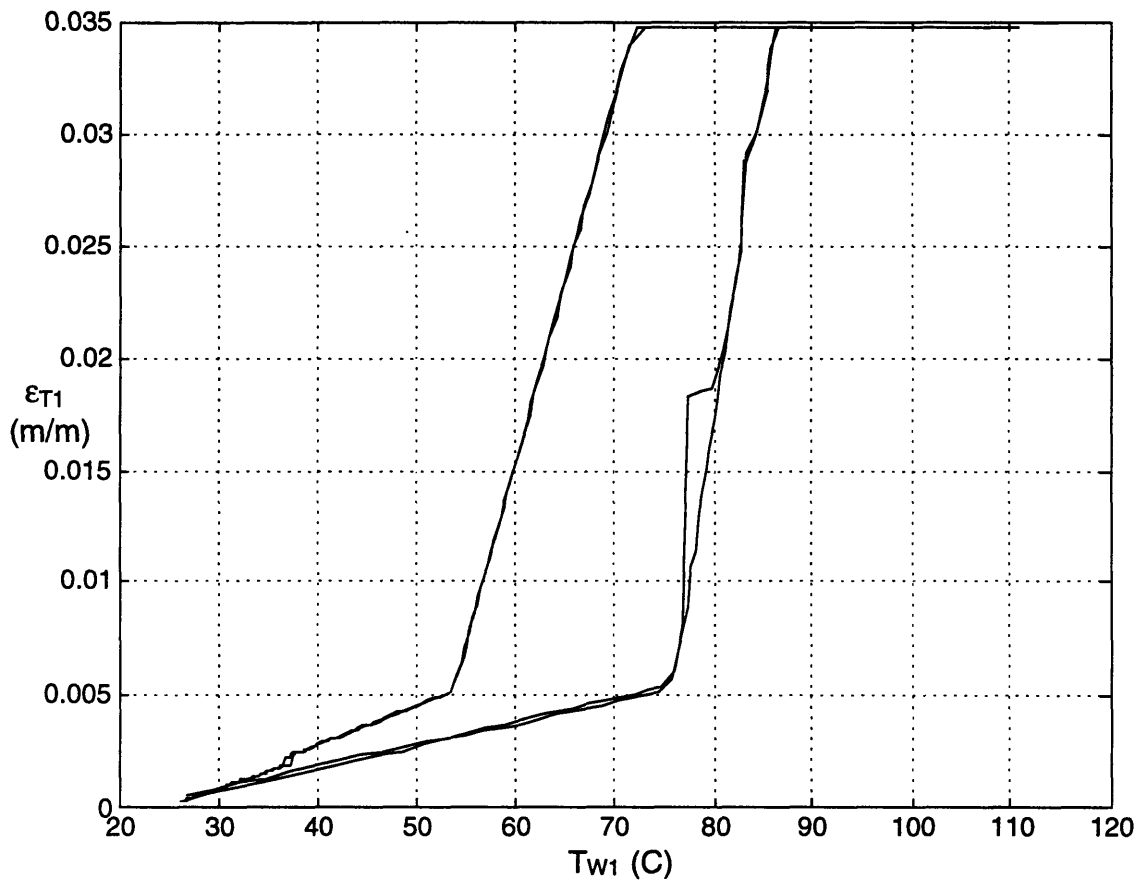


Figure 20. Simulated temperature-strain curve for Ni<sub>49</sub>Ti<sub>51</sub> wire (wire 1).

The temperature-strain curve shows how the strain path from As to Af tends towards the As temperature. This occurs because the stress in the wire decreases for the majority of that transition from As to Af. The As and Af temperatures decrease as the stress decreases; hence, the slope of the right curve increases as the strain and temperature increase. On the left side of the temperature-strain curve, the slope is constant until the elongating strain is about .0025. At that point the slope becomes less steep because the corresponding Mf temperature has increased. Note that the maximum temperature strain is slightly less than .035. This correctly indicates that after 1,000,000 cycles the wire has lost 12.5% of its net ability to contract.

The magnetic force was doubled (increasing the maximum wire stress to 150 MPa). The system was still able to actuate after 1,000,000 cycles. When the magnetic force was tripled (increasing the maximum wire stress to 180 MPa), however, the system could not actuate for 1,000,000 cycles. These simulation results lead to the following general design rules:

1. Design for 3.0% shrink (  $2.0\sin(15^\circ)/18.0 = .0317$  )
2. Note that the remaining 0.5 % shrink will recover from  $M_f$  (45°C) to  $T_o$  (25°C)
3. Bias the wire with 70 MPa stress
4. Maximum actuation stress of 150 MPa

## 4 Conclusions and Recommendations

A model for Shape Memory Alloys has been presented which addresses the actuating dynamics and the changing properties due to cycling, stress and manufacturing. Thoma's work with the manufacturing and cycling effects on  $\text{Ni}_{49}\text{Ti}_{51}$  wires enabled a computer simulation model for these wires to be developed. This computer simulation program approximately matched the experimental temperature-strain curves of Flexinol 90-110 wires. These results imply that the wires were manufactured in the following manner:

1. The  $\text{Ni}_{49}\text{Ti}_{51}$  wire was first annealed and then cold-worked to reduce the cross-sectional surface area by 40%.
2. The  $\text{Ni}_{49}\text{Ti}_{51}$  wire was then heat-treated for 1 hour at 425°C.
3. Next, the  $\text{Ni}_{49}\text{Ti}_{51}$  wire was constrained with a 4% strain while being cycled 5 times between the  $M_f$  and  $A_f$  temperatures. This allows the wire to contract and elongate with just a 65 MPa bias stress.
4. Finally, the  $\text{Ni}_{49}\text{Ti}_{51}$  wire was pre-creeped by cycling the wire approximately 200 times under a 207 MPa stress.

This working model for  $\text{Ni}_{49}\text{Ti}_{51}$  wires allowed a bi-stable mechanism employing  $\text{Ni}_{49}\text{Ti}_{51}$  wires and permanent magnets to be simulated. The goal was to make the mechanism cycle 1,000,000 times with pre-creeped  $\text{Ni}_{49}\text{Ti}_{51}$  wires. The simulation and experimental results led to the following design rules for these wires:

1. Design for 3.0% shrink
2. Note that the remaining 0.5% shrink will recover from  $M_f$  (45°C) to  $T_o$  (25°C)
3. Bias the wire with 70 MPa stress
4. Maximum actuation stress of 150 MPa

It is then essential to design the SMA actuating device in such a way so that the maximum strain of the SMA member under stress does not exceed 3% when it transforms to Martensite.

- Zhang, Zee and Thoma (1996)

An experimental attempt was made to cycle a Ni<sub>49</sub>Ti<sub>51</sub> wire 1,000,000 times under a 160 MPa stress. Two of the wires cycled approximately 1,000,000 times and two other wires cycled approximately 10,000 times. The cause of wire failure was located at the wire crimp termination. These wire failures imply that any type of constrained bending at the wire's ends will lead to premature failure.

It is essential to prevent localized preferential straining of the actuating member during its transformation from Austenite to Martensite.

- Zhang, Zee and Thoma (1996)

A theoretical model was developed to determine the relationship between the resulting permanent magnet pulling force at a given air gap. The model was based on the work done by Fitzgerald (1990), in which a fictitious coil winding is used to drive the flux density of the system to zero in order to determine the coenergy of the magnetic field. Two correction factors were introduced in order to match the theory to the experimental results. The correction factors enable the force-gap curves to be determined for Samarium Cobalt, Neodymium Iron Boron, Bonded Neodymium Iron Boron, Ceramic 5 and Ceramic 8 magnets.

## Appendix A: Users Manual for Design Program

This users manual is written to show how a designer can create the following three simulations:

1. An electrically-heated  $\text{Ni}_{49}\text{Ti}_{51}$  wire actuating a constant force bias spring.
2. An electrically-heated  $\text{Ni}_{49}\text{Ti}_{51}$  wire actuating a linear bias spring.
3. A bi-stable mechanism employing  $\text{Ni}_{49}\text{Ti}_{51}$  wires and permanent magnets.

The design program is written in a higher-level code and requires the software package MATLAB® to operate. The interface occurs in windows with interactive Handle

Graphics™ objects. The objects which will be used are push buttons, pop-up buttons, and editable-text buttons.

1. Push buttons are used to implement the command displayed on the button. Push buttons can be implemented by moving the mouse pointer over the button and pressing on the mouse button.
2. Pop-up buttons are used to list numerous options to be selected. Pop-up buttons can be implemented by moving the mouse pointer over the button and holding down the mouse button to scroll to a desired selection.
3. Editable-text buttons are used to allow the user to input the desired value for a given variable. Editable-text buttons can be implemented by moving the mouse pointer over the button, depressing the mouse button, and typing the desired text.

**A.1 *Simulating an electrically-heated  $Ni_{49}Ti_{51}$  wire actuating a constant force bias spring.***

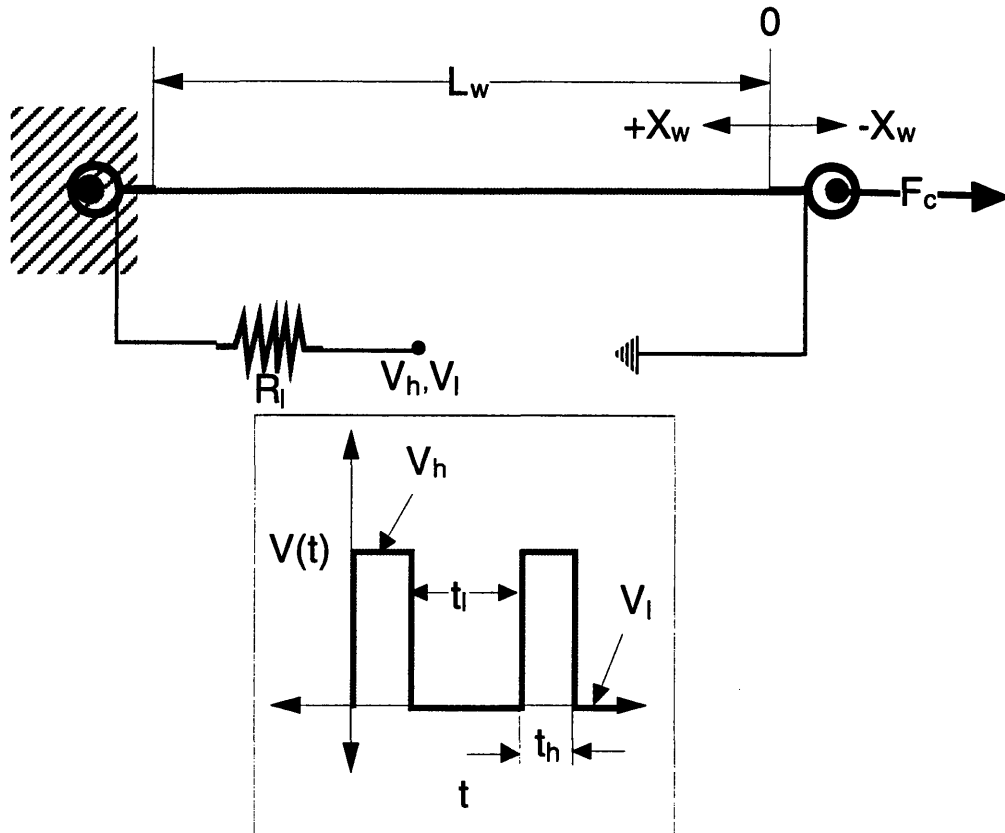


Figure A1. An electrically-heated  $Ni_{49}Ti_{51}$  wire actuating a constant force bias spring.

Figure A1 shows the simulation setup and parameters to be defined by the designer. The designer wants to make a  $Ni_{49}Ti_{51}$  wire, with a given wire length ( $L_w$ ), actuate a constant force ( $F_c$ ) bias spring. The designer needs to create an electrical square wave to heat the wire. The square wave will require high voltage ( $V_h$ ), high time ( $t_h$ ), low voltage ( $V_l$ ) and low time ( $t_l$ ). The designer can also add a load resistor ( $R_l$ ) in series with the  $Ni_{49}Ti_{51}$  wire. The position of the wire ( $X_w$ ) is set at zero before the constant force bias spring is applied.

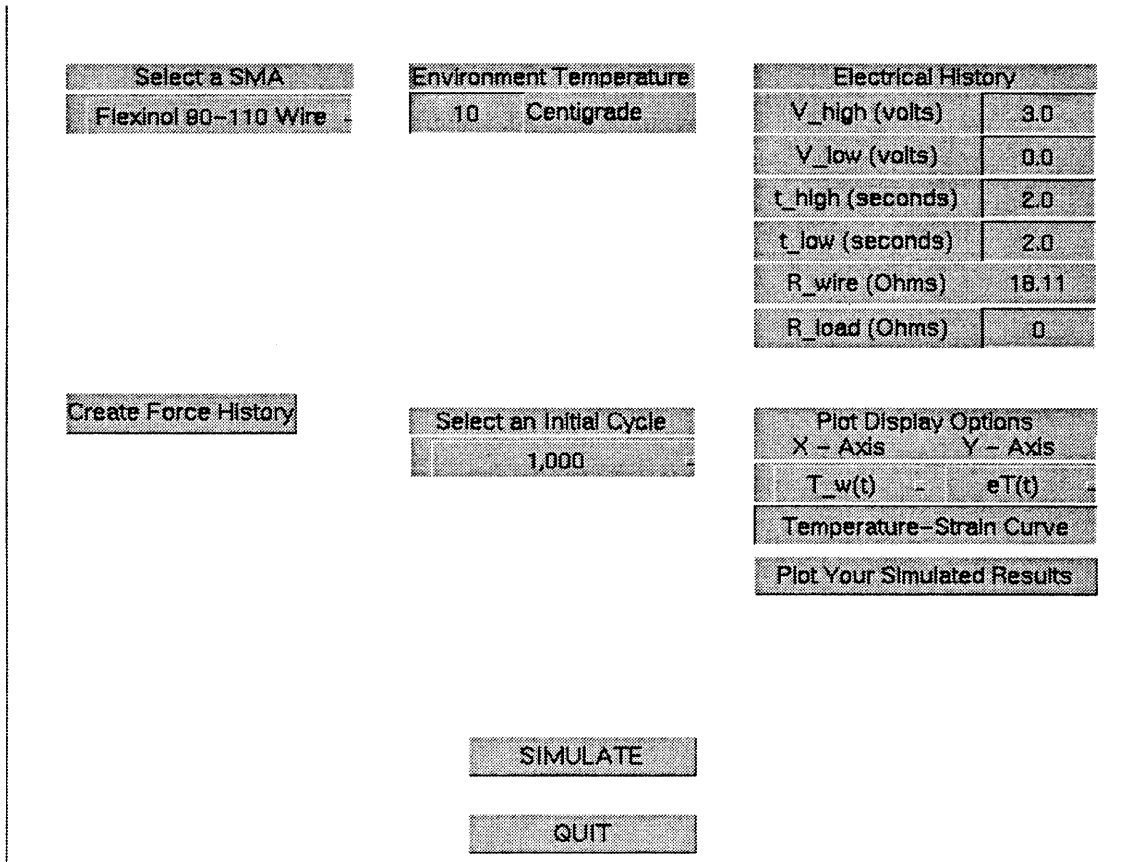


Figure A2. Design menu used to simulate an electrically-heated Ni<sub>49</sub>Ti<sub>51</sub> wire.

Figure A2 illustrates the initial design menu to perform the simulation. This menu consists of six parts:

1. The “Select a SMA” section allows the user to describe the type of Ni<sub>49</sub>Ti<sub>51</sub> wire to be used. There are three choices:
  - The “Flexinol 90-110 Wire” choice is for Ni<sub>49</sub>Ti<sub>51</sub> wires manufactured by Dynalloy. The wires have a circular cross-section.
  - The “Mondo-tronics Ribbon” choice is for Ni<sub>49</sub>Ti<sub>51</sub> wires manufactured by Mondo-tronics. The wires have a rectangular cross-section.
  - The “Create Your Own” choice allows the user to manufacture the Ni<sub>49</sub>Ti<sub>51</sub> wire by choosing options such as the wire’s heat treatment temperature, and whether to pre-cycle the wire.
2. The “Environment Temperature” section allows the user to define the environmental temperature.

3. The “Electrical History” section allows the user to define the electrical square wave and load resistance to heat the wire.
4. The “Create Force History” section allows the user to define the constant force bias spring or a linear force bias spring.
5. The “Select an Initial Cycle” section allows the user to define which transformation cycle to simulate. The user can select cycle 1, 10, 100, 1,000, 10,000, 100,000, 1,000,000 or 10,000,000.
6. The “Plot Display Options” section allows the user to plot the simulation results:
  - time for the simulation (seconds)
  - $V(t)$ , which is the square wave (Volts) corresponding to time
  - $T_w(t)$ , which is the wire temperature (Centigrade) corresponding to time
  - $\epsilon T(t)$ , which is the temperature strain (m/m) corresponding to time
  - $X(t)$ , which is the actual position (meters) corresponding to time
  - $\text{Stress}(t)$ , which is the wire stress (Pa) corresponding to time
  - $L_w(t)$ , which is the wire length (meters) corresponding to time

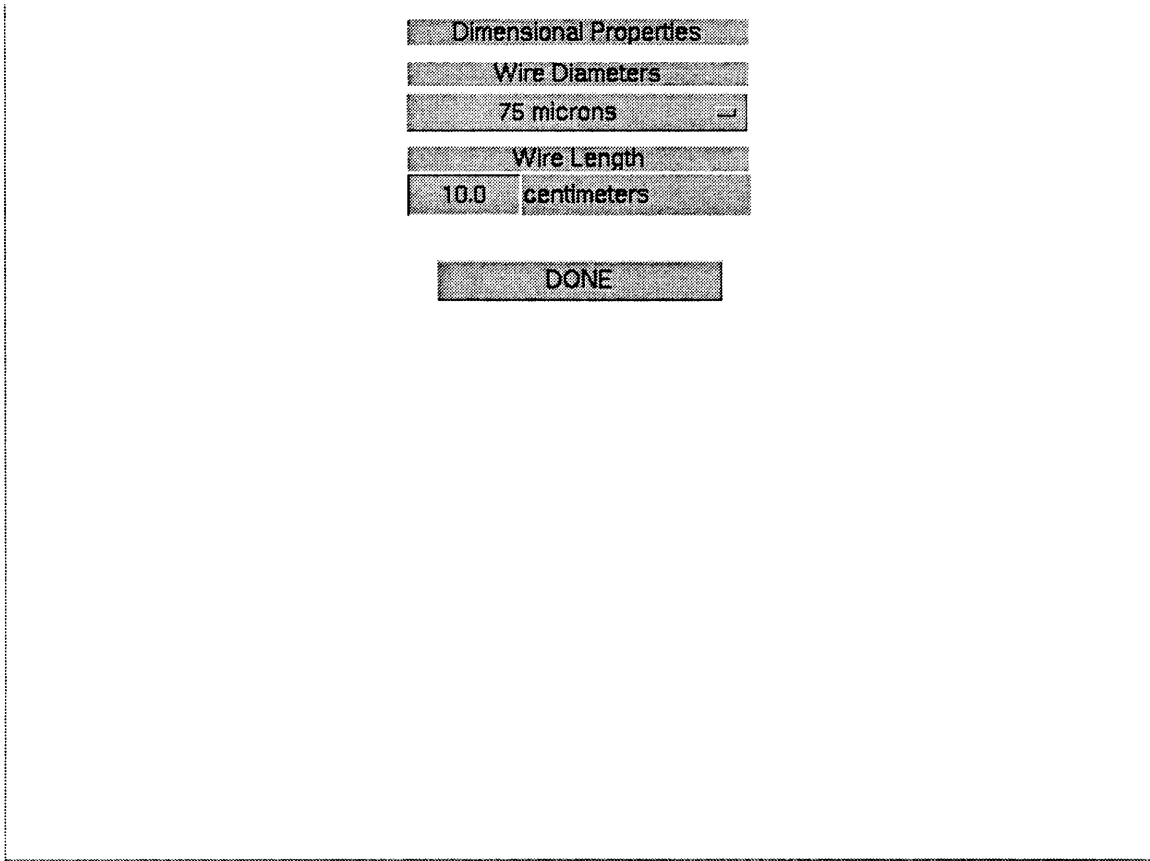


Figure A3. The “Flexinol 90-110 Wires” screen.

Figure A3 shows the resulting window when the “Flexinol 90-110 Wire” choice is made. The length of the wire can be defined. Existing wire diameters of 25, 50, 75, 100, 150 and 250 microns can be chosen. The wires are heat-treated at 425°C for 1 hour and pre-cycled 200 hundred times under a 200 MPa stress.

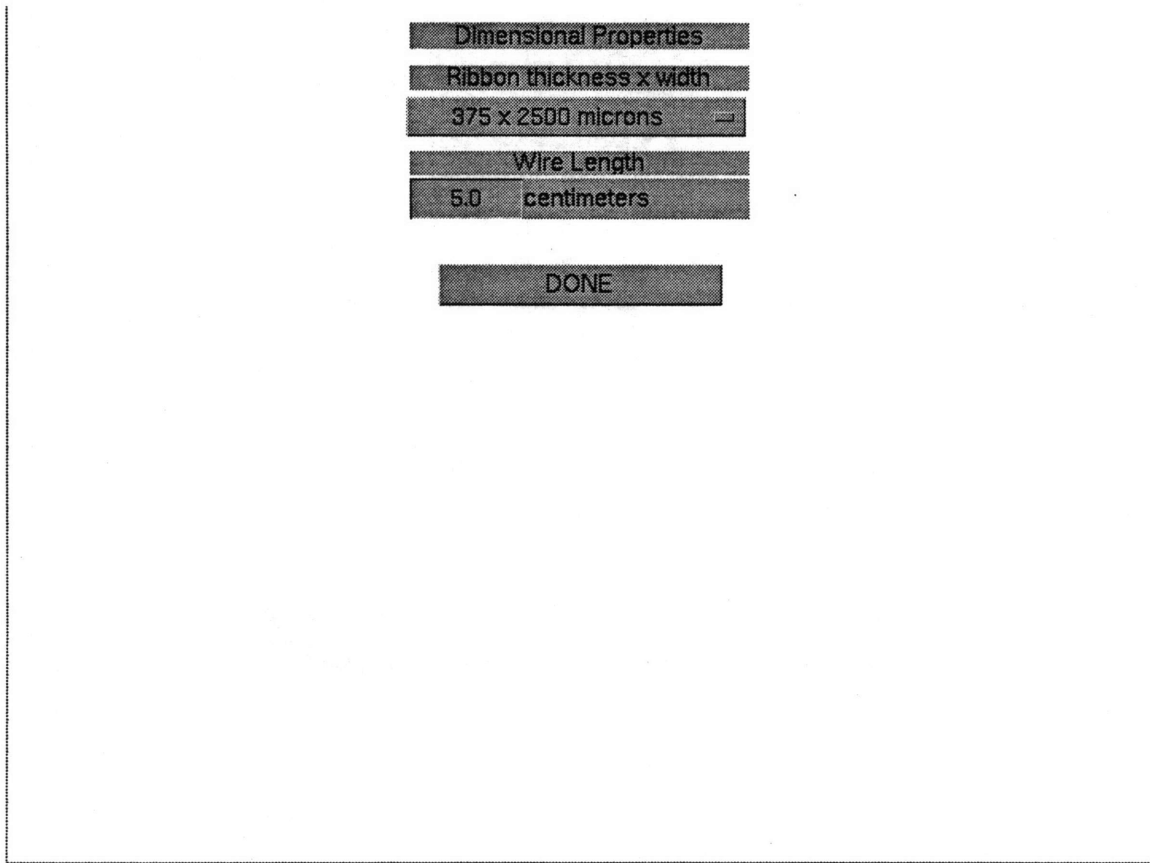


Figure A4. The “Mondo-tronics Ribbon Wires” screen.

Figure A4 shows the resulting window when the “Mondo-tronics Ribbon” choice is made. The length of the wire can be defined. Existing wire cross-sections of 375 x 2500 microns, and 500 x 2250 microns can be chosen. The wires are heat treated at 425°C for 1 hour and are not pre-cycled.

Dimensional Properties	Physical Properties	Manufacturing Properties
Select Wire Cross Section	Density	Heat-Treat Temperature
Circular	6.45e3 kg/(m <sup>3</sup> )	425 (C)
Diameter	Resistivity	Pre-Cycled Wire?
25 Microns	80e-8 Ohm-meters	no
Wire Length	Constant Specific Heat	Strain at As
5.0 centimeters	837.4 J/(kg-K)	.005 m/m
	Latent Heat	Strain at Mf
	24.2e3 J/kg	.005 m/m
	Martensite Modulus	Strain at Af
	28.0 GPa	.04 m/m
	Austenite Modulus	
	75.0 GPa	
	Martensite Yield Stress	
	224 MPa	
	Austenite Yield Stress	
	600 MPa	
	DONE	

Figure A5. The “Create Your Own Wires” screen.

Figure A5 shows the resulting window when the “Create Your Own” choice is made. This screen allows the designer to modify the dimensional, physical and manufacturing properties of a  $\text{Ni}_{49}\text{Ti}_{51}$  wire. The cross-section can be either circular or rectangular (ribbon wire). The heat-treatment temperature can be either 400°C, 425°C or 600°C. The wire can either be pre-cycled 200 times under a 200 MPa stress, or not be pre-cycled. The hysteresis curve relating the temperature strain ( $\epsilon_T$ ) to the wire temperature ( $T_w$ ) can be modified. This modification can be accomplished by defining the temperature strain ( $\epsilon_T$ ) at the Austenite Start (As), Austenite Finish (Af), and Martensite Finish (Mf) temperatures.

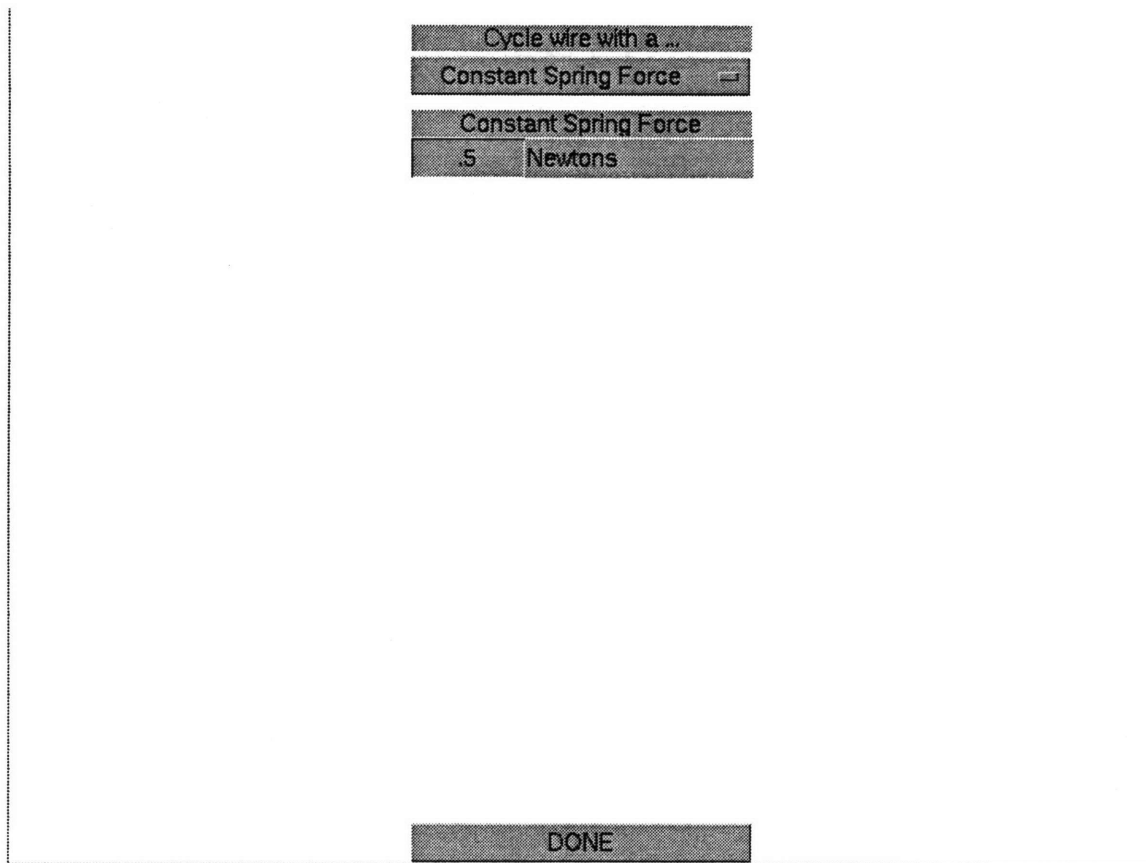


Figure A6. The “Create Force History” screen (constant force bias option).

Figure A6 shows the resulting screen when the designer has selected a constant force bias spring after selecting the “Create Force History” option from the design menu. Figures A2 through A6 show how the designer could simulate an electrically-heated  $\text{Ni}_{49}\text{Ti}_{51}$  wire actuating a constant force bias spring with the following parameters:

A Flexinol 90-110 wire with:

- 75 micron diameter
- 10.0 centimeter length
- 18.11 Ohm wire resistance

The environmental temperature is 10°C.

The electrical square wave has the following parameters:

- $V_h$  is 3.0 Volts for 2.0 seconds ( $t_h$ )
- $V_l$  is 0.0 Volts for 2.0 seconds ( $t_l$ )
- The load resistance ( $R_l$ ) is 0 Ohms

The constant spring force bias ( $F_c$ ) was .5 Newtons.

Cycle 1,000 was simulated.

A plot of the wire temperature ( $T_w(t)$ ) on the x-axis and the temperature strain ( $eT(t)$ ) on the y-axis resulted.

The plotted results were labeled "Temperature-Strain Curve." The curve is plotted in Figure A7.

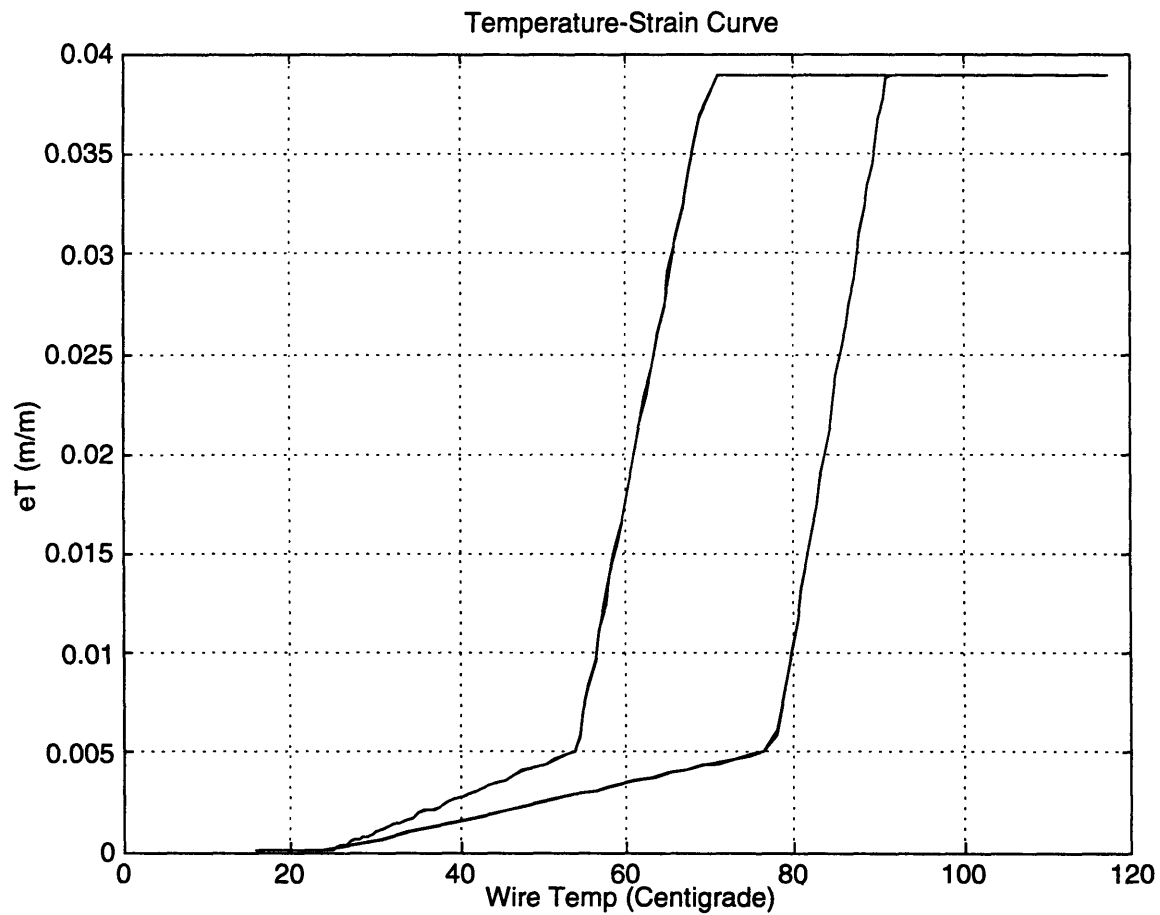


Figure A7. Simulated temperature-strain curve for  $Ni_{49}Ti_{51}$  wire.

In a similar manner, the designer can simulate a linear bias springed  $Ni_{49}Ti_{51}$  wire.

**A.2 Simulating an electrically-heated  $Ni_{49}Ti_{51}$  wire actuating a linear bias spring.**

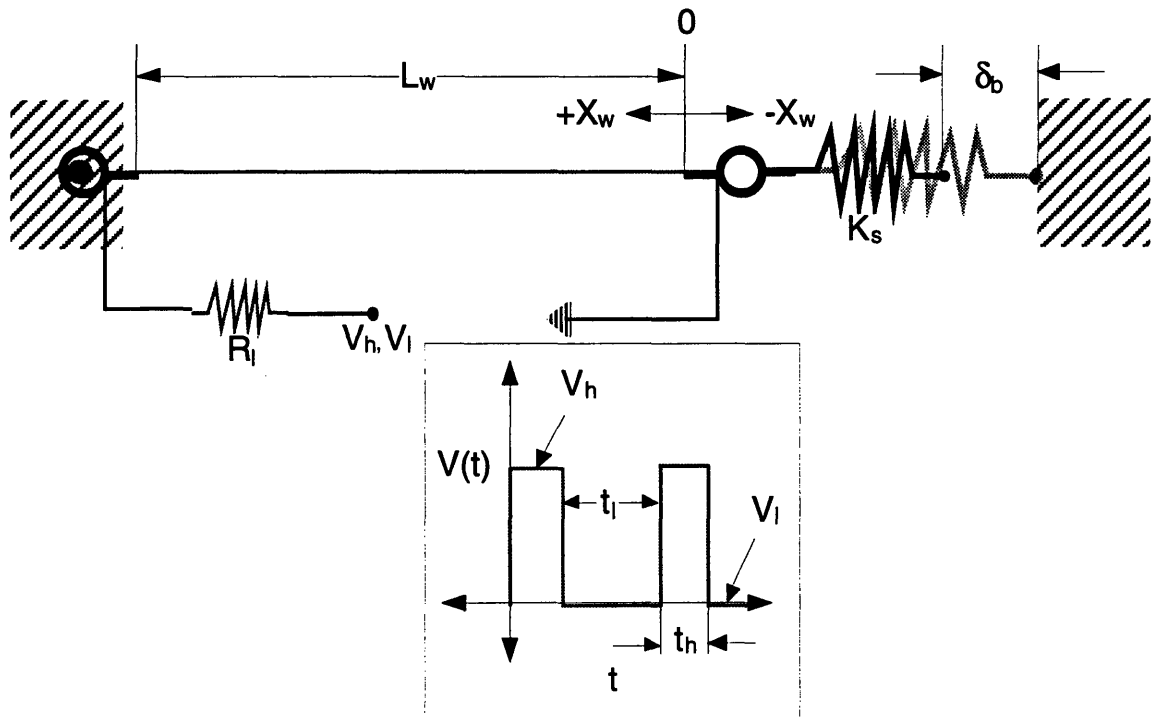


Figure A8. An electrically-heated  $Ni_{49}Ti_{51}$  wire actuating a linear bias spring.

Figure A8 shows the new arrangement when the  $Ni_{49}Ti_{51}$  wire has a linear bias spring. The information the designer needs to supply is almost identical to the information required for the constant force bias simulation. The new information needed is the spring stiffness ( $K_s$ ) and the system bias spring ( $\delta_b$ ). Note that the  $Ni_{49}Ti_{51}$  wire position ( $X_w$ ) is based on its length before it is elongated by the bias spring.

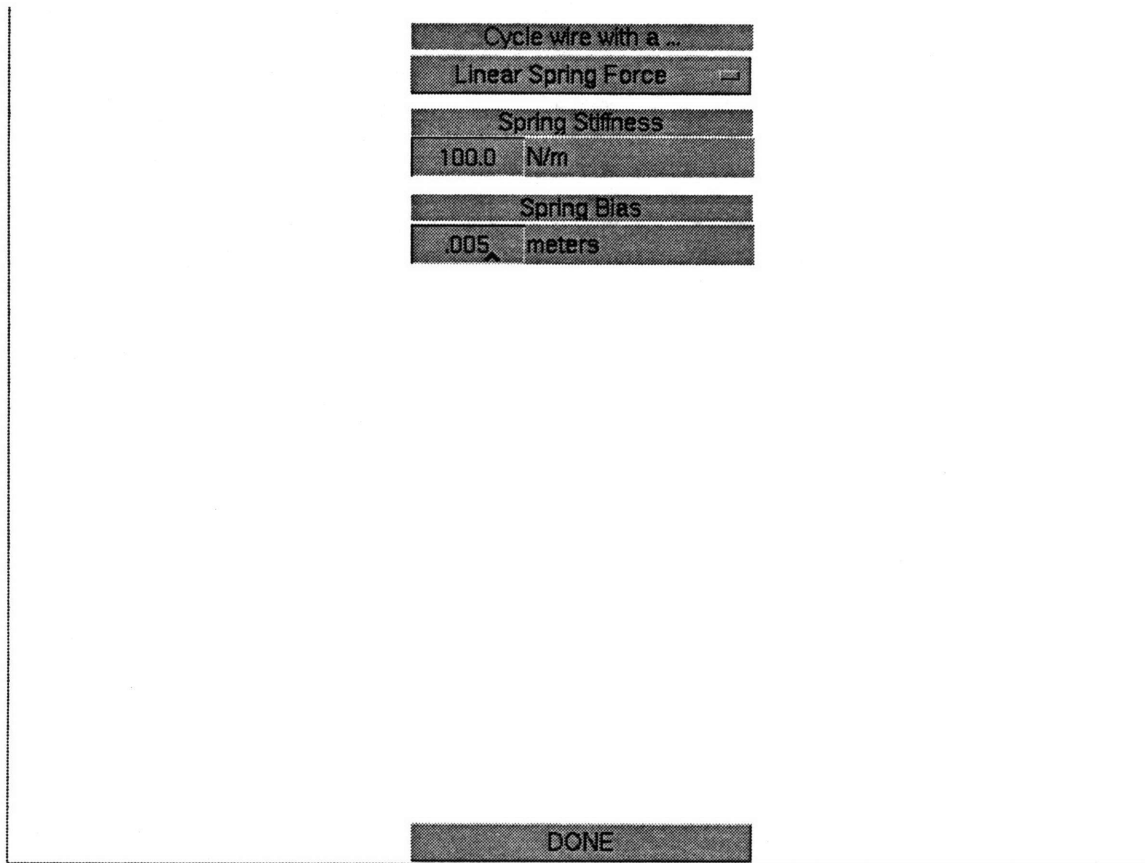


Figure A9. The “Create Force History” screen (linear bias spring option).

Figure A9 shows the resulting interface after “Create Force History” and the “Linear Spring Force” options are selected. A linear spring with a stiffness of 100.0 N/m and a .005 meter bias was chosen. Using the previous simulation inputs in Figures A2 and A3, along with the input in Figure A9, the resulting wire stress can be plotted with respect to time.

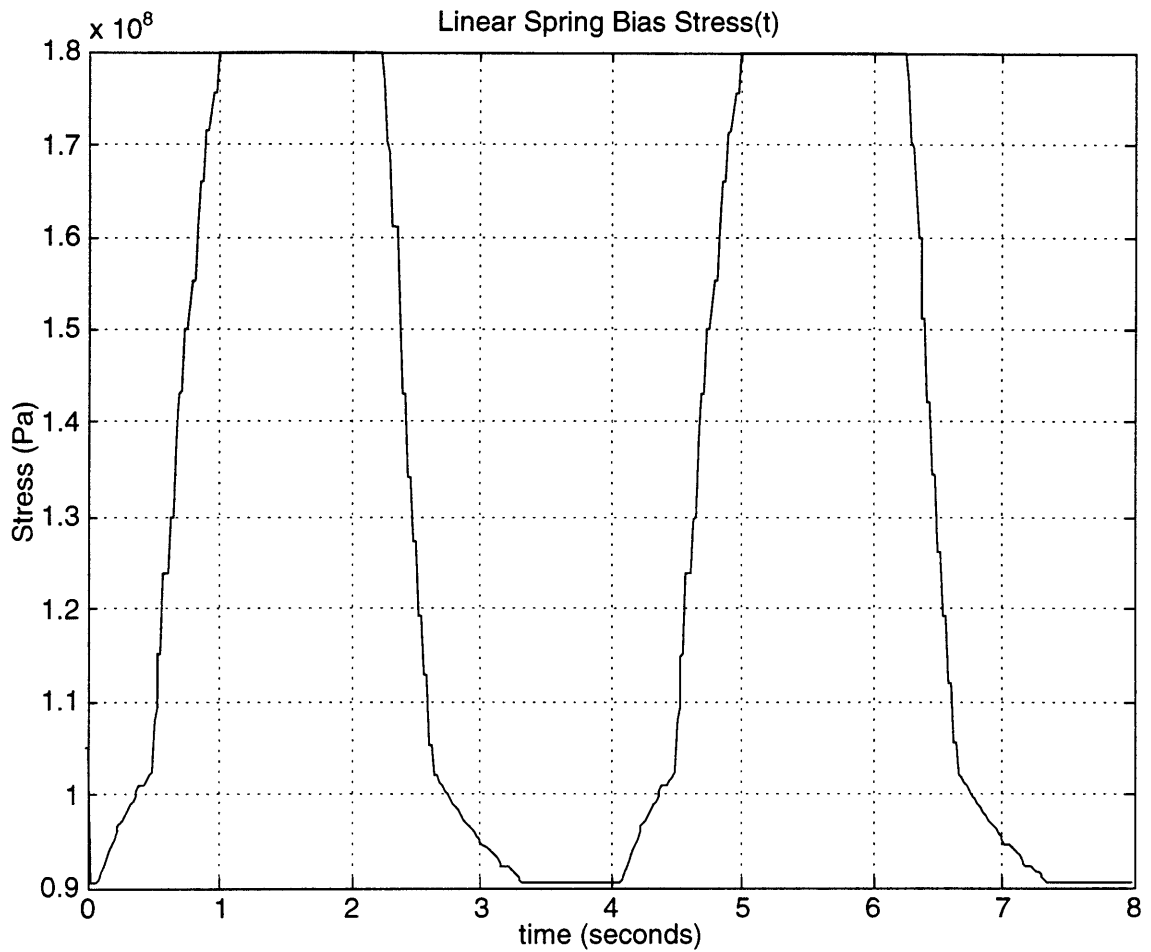


Figure A10. Simulated stress-time curve for Ni<sub>49</sub>Ti<sub>51</sub> wire.

Figure A10 shows the changing stress in the Ni<sub>49</sub>Ti<sub>51</sub> wire as it contracts when heated and extends when cooled. Note that the Ni<sub>49</sub>Ti<sub>51</sub> wire was cycled twice by the electrical square wave.

**A.3 Simulating a bi-stable mechanism employing  $Ni_{49}Ti_{51}$  wires and permanent magnets.**

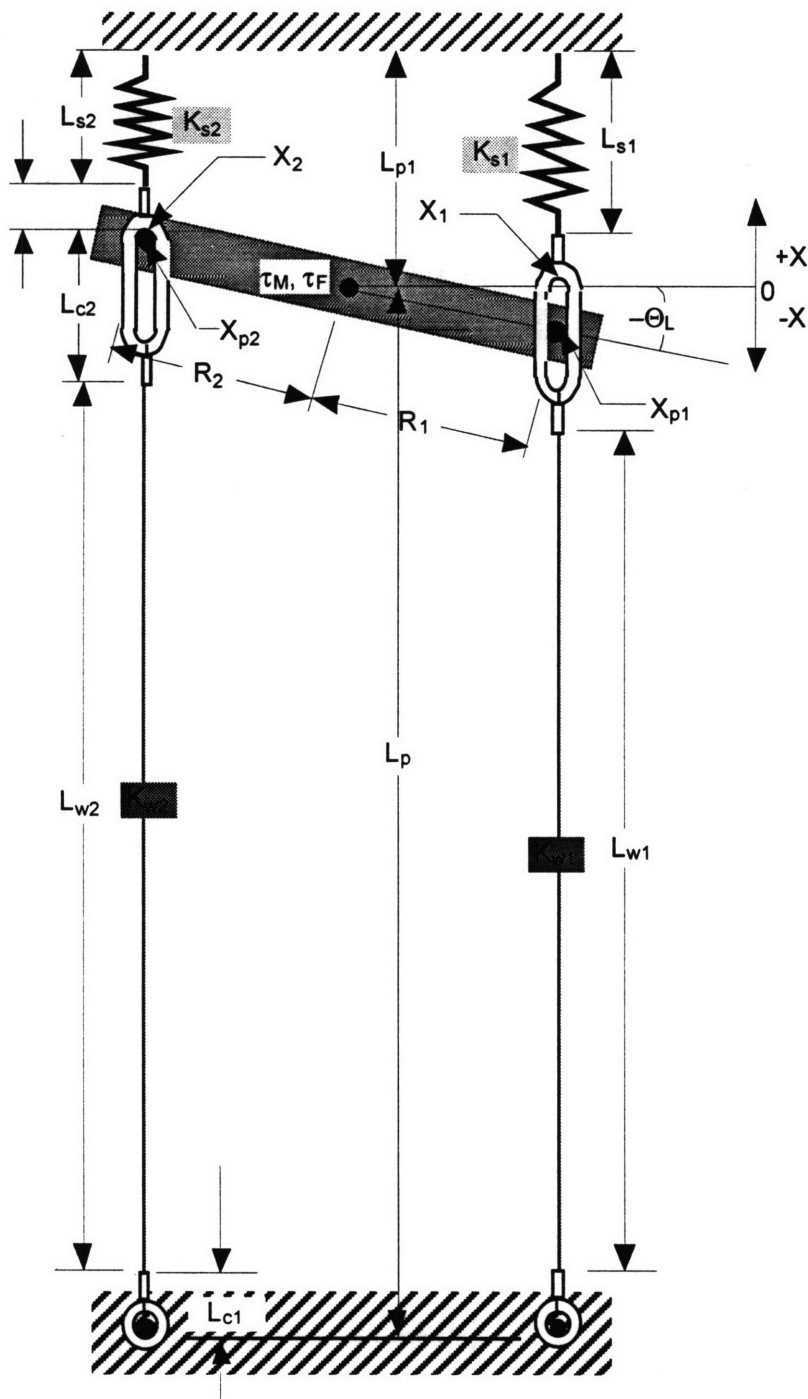


Figure A11. A bi-stable mechanism employing  $Ni_{49}Ti_{51}$  wires and permanent magnets.

Figure A11 illustrates the system which the designer wants to simulate. The system consists of 2 springs biasing 2 Ni<sub>49</sub>Ti<sub>51</sub> wires which are actuating a lever. The lever has a magnetic and friction torque history dependent on its velocity and position. There are 2 pins on the lever which, with the wire connectors, enable the contracting Ni<sub>49</sub>Ti<sub>51</sub> wires to actuate the lever. Figure A11 does not show that the Ni<sub>49</sub>Ti<sub>51</sub> wires are heated electrically with their corresponding load resistors and voltage source. The following discussion will show how to simulate the system illustrated in Figure A11.

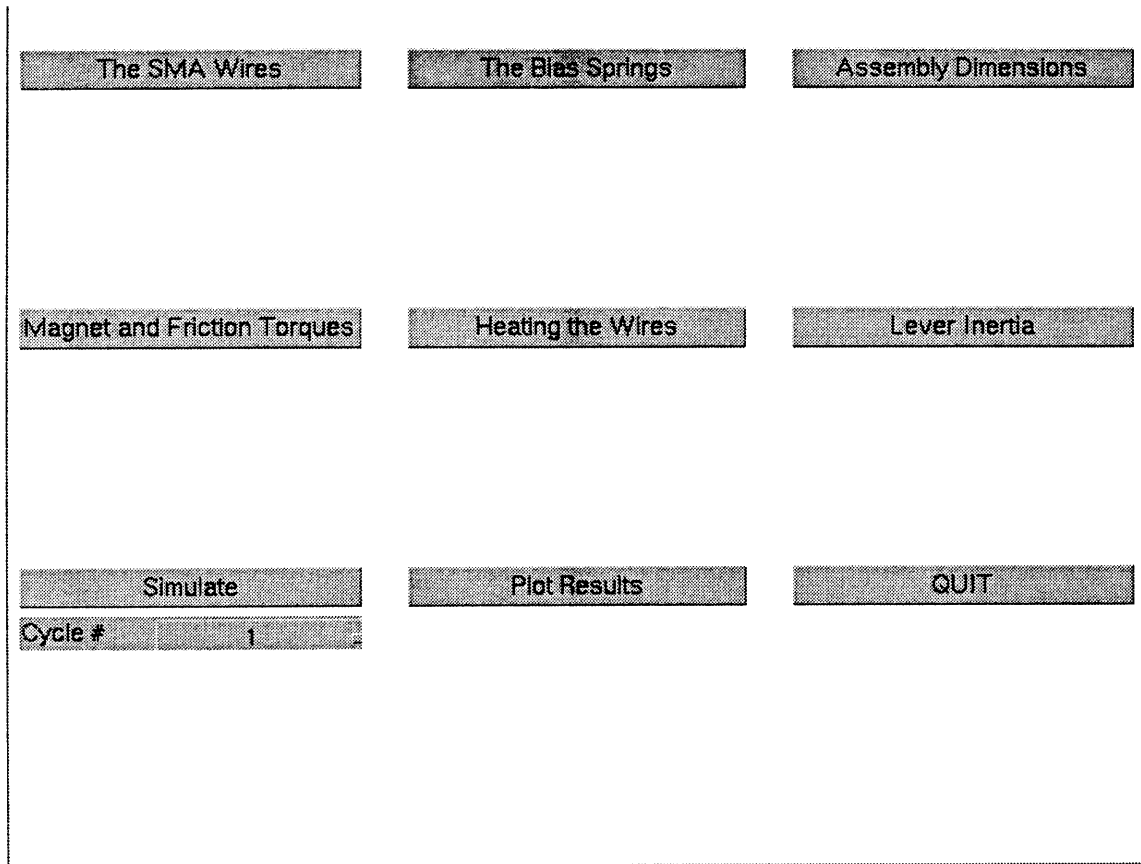


Figure A12. Main menu used to simulate a bi-stable mechanism employing Ni<sub>49</sub>Ti<sub>51</sub> wires and permanent magnets.

Figure A12 illustrates the main menu of the computer simulation program. It consists primarily of push-buttons, which bring the user to different screens to create various aspects of the system presented in Figure A11. Pressing “The SMA Wires” button brings the designer to a screen similar to the one illustrated in Figure A13.

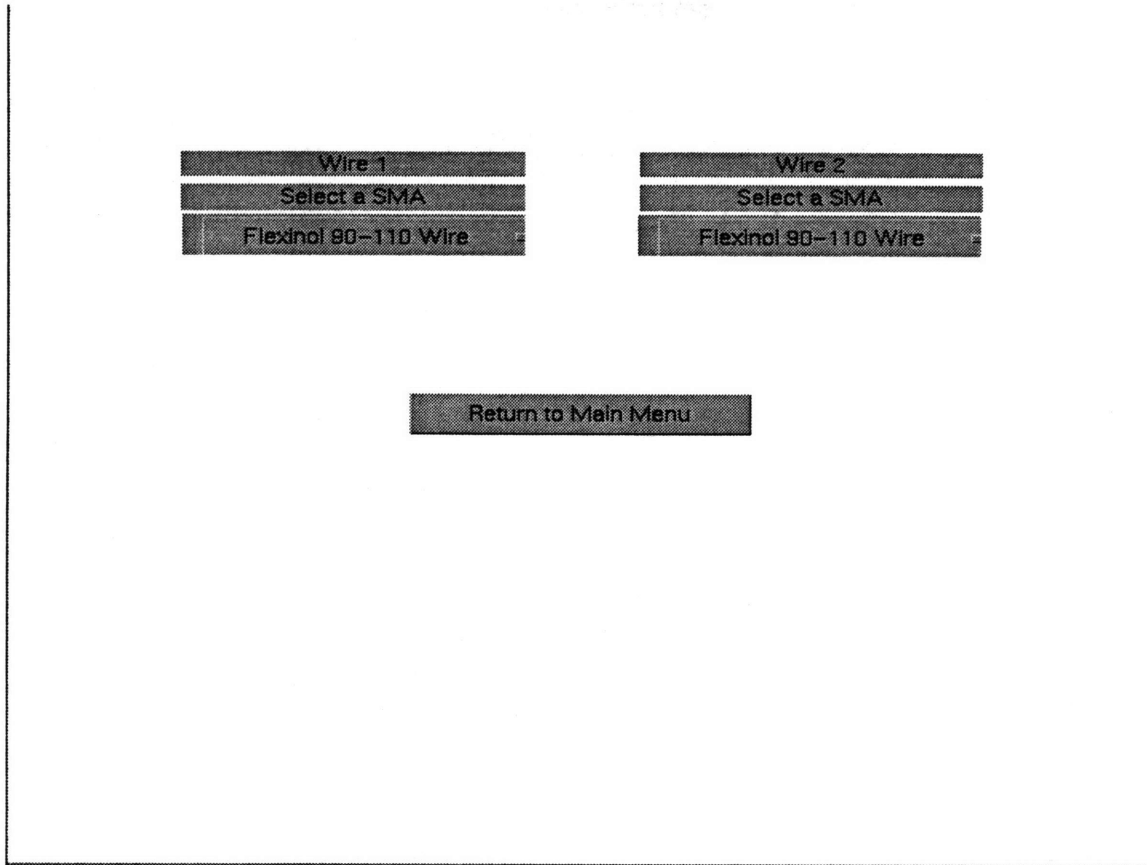


Figure A13. The “SMA Wires” screen.

This screen allows the designer to define the properties of the 2  $\text{Ni}_{49}\text{Ti}_{51}$  wires illustrated in Figure A11. Under the “Wire 1” and “Wire 2” sections the designer can select from three possible wires. The “Flexinol 90-110 Wire” option leads the designer to a screen similar to the one illustrated in Figure A3. The “Mondo-tronics Ribbon” option leads the designer to a screen similar to the one illustrated in Figure A4. The “Create Your Own” option leads the designer to a screen similar to the one illustrated in Figure A5. These screens allow the designer to define the length of wire 1 ( $L_{w1}$ ), the length of wire 2 ( $L_{w2}$ ) and the cross-sections of these wires. This allows the corresponding wire stiffness ( $K_{w1}$  and  $K_{w2}$ ) to be calculated.

In this discussion the user chose wires 1 and 2 to be Flexinol 90-110 wires with the following dimensions:

$L_{w1}$  is 4.05 centimeters and  $D_{w1}$  is 75 microns

$L_{w2}$  is 4.05 centimeters and  $D_{w2}$  is 75 microns

Pressing the “Return to Main Menu” button brings the designer back to the main menu. Pressing “The Bias Springs” button then brings the designer to a screen similar to the one illustrated in Figure A14.

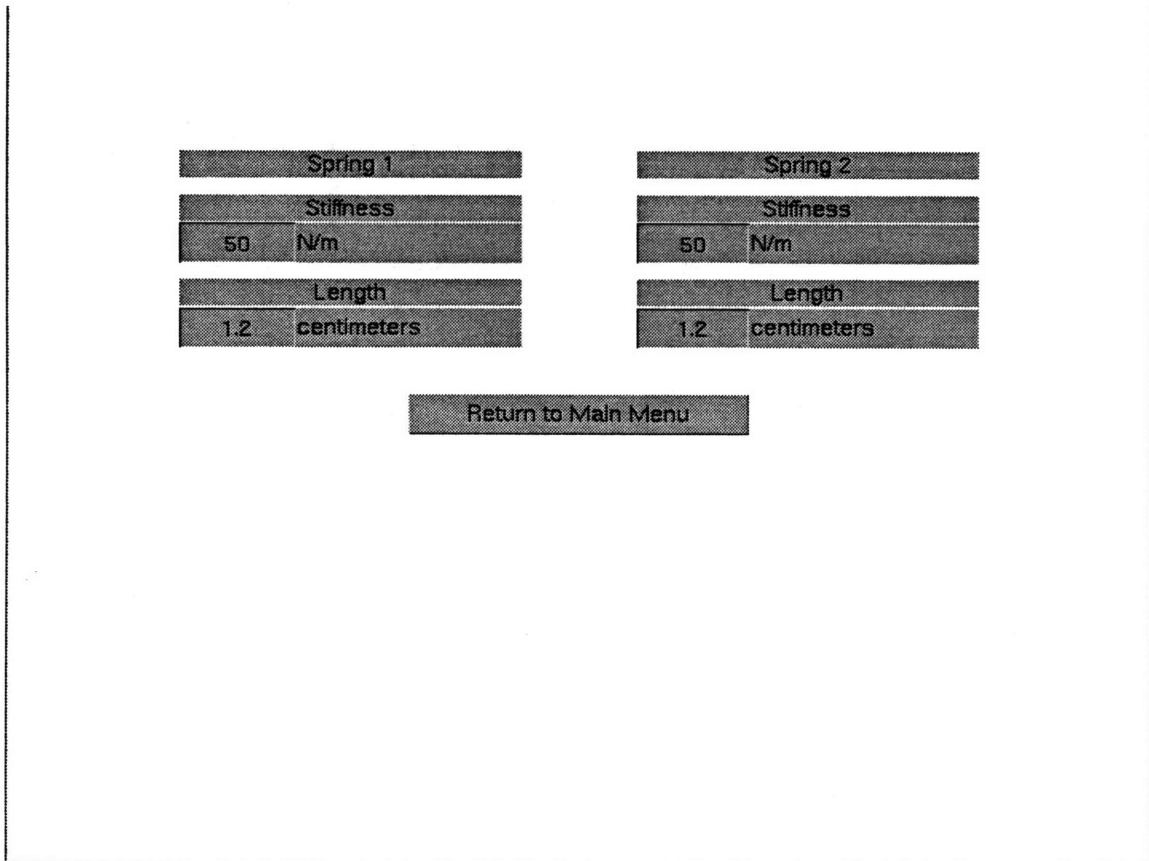


Figure A14. The “Bias Springs” screen.

This screen allows the designer to define the properties of the 2 bias springs illustrated in Figure A11. Under the “Spring 1” and “Spring 2” sections the designer defines the corresponding spring stiffness and length.

In this discussion the designer chose the spring stiffness and length as follows:

$K_{s1}$  is 50.0 N/m and  $L_{s1}$  is 1.2 centimeters

$K_{s2}$  is 50.0 N/m and  $L_{s2}$  is 1.2 centimeters

Pressing the “Return to Main Menu” button brings the designer back to the main menu. Pressing the “Assembly Dimensions” button then brings the designer to a screen similar to the one illustrated in Figure A15.

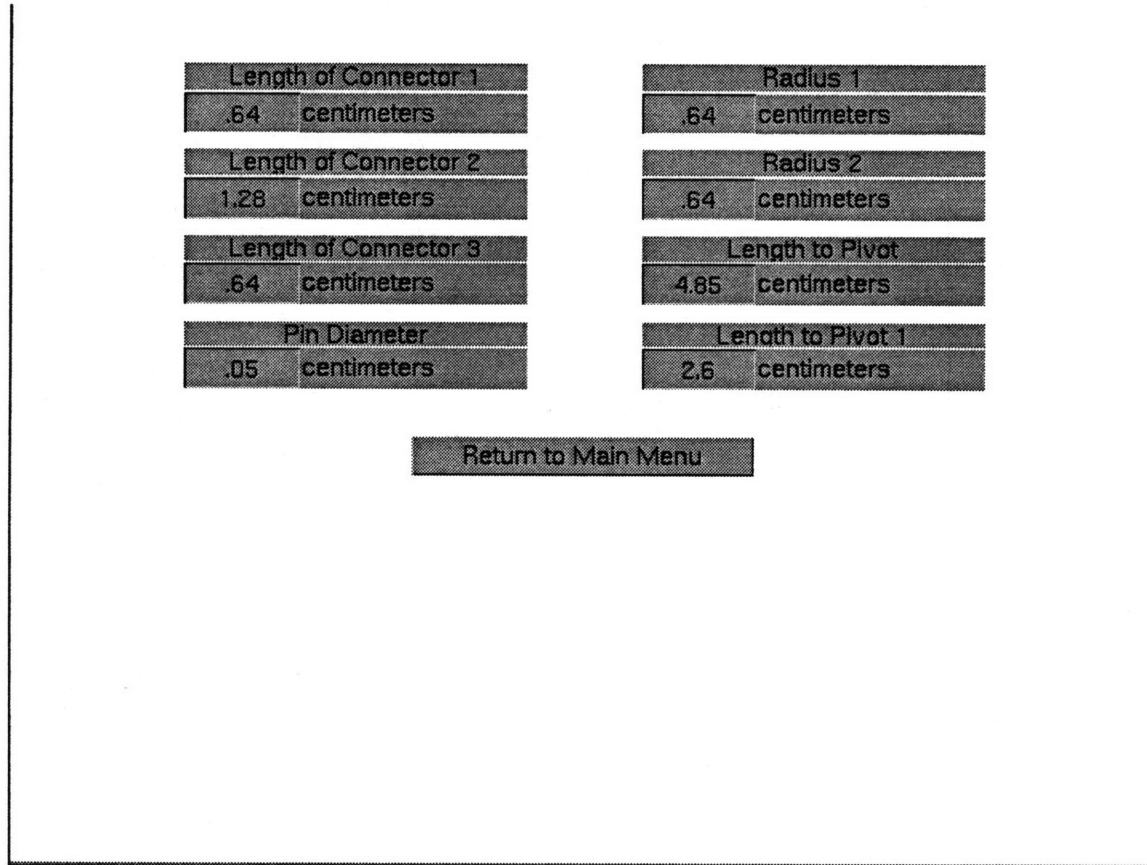


Figure A15. The “Assembly Dimensions” screen.

This screen allows the designer to define the remaining dimensions of the connectors and pins illustrated in Figure A11.

In this discussion the designer chose the assembly dimensions as follows:

Length of connector 1 ( $L_{c1}$ ) is	0.64 centimeters
Length of connector 2 ( $L_{c2}$ ) is	1.28 centimeters
Length of connector 3 ( $L_{c3}$ ) is	0.64 centimeters
Pin Diameter on Lever was	0.05 centimeters

Radius 1 of pin on lever ( $R_1$ ) is 0.64 centimeters  
 Radius 2 of pin on lever ( $R_2$ ) is 0.64 centimeters  
 Length to pivot from bottom ( $L_p$ ) is 5.85 centimeters  
 Length to pivot from top ( $L_{p1}$ ) is 2.60 centimeters

Pressing the “Return to Main Menu” button brings the designer back to the main menu. Pressing the “Magnet and Friction Torque” button then brings the designer to a screen similar to the one illustrated in Figure A16.

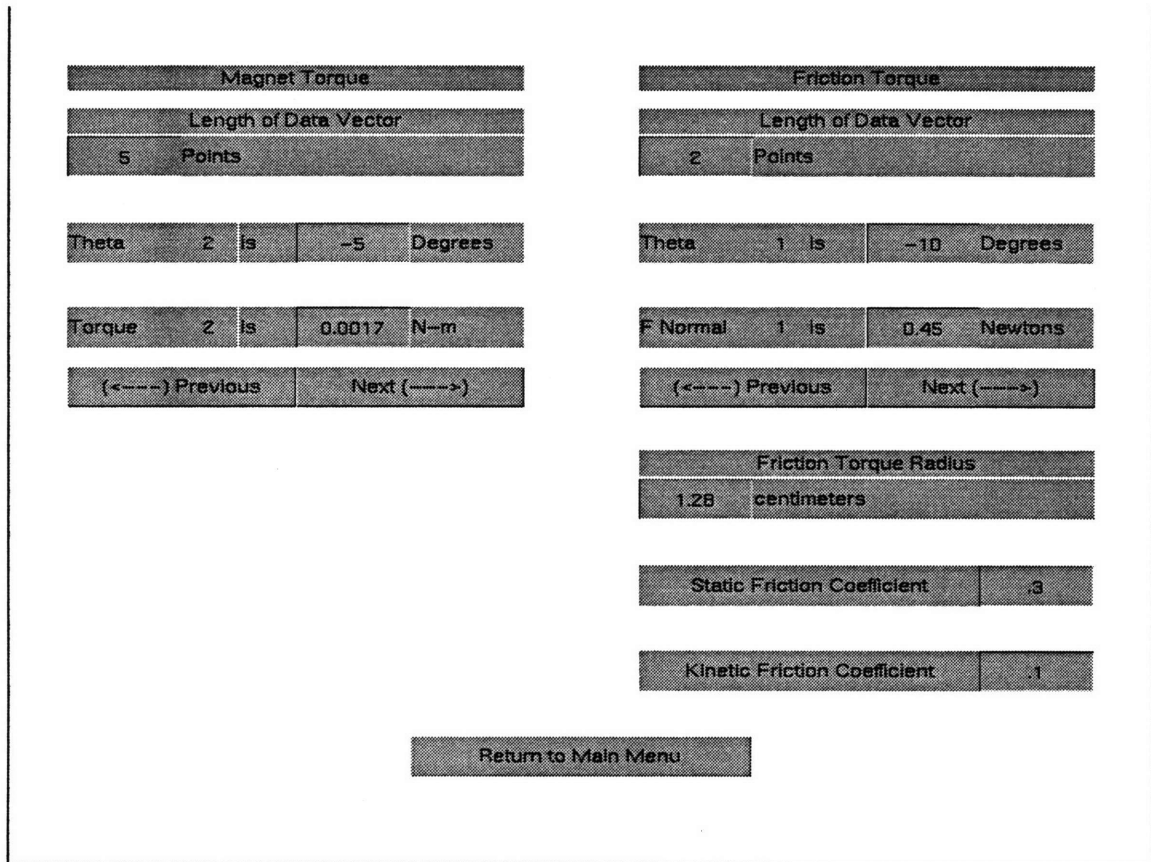


Figure A16. The “Magnet and Friction Torque” screen.

This screen allows the designer to create an actuating magnetic torque history for the lever. It also allows the designer to create a friction torque history for the lever as well.

In the “Magnet Torque” section the designer creates 2 data vectors which relate lever angular position ( $\theta_l$ ) to the magnetic torque ( $\tau_M$ ).

In the “Friction Torque” section the designer creates 2 data vectors which relate lever angular position to the force normal to the surface on which the lever is mounted. The radius ( $R_f$ ) at which this normal force acts on the lever, the static ( $\mu_s$ ) and kinetic ( $\mu_k$ ) coefficients of friction, are required to create the friction torque ( $\tau_f$ ).

The simulation sorts and interpolates the points given by the user. If the angle of the lever is either greater or lesser than the values supplied by the user, the simulation program will use the value closest to the given limits.

In this discussion the designer created the following torque histories, shown in Figure A17:

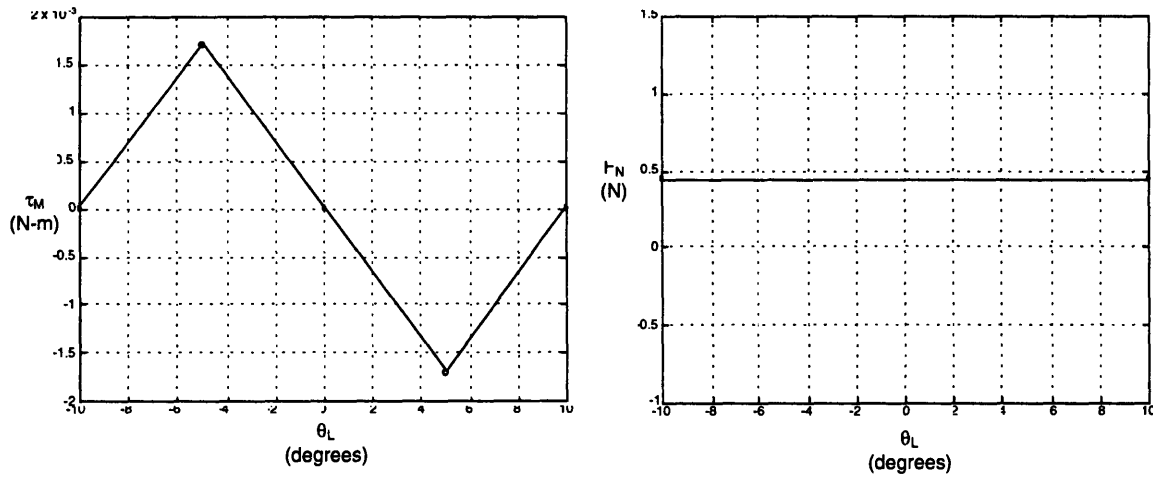


Figure A17. Magnetic torque-angular position and normal force-angular position curves.

Figure A16 shows that the magnetic torque vector needed only 5 points, and the normal force curve needed only 2 points. The vector inputs were as follows:

$\tau_M$  is [0 .0017 0 -.0017 0] N-m, with  $\theta_L$  being [-10 -5 0 5 10] degrees.

$F_N$  is [.45 .45] Newtons, with  $\theta_L$  being [-10 10] degrees.

The corresponding friction torque radius and coefficients are as follows:

$R_f$  is 1.28 centimeters

$\mu_s$  is .3

$\mu_k$  is .1

Pressing the “Return to Main Menu” button brings the designer back to the main menu. Pressing the “Heating The Wires” button then brings the designer to a screen similar to the one illustrated in Figure A18.

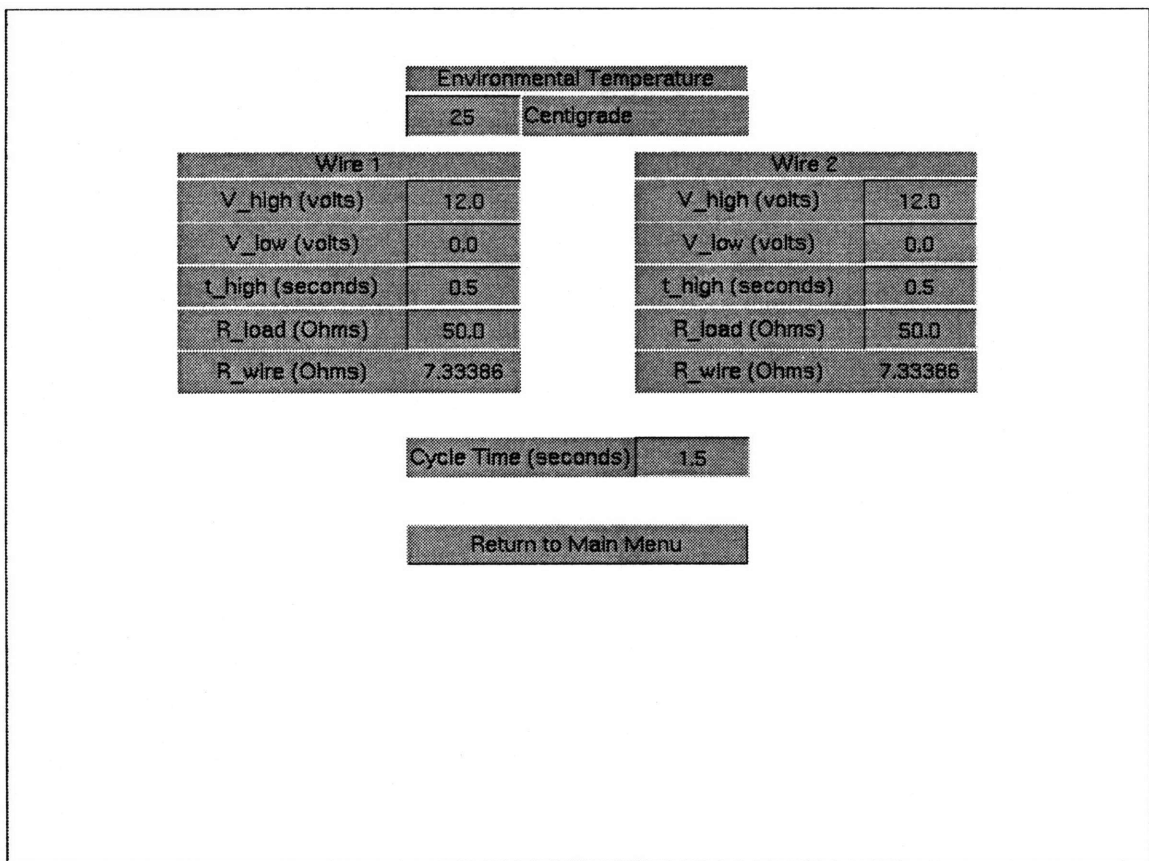


Figure A18. The “Heating The Wires” screen.

This screen allows the designer to create the electrical square waves which heat the 2 wires, and to select the load resistors ( $R_{l1}$  and  $R_{l2}$ ) for the 2 wires. Finally, it allows the designer to define the environmental temperature ( $T_{env}$ ).

Figure A19 shows how the high times for wires 1 and 2 ( $t_{h1}$  and  $t_{h2}$ ) and their high and low voltages ( $V_{h1}$ ,  $V_{l1}$  and  $V_{h2}$ ,  $V_{l2}$ ) relate to the cycle time ( $t_c$ ):

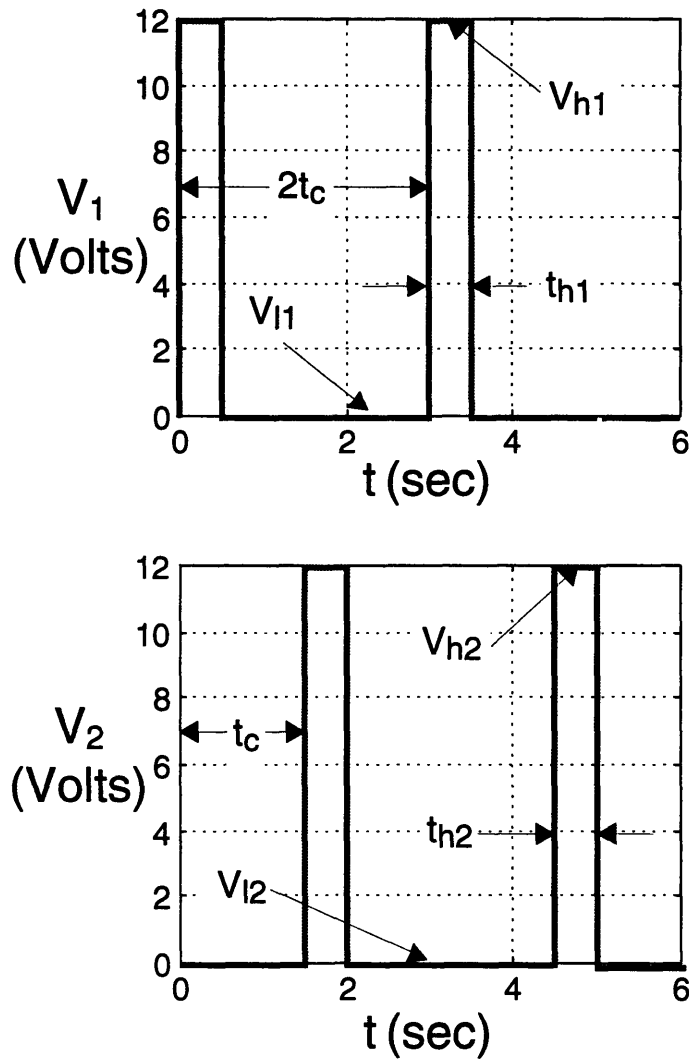


Figure A19. Electrical square wave to heat  $Ni_{49}Ti_{51}$  wires.

In this discussion the designer chose the heating parameters as follows:

$V_{h1}$	12.0	Volts
$t_{h1}$	0.5	seconds
$R_{l1}$	50.0	Ohms
$V_{h2}$	12.0	Volts
$t_{h2}$	0.5	seconds

$R_{12}$  50.0 Ohms  
 $t_c$  1.5 seconds

Pressing the “Return to Main Menu” button brings the designer back to the main menu. Pressing the “Lever Inertia” button then brings the designer to a screen similar to the one illustrated in Figure A20.

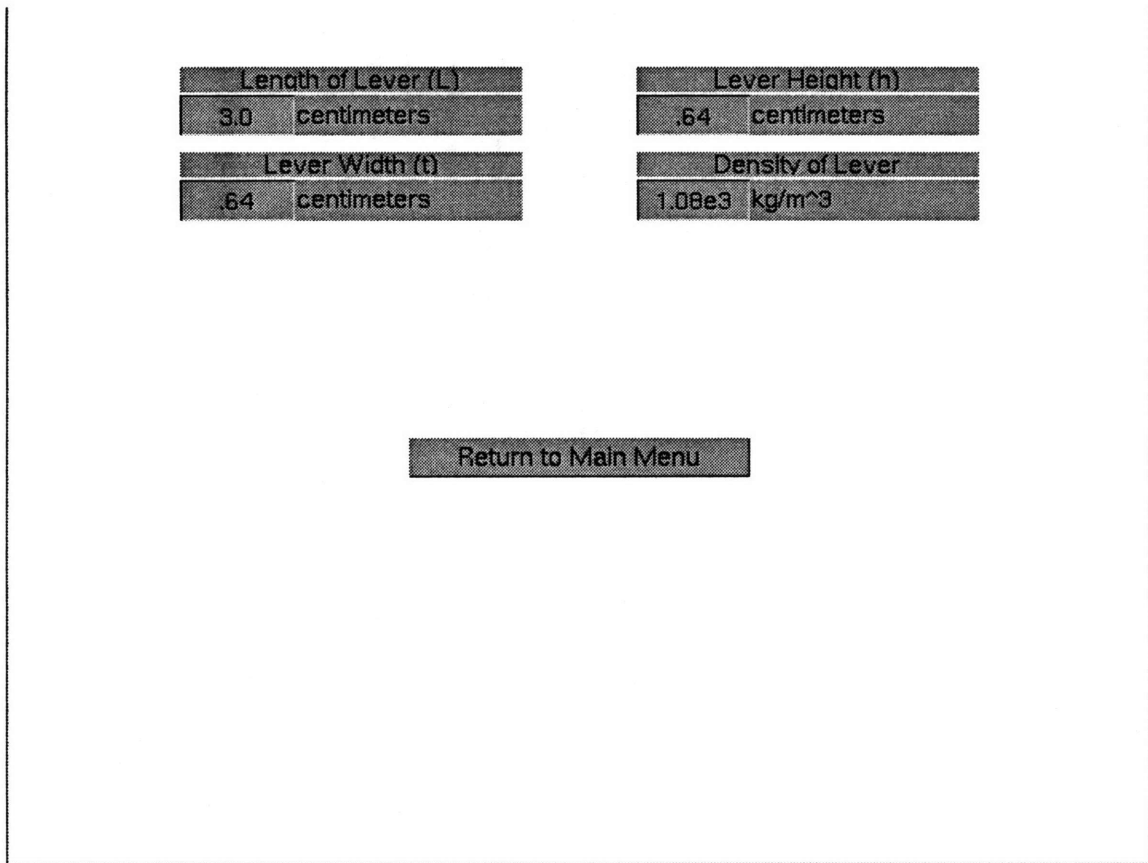


Figure A20. The “Lever Inertia” screen.

This screen allows the designer to define the dimensions and density of the lever. The lever dimensions consist of the length, width and height.

In this discussion the designer chose the lever dimensions and density as follows:

length 3.0 centimeters  
width 0.64 centimeters

height 0.64 centimeters

density 1,080 kg/m<sup>3</sup>

Pressing the “Return to Main Menu” button brings the designer back to the main menu. The designer chooses to simulate the first cycle, and then presses the “Simulate” button. After the simulation is completed, the designer presses the “Plot Results” button, which brings the designer to a screen similar to the one illustrated in Figure A21.

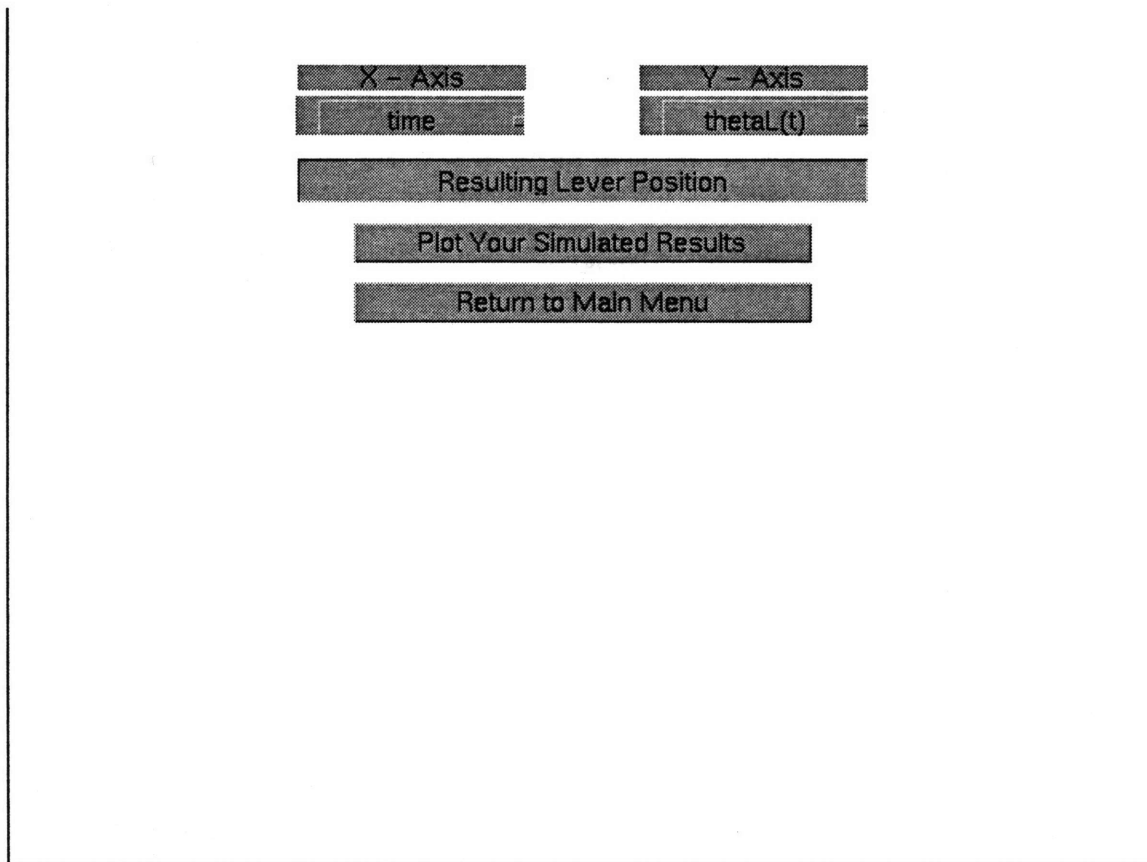


Figure A21. The “Plot Results” screen.

This screen allows the designer to plot the results of the simulation. Variables which can be plotted on the x and y axes are as follows:

- time (seconds)
- thetaL(t) (degrees), which is the lever angular position

- $T_{w1}(t)$  (Centigrade), which is the temperature of wire 1
- $T_{w2}(t)$  (Centigrade), which is the temperature of wire 2
- $e_{T1}(t)$  (m/m), which is the temperature strain of wire 1
- $e_{T2}(t)$  (m/m), which is the temperature strain of wire 2
- $L_{w1}(t)$  (meters), which is the changing length of wire 1
- $L_{w2}(t)$  (meters), which is the changing length of wire 2
- $S_{w1}(t)$  (Pa), which is the stress in wire 1
- $S_{w2}(t)$  (Pa), which is the stress in wire 2
- $X1(t)$  (meters), which is  $(L_{w1} + L_{c2} - L_p)$
- $X2(t)$  (meters), which is  $(L_{w2} + L_{c2} - L_p)$
- $F_{w1}(t)$  (Newtons), which is the resulting tension in wire 1
- $F_{w2}(t)$  (Newtons), which is the resulting tension in wire 2

In this discussion the designer chose to plot time on the x-axis and  $\theta_L(t)$  on the y-axis, with the title “Resulting Lever Position.” This plot is illustrated as follows:

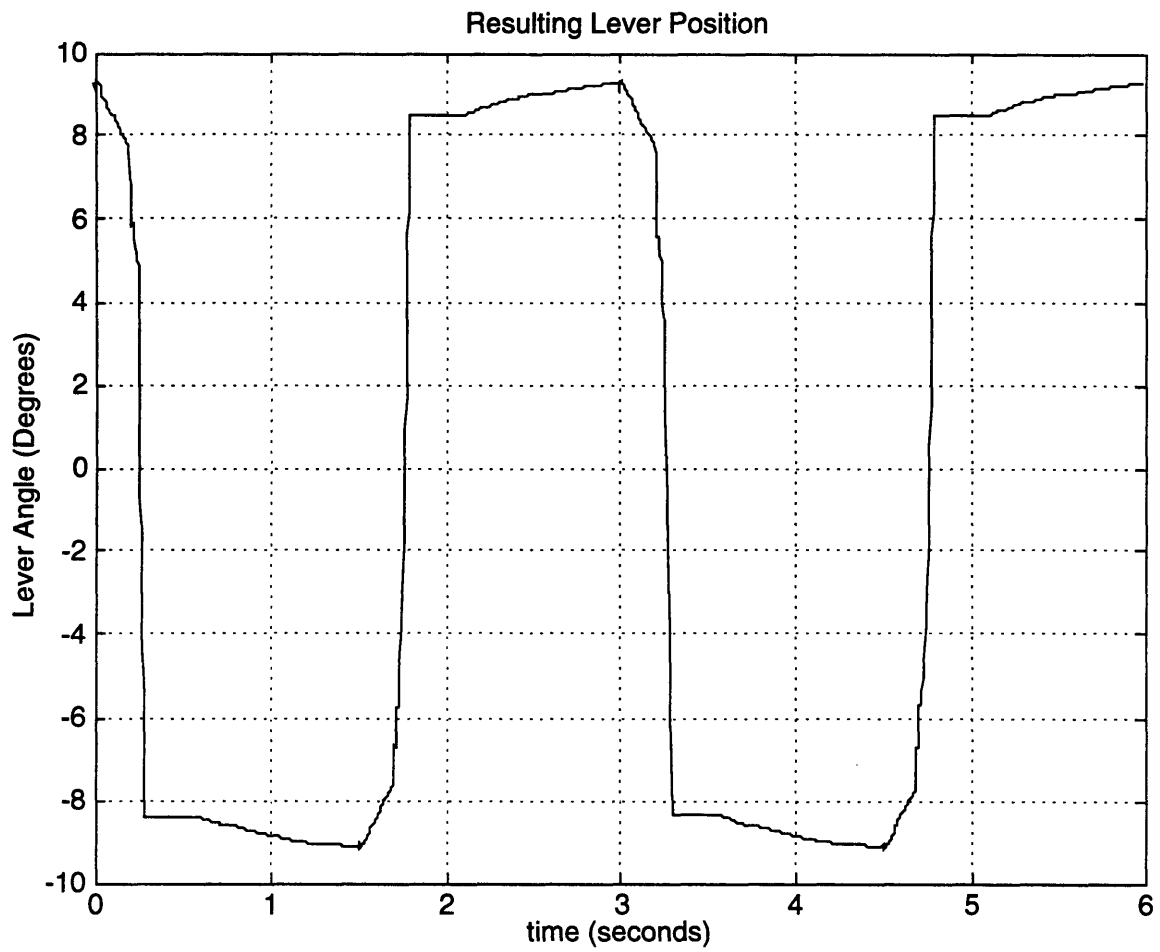


Figure A22. Simulated angular position-time curve for steel lever.

## Appendix B: Modeling Shape Memory Alloys

Figure B1 illustrates the general structure used to model a Shape Memory Alloy. A voltage ( $V(s)$ ) is applied to a SMA in order to heat it electrically. A first-order dynamic model is used to represent the heating and cooling of the isothermal SMA. Incorporating the room temperature ( $T_{env}(s)$ ) with the change in wire temperature ( $\theta(s)$ ) allows the wire temperature ( $T_w(s)$ ) to be determined. The temperature of the wire is then fed into a hysteresis loop relating the temperature of the wire to the resulting temperature strain ( $\epsilon_T(s)$ ). The hysteresis loop has parameters which affect its overall shape. These parameters vary with the applied stress to the wire ( $\sigma$ ) and the transformation cycles it has completed ( $N$ ). After calculating the temperature strain, the desired strain ( $\epsilon_d(s)$ ) is calculated by subtracting out the creep strain ( $\epsilon_c(s)$ ) resulting from the stress and cycle history associated with the SMA. Multiplying the desired strain by the length of the wire ( $L_w$ ) allows the desired position of the wire ( $X_d(s)$ ) to be determined. Since the wire is not infinitely stiff, the desired position of the wire is subtracted from the stretch in the wire, and the resulting wire position ( $X_w(s)$ ) is determined.

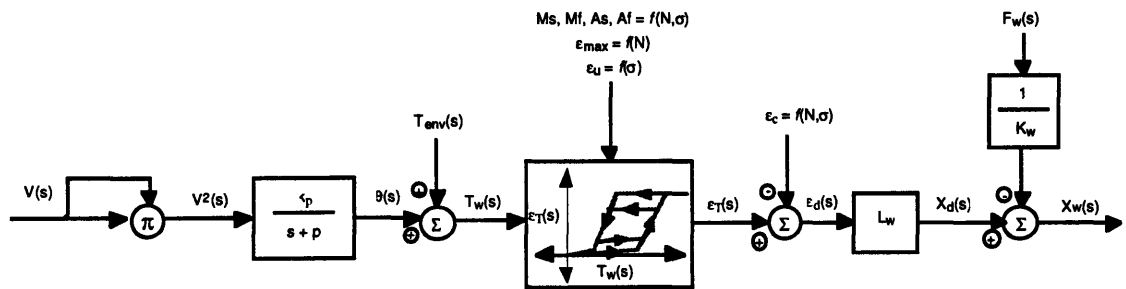


Figure B1. Generalized model for a Shape Memory Alloy.

Appendix B is concerned with describing the various aspects associated with the model in Figure B1. Section B.1 discusses the heat-transfer analysis applied to a SMA wire for free air convection and radiation cooling. Section B.2 discusses the modeling of the temperature-strain hysteresis curve. Section B.3 discusses the incorporation of creep and changing wire stiffness into the model to determine the actual position of the wire.

### B.1 Heat-transfer model of a Shape Memory Alloy wire.

A SMA heat-transfer model is discussed for an isothermal, air-cooled wire with a circular and a rectangular cross-section. Given the mass ( $m$ ), specific heat ( $C_p$ ), wire resistance ( $R_w$ ), heat-transfer coefficient ( $h_{env}$ ) and cooling surface area ( $A_w$ ), the dynamics relating the voltage to the change in wire temperature can be determined.

$$mC_p \left( \frac{dT_w}{dt} \right) = \frac{V_w^2(t)}{R_w} - h_{env} A_w (T_w - T_{env}) \quad (B1)$$

The temperature change is expressed as,  $\theta(t) = (T_w(t) - T_{env}(t))$  and  $\theta(0) = 0$ . Applying the Laplace transform to Equation B1 yields:

$$\frac{\theta(s)}{V_w^2(s)} = \frac{1}{mC_p R_w \left( s + \frac{h_{env} A_w}{mC_p} \right)} = \frac{k_p}{s + p} \quad (B2)$$

In order to implement Equation B2, the heat-transfer coefficient and specific heat need to be determined. Since Shape Memory Alloys undergo a phase transformation during actuation, their specific heat changes. Liang (1990) showed how to calculate the specific heat of the SMA by adding the constant specific heat ( $C_{po}$ ) to the product of the latent heat ( $l$ ), and the derivative of the percent of Austenite ( $\xi_A$ ) with respect to the changing wire temperature ( $T_w$ ).

$$C_p = C_{po} + l \frac{d\xi_A}{dT_w} \quad (B3)$$

White (1988) presents methods for calculating free-convection heat-transfer coefficients for horizontal cylinders and vertical plates (rectangular cross-section SMA wire). The following formulas are used to determine the heat transfer coefficient for a cylinder.

$$\text{Nu}_D = \frac{h_{\text{env}} D}{k_a} = \left( .60 + \frac{.387 \text{Ra}_D^{\frac{1}{4}}}{\left[ 1 + \left( \frac{.559}{\text{Pr}} \right)^{\frac{9}{16}} \right]^{\frac{8}{27}}} \right)^2 \quad (\text{B4})$$

This formula is valid for  $10^5 \leq \text{Ra}_D \leq 10^{12}$ , and for the average heat-transfer coefficient. The variables  $k_a$  (thermal conductivity for air), Pr (Prandtl number for air) and  $\text{Ra}_D$  (the Rayleigh number) can be determined by Figures B2-B4 and Equation B5. Figure B2 shows a curve-fit relating the thermal conductivity to  $T_{\text{env}}$  in air.

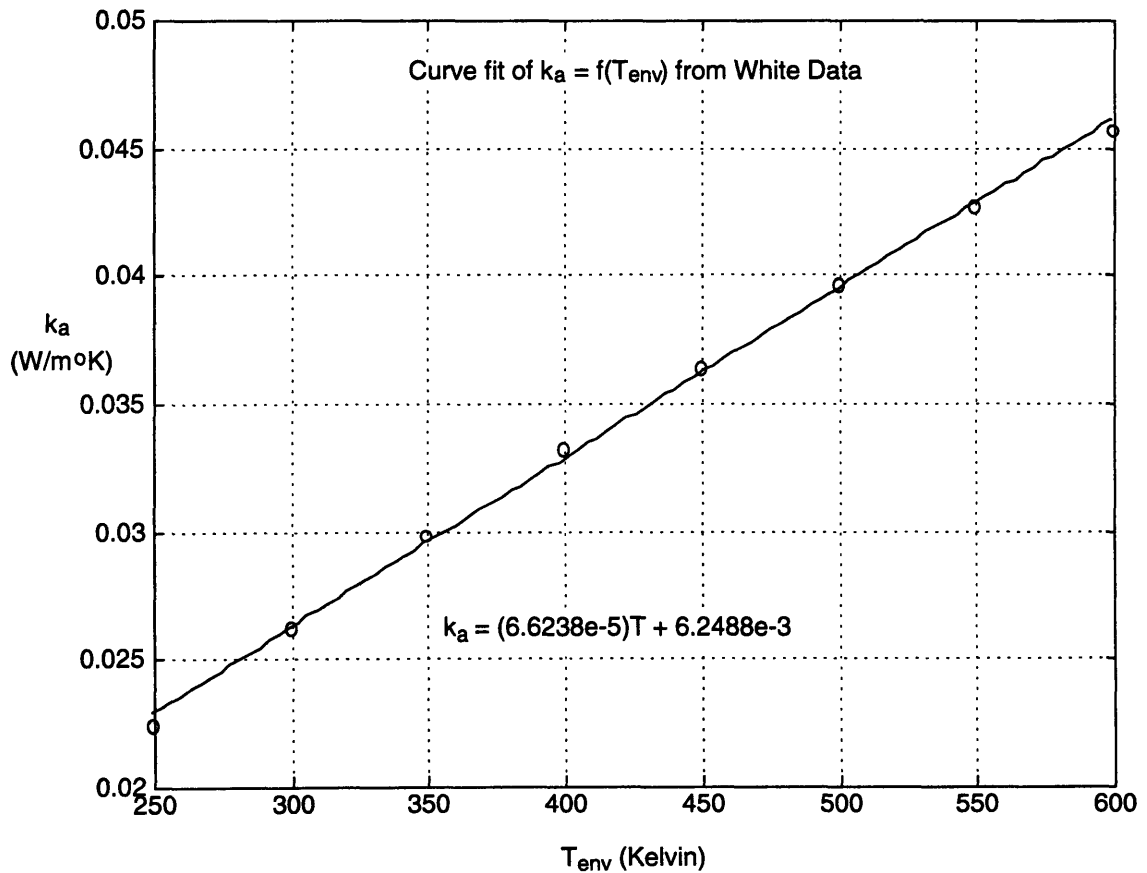


Figure B2. Thermal conductivity-temperature curve for air.

Figure B3 shows a curve fit relating the Prandtl number to  $T_{\text{env}}$  in air.

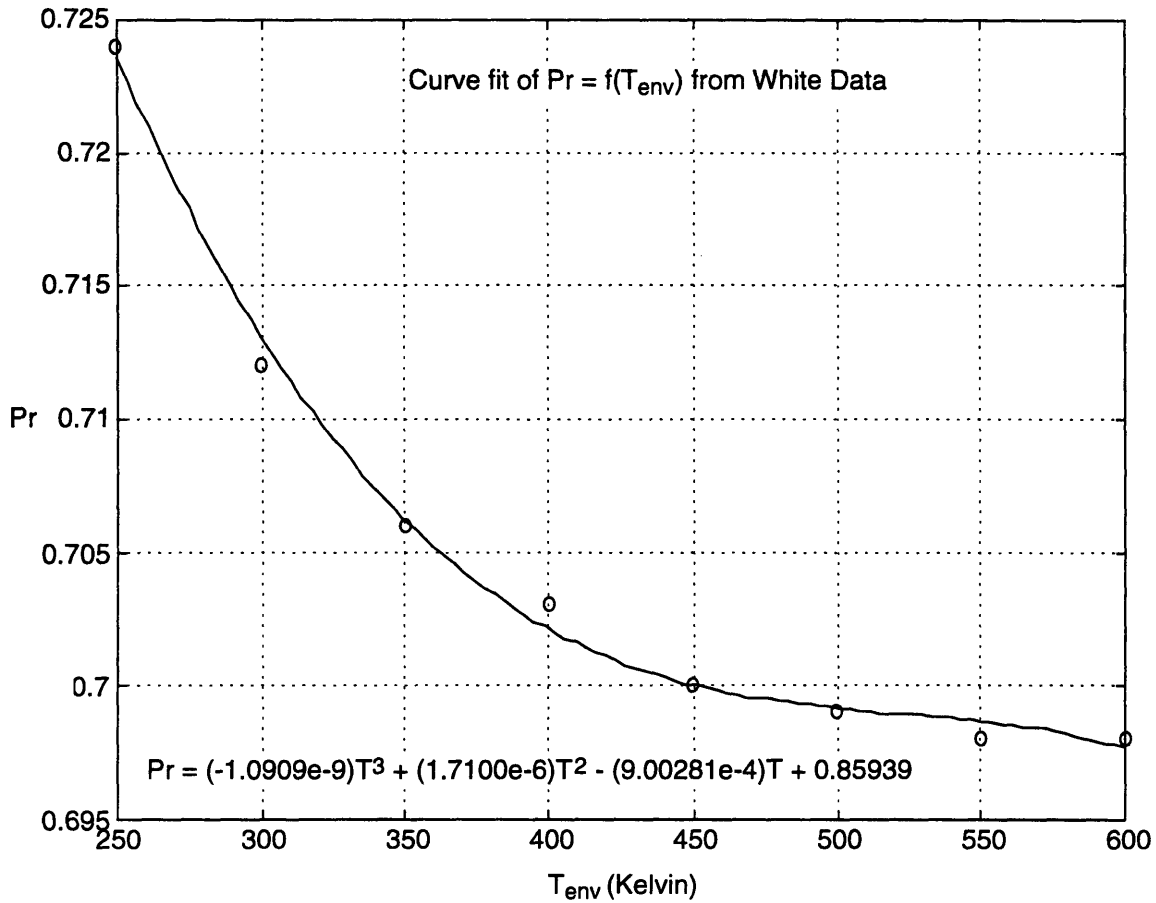


Figure B3. Prandtl-temperature curve for air.

Equation B5 shows how the  $Ra_D$  is calculated as the product of the Grashof and Prandtl numbers.

$$Ra_D = Pr \left( \frac{g\beta}{\nu^2} \right) (T_w - T_{env}) D^3 \quad (B5)$$

The grouping of  $g$  (gravity),  $\beta$  (coefficient of thermal expansion) and  $\nu$  (kinematic viscosity) has been plotted on semi-log plots for various gases. Figure B4 plots the log of  $(g\beta/\nu^2)$  versus temperature for air.

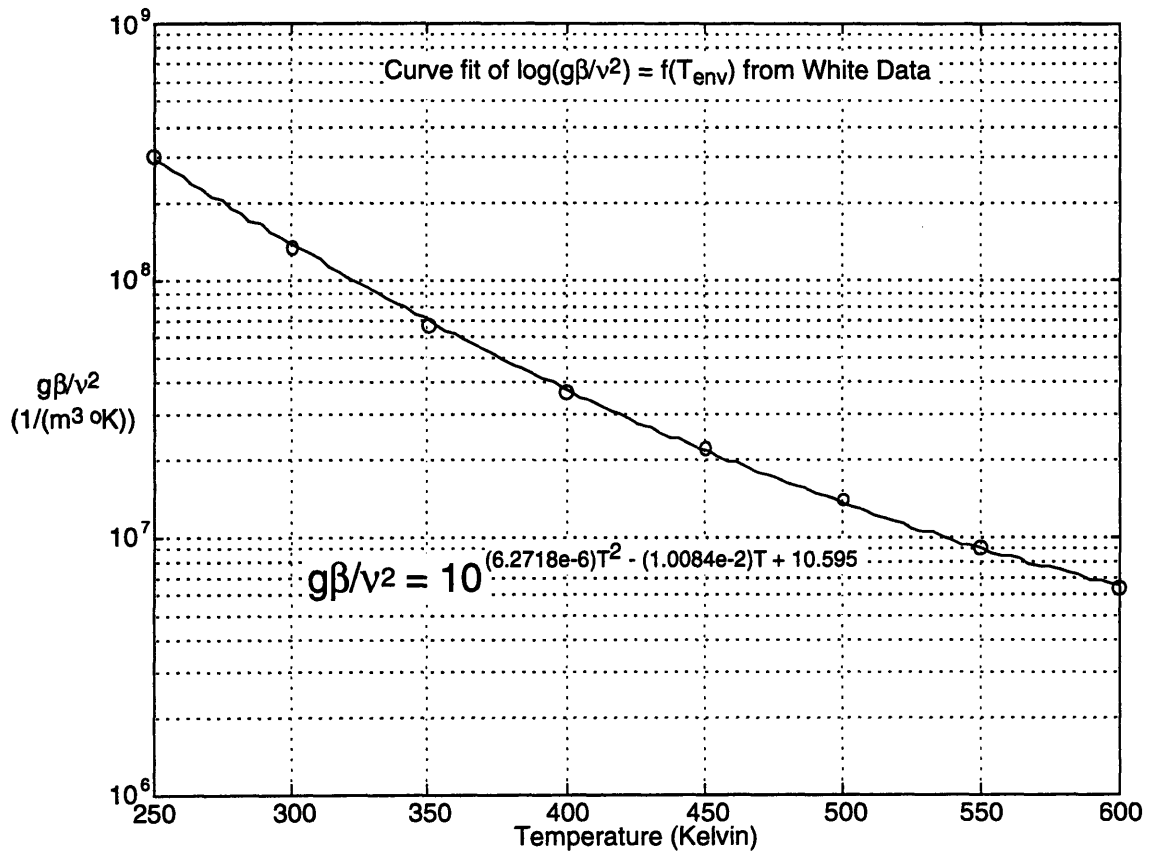


Figure B4. Curve relating  $\log_{10}(g\beta/v^2)$  to temperature for air.

In a similar manner the heat-transfer coefficient can be calculated for a SMA wire with a rectangular cross-section.

$$Nu_L = \frac{h_{env}L}{k_a} = \left( .825 + \frac{.387Ra_L^{\frac{1}{6}}}{\left[ 1 + \left( \frac{.492}{Pr} \right)^{\frac{9}{16}} \right]^{\frac{8}{27}}} \right)^2 \quad (B6)$$

When calculating the Rayleigh number for Equation B6, replace D with L in equation B5. Note that L will be chosen as the larger of the two dimensions associated with the rectangular cross-section of the SMA wire. Equation B6 is valid for  $0.1 \leq Ra_L \leq 10^{12}$

Radiation losses can also be modeled into the heating and cooling dynamics of the SMA. Equation B1 can be modified to yield the following formula:

$$mC_p \left( \frac{dT_w}{dt} \right) = \frac{V_w^2(t)}{R_w} - h_{env} A_w (T_w - T_{env}) - \sigma_s A_w (T_w^4 - T_{env}^4) \quad (B7)$$

The variable  $\sigma_s$  is the Stefan-Boltzmann constant, and the wire and environmental temperatures are in Kelvin. Radiation losses were modeled into the computer simulation program, but had little effect in the cooling dynamics for normal operating temperatures.

## B.2 Temperature Strain curve model of a Shape Memory Alloy wire.

A generalized temperature strain curve is shown in Figure B5. The temperature-strain curve has five distinct slopes. It also shows how the minor hysteresis curves will be modeled to behave.

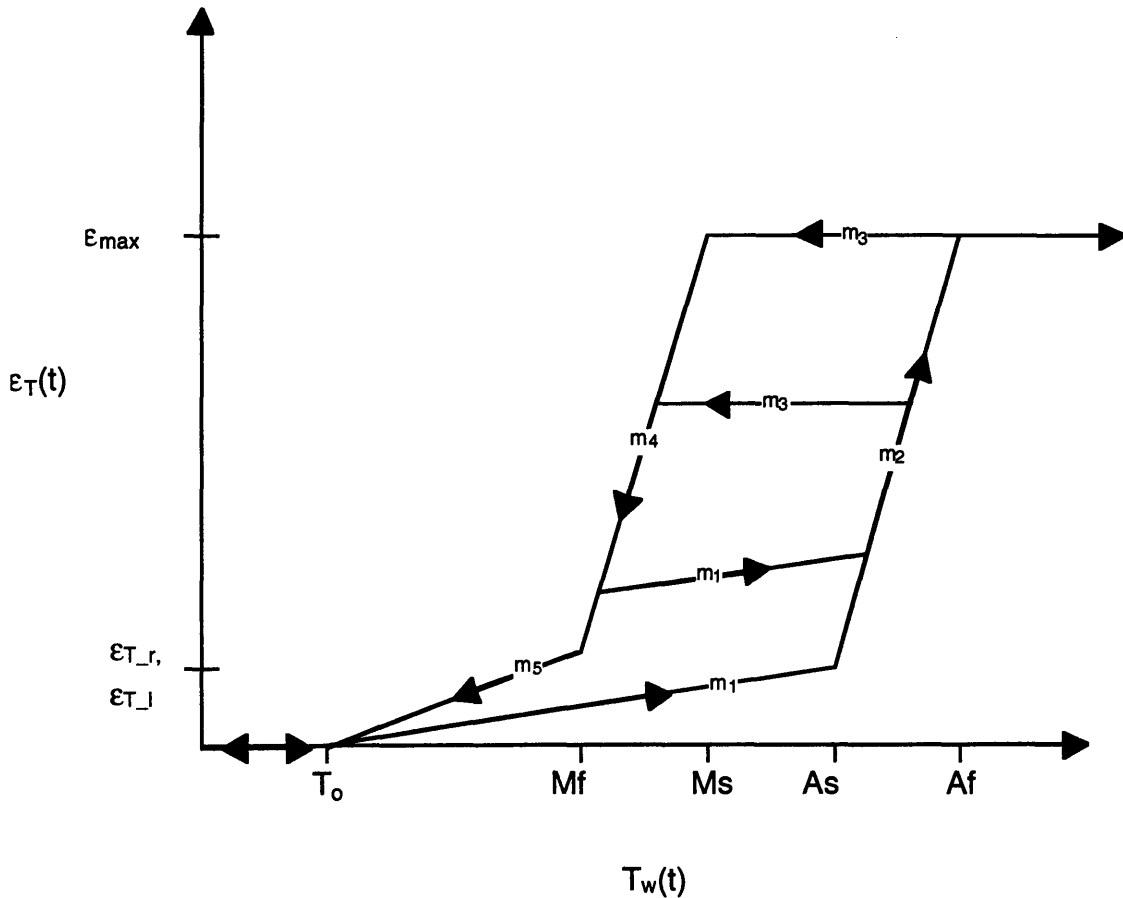


Figure B5. Temperature-strain curve model for a SMA.

Figure B5 displays the zero temperature ( $T_0$ ), the Martensite start temperature ( $M_s$ ), the Martensite finish temperature ( $M_f$ ), the Austenite start temperature ( $A_s$ ), the Austenite finish temperature ( $A_f$ ), the maximum temperature strain ( $\epsilon_{max}$ ), the right temperature strain ( $\epsilon_{T,r}$ ), and the left temperature strain ( $\epsilon_{T,l}$ ) variables. These variables describe the five slopes as follows:

$$\begin{aligned}
m_1 &= \frac{\epsilon_{T,r}}{A_s - T_o} \\
m_2 &= \frac{\epsilon_{\max} - \epsilon_{T,r}}{A_f - A_s} \\
m_3 &= 0 \\
m_4 &= \frac{\epsilon_{\max} - \epsilon_{T,l}}{M_s - M_f} \\
m_5 &= \frac{\epsilon_{T,l}}{M_f - T_o}
\end{aligned} \tag{B8}$$

With these slopes known, the temperature strain of the wire can be determined from a given wire temperature and its previous temperature and position condition. Difficulty appears, because the  $M_s$ ,  $M_f$ ,  $A_s$ ,  $A_f$  and  $\epsilon_{\max}$  vary with the applied stress and cycle history; and, if the bias stress in the SMA is too low, the SMA will not recover to its original length. These dependencies have been observed by Liang (1990), Thoma (1992) and recent experimental results. The following Figures, B6 - B13, are experimental temperature-strain curves of  $\text{Ni}_{49}\text{Ti}_{51}$  and  $\text{Ni}_{49}\text{Ti}_{44}\text{Cu}_7$ , which possess the characteristics shown in Figure B5.

Figures B6-B9 are temperature-strain curves for  $\text{Ni}_{49}\text{Ti}_{51}$  under stresses of 4.3, 47.3, 86.0 and 150.4 MPa, respectively.

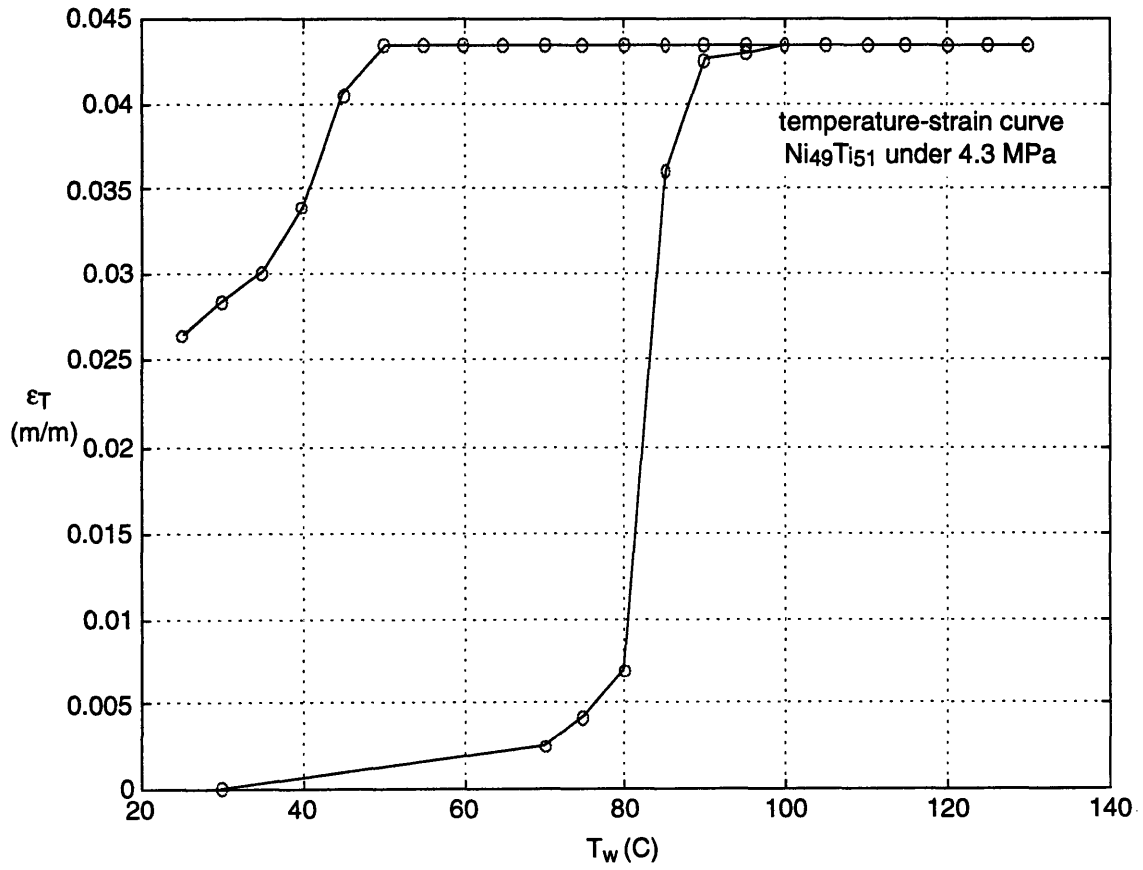


Figure B6. Experimental temperature-strain curve of a 4.3 MPa biased Ni<sub>49</sub>Ti<sub>51</sub> wire.

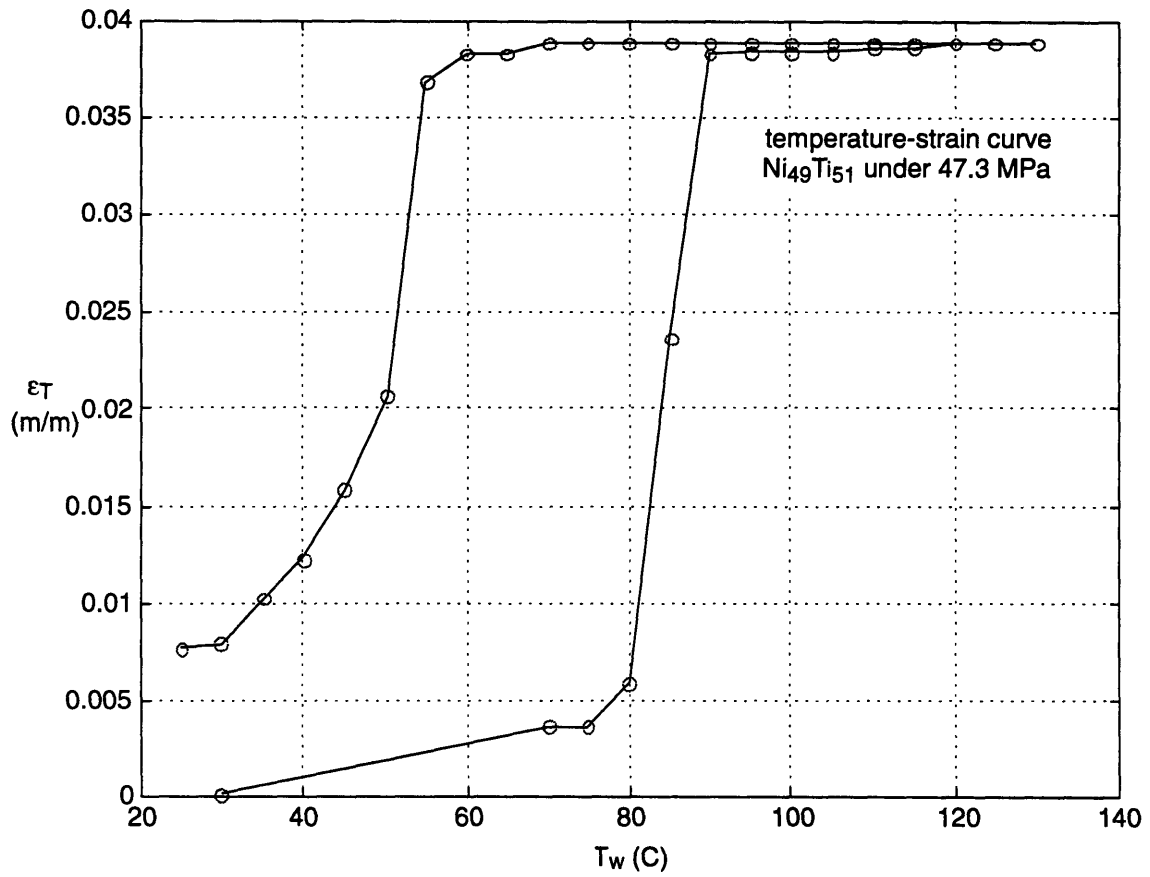


Figure B7. Experimental temperature-strain curve of a 47.3 MPa biased Ni<sub>49</sub>Ti<sub>51</sub> wire.

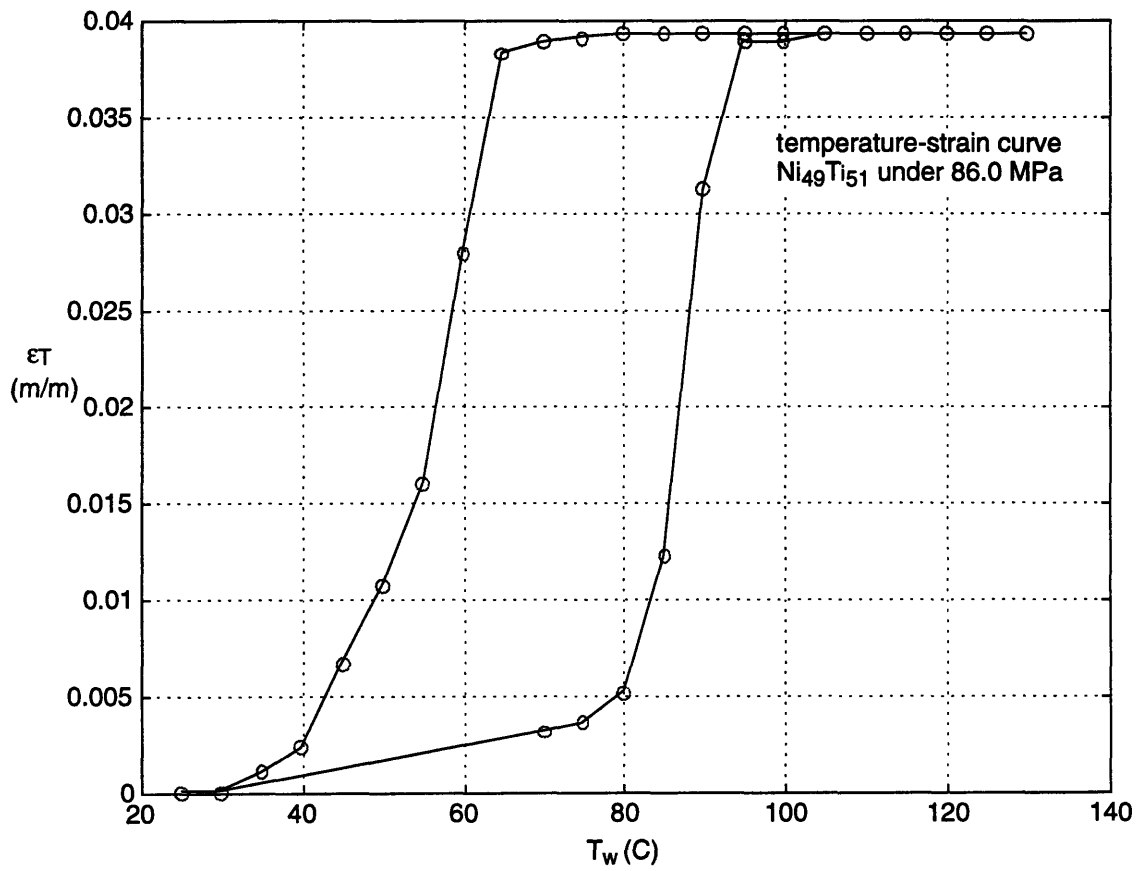


Figure B8. Experimental temperature-strain curve of a 86.0 MPa biased Ni<sub>49</sub>Ti<sub>51</sub> wire.

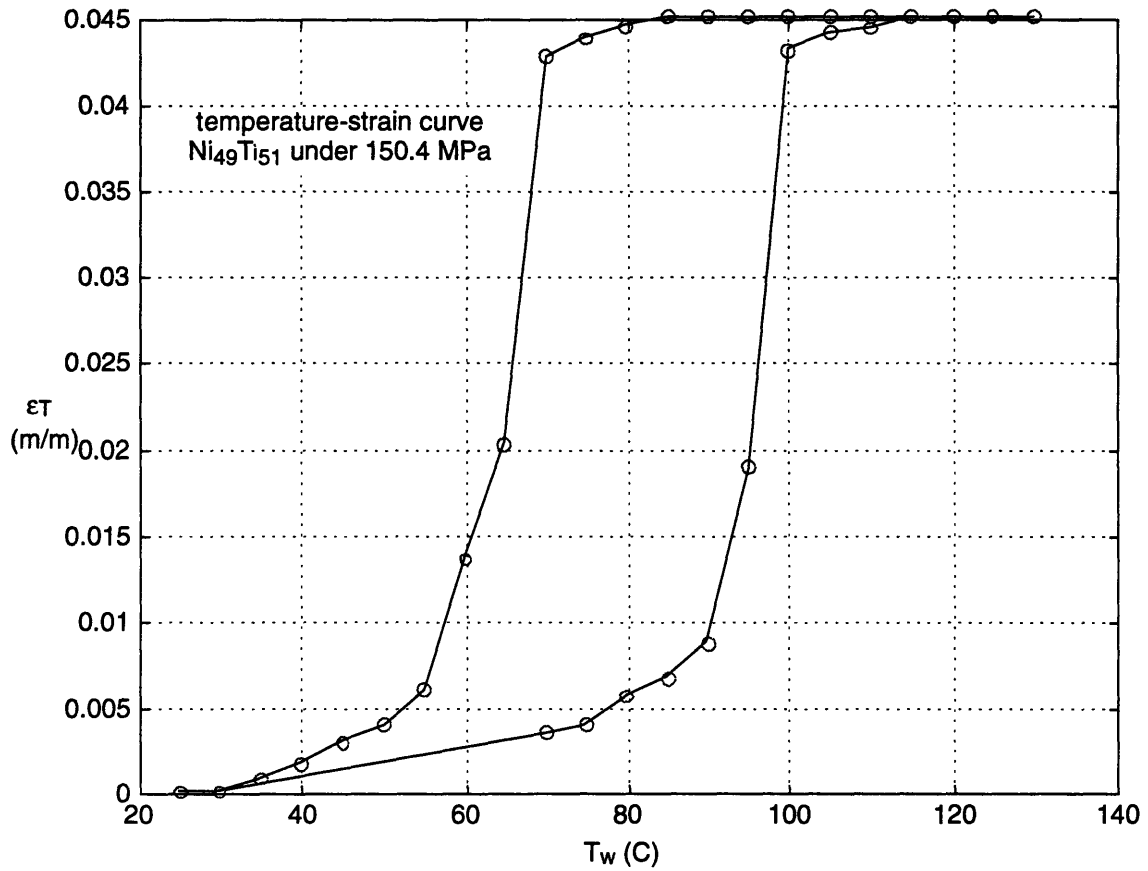


Figure B9. Experimental temperature-strain curve of a 150.4 MPa biased Ni<sub>49</sub>Ti<sub>51</sub> wire.

Figures B6 - B9 illustrate the unrecovered strain due to a small bias stress, the increasing transformation temperatures due to increased stress, and the minor transformation slopes. Figures B10 - B13 reinforce the need to be aware of these minor slopes, since they affect the overall hysteresis loop.

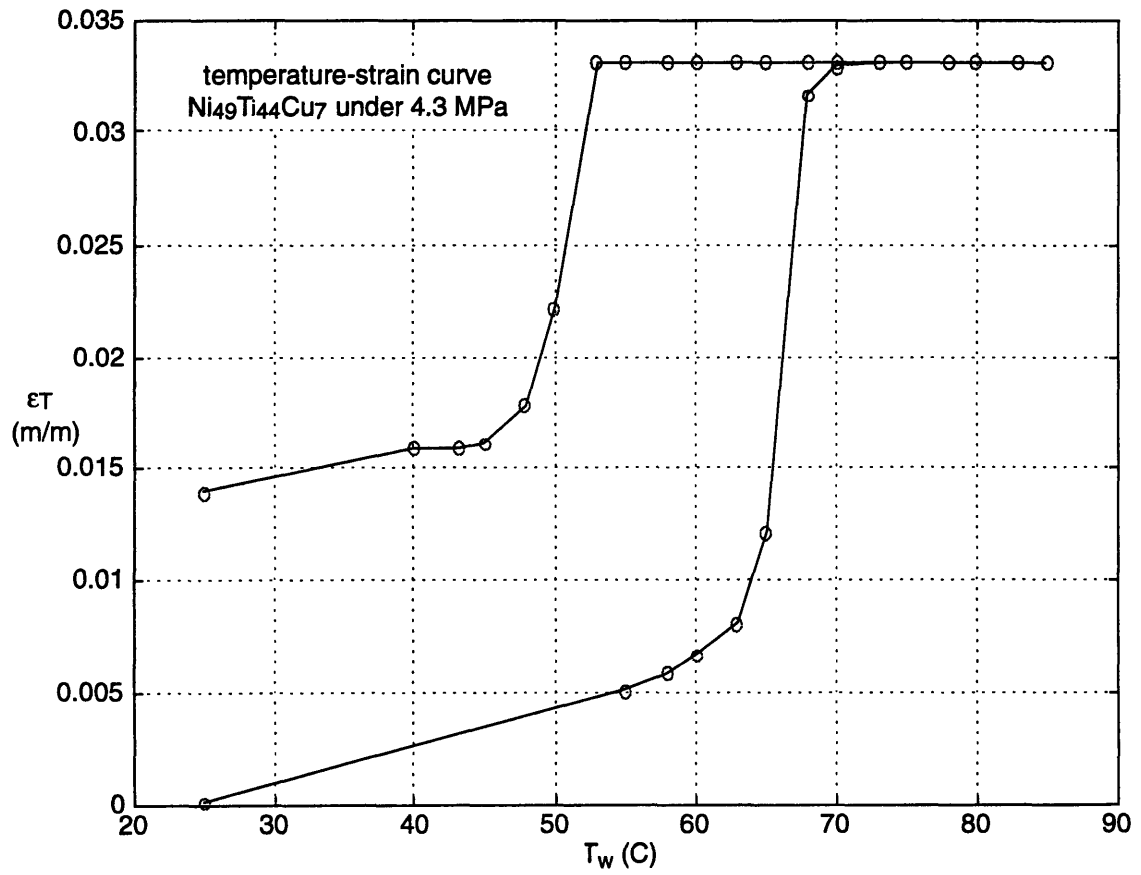


Figure B10. Experimental temperature-strain curve of a 4.3 MPa biased Ni<sub>49</sub>Ti<sub>44</sub>Cu<sub>7</sub> wire.

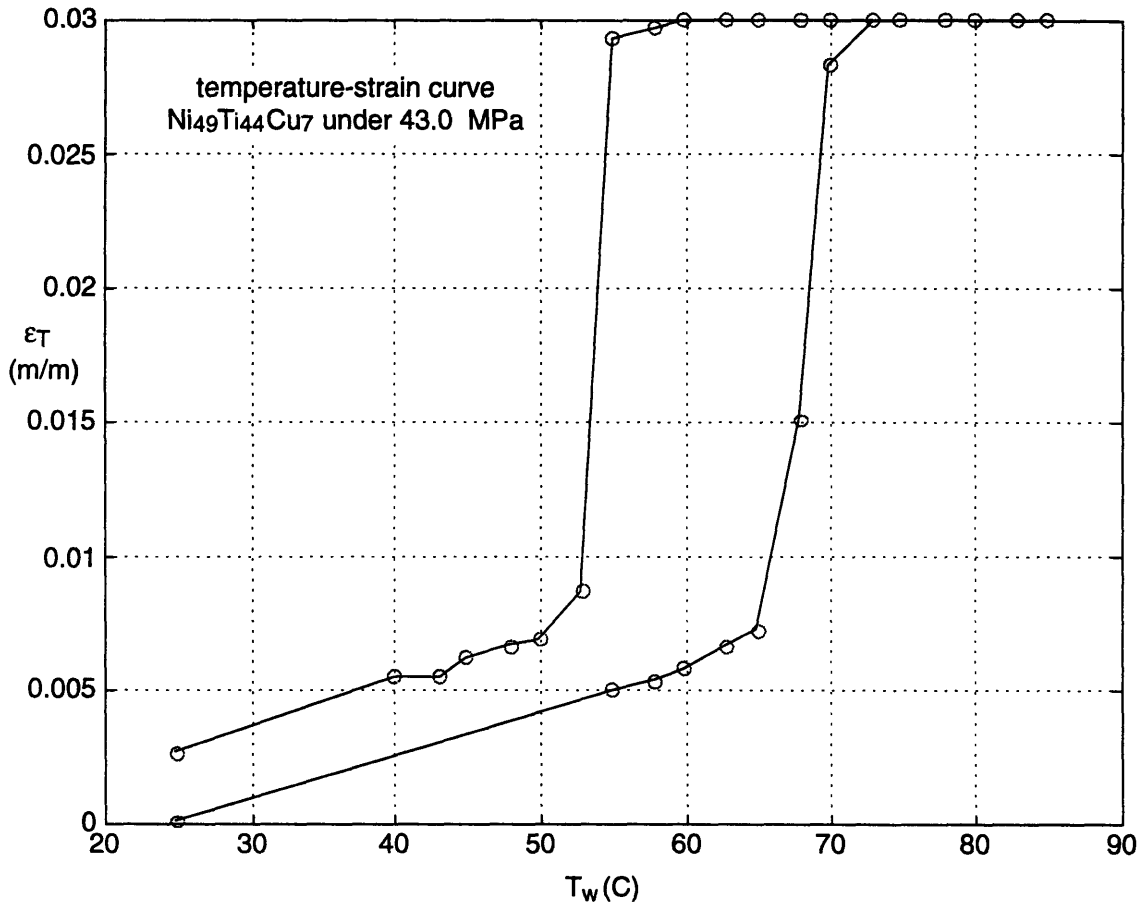


Figure B11. Experimental temperature-strain curve of a 43.0 MPa biased Ni<sub>49</sub>Ti<sub>44</sub>Cu<sub>7</sub> wire

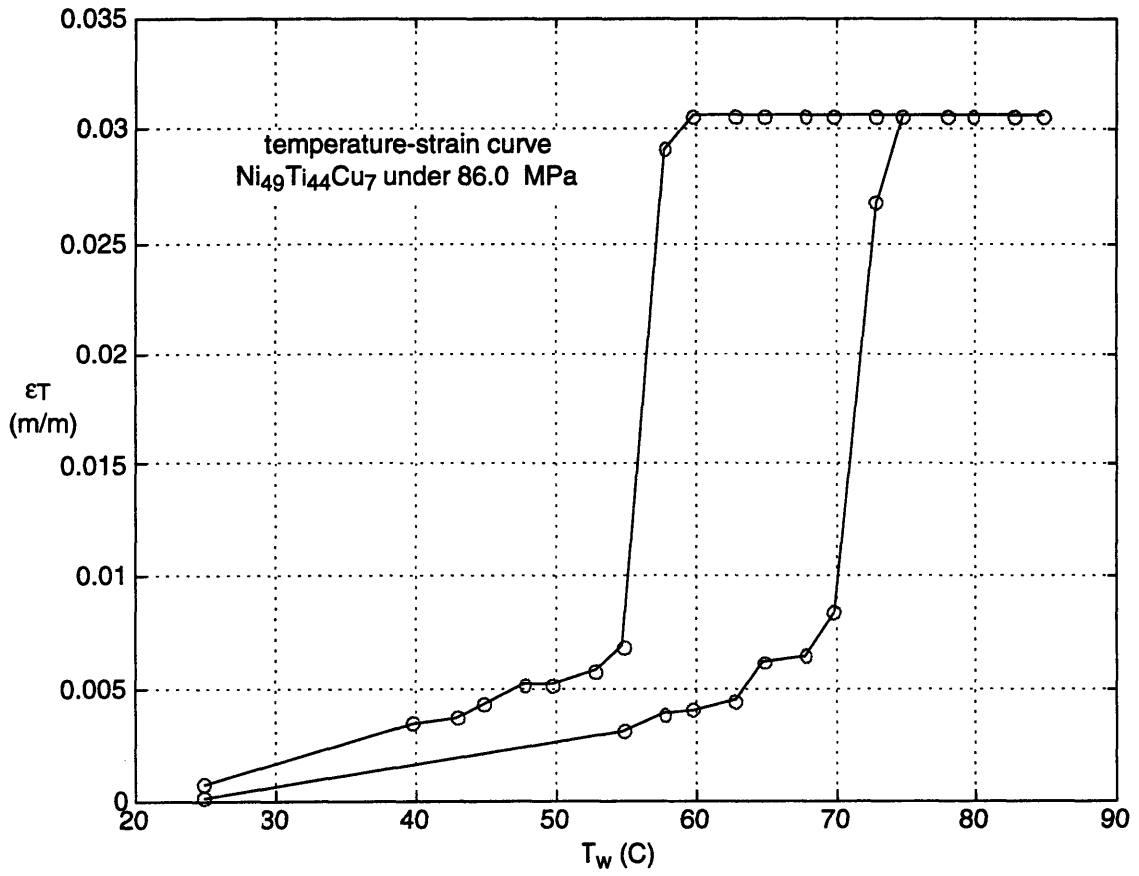


Figure B12. Experimental temperature-strain curve of a 86.0 MPa biased  $\text{Ni}_{49}\text{Ti}_{44}\text{Cu}_7$  wire.

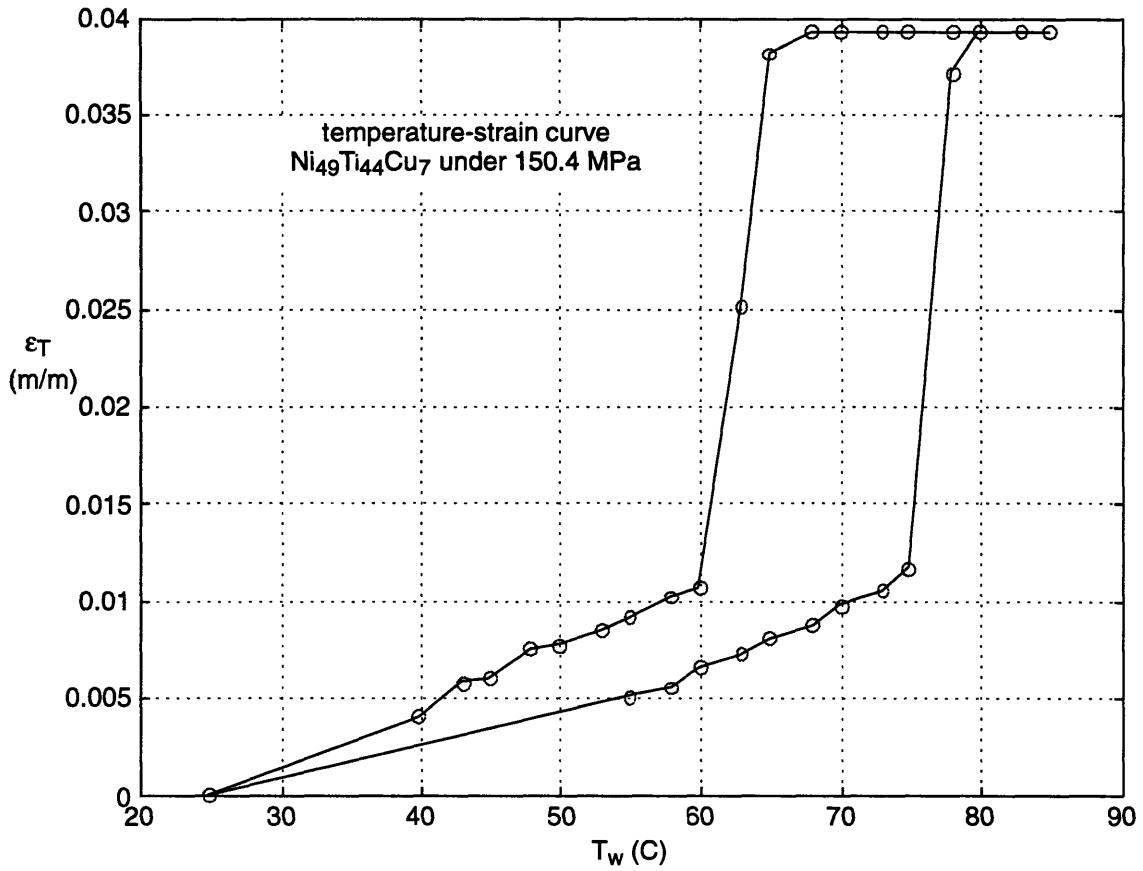


Figure B13. Experimental temperature-strain curve of a 150.4 MPa biased Ni<sub>49</sub>Ti<sub>44</sub>Cu<sub>7</sub> wire

It is important to realize that if design engineers do not address these lagging strain recovery aspects of a SMA wire, the engineers may incorrectly rate a device to work at temperatures up to the Martensite finish temperature.

Figure B14 shows how the Ms, Mf, As and Af vary with the applied stress for a Ni<sub>49</sub>Ti<sub>51</sub> wire. These curves were based on the results presented in Figures B6-B9.

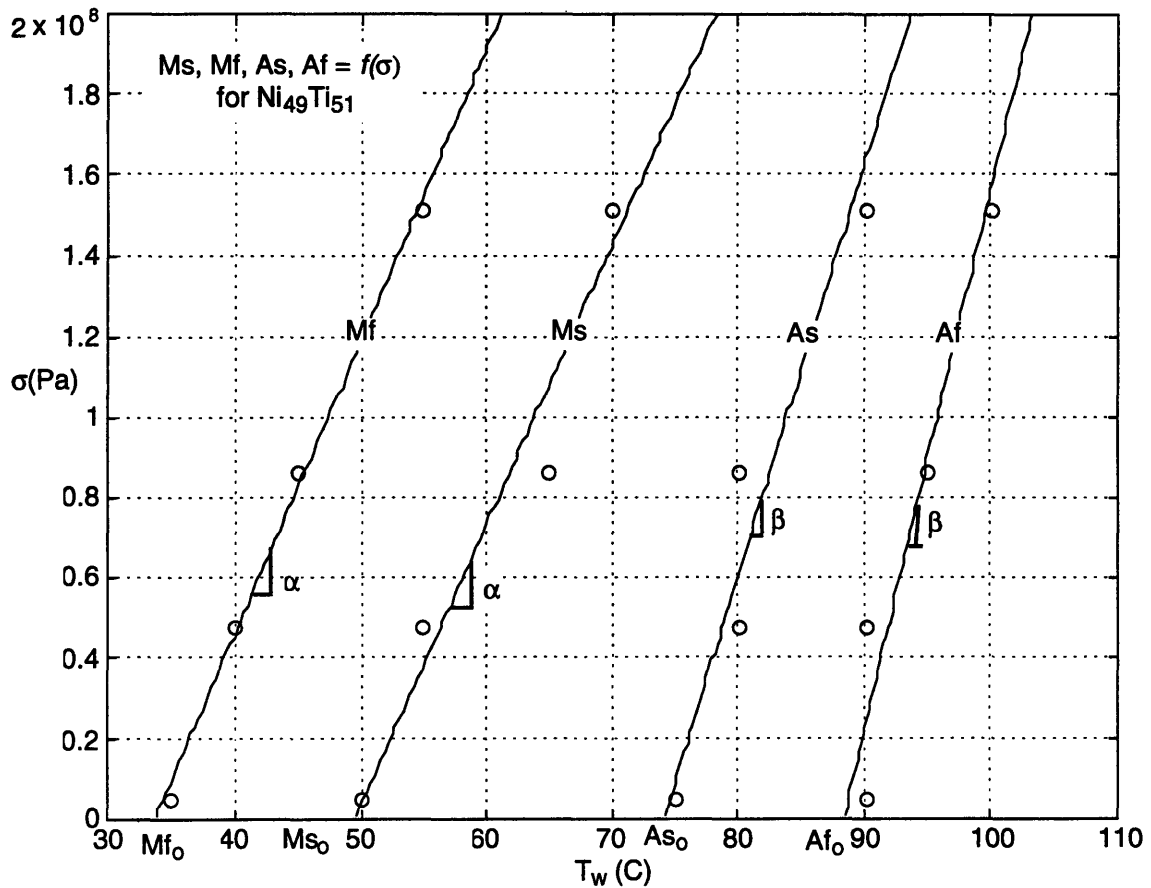


Figure B14. Transformation temperature-stress curves  
(Ms, Mf, As, Af) for Ni<sub>49</sub>Ti<sub>51</sub> wire.

Figure B14 allows the following formulas, describing the transformation temperatures' dependencies on stress:

$$\begin{aligned}
 M_s &= M_{s_0} + \alpha\sigma \\
 M_f &= M_{f_0} + \alpha\sigma \\
 A_s &= A_{s_0} + \beta\sigma \\
 A_f &= A_{f_0} + \beta\sigma
 \end{aligned}
 \quad (B9)$$

Equation B9 would be adequate to explain the transformation temperatures associated with the SMA, except that the constants  $M_{s_0}$ ,  $M_{f_0}$ ,  $A_{s_0}$  and  $A_{f_0}$  vary with cycling and manufacturing methods. This characteristic is addressed by Thoma (1992) for Ni<sub>49</sub>Ti<sub>51</sub> wires, which were given different heat treatments of 400°C, 425°C and 600°C. Figures

B15 and B16 show how the  $\text{Ni}_{49}\text{Ti}_{51}$  wire's Af and Ms temperatures vary under stresses of 69 MPa and 207 MPa due to cycling.

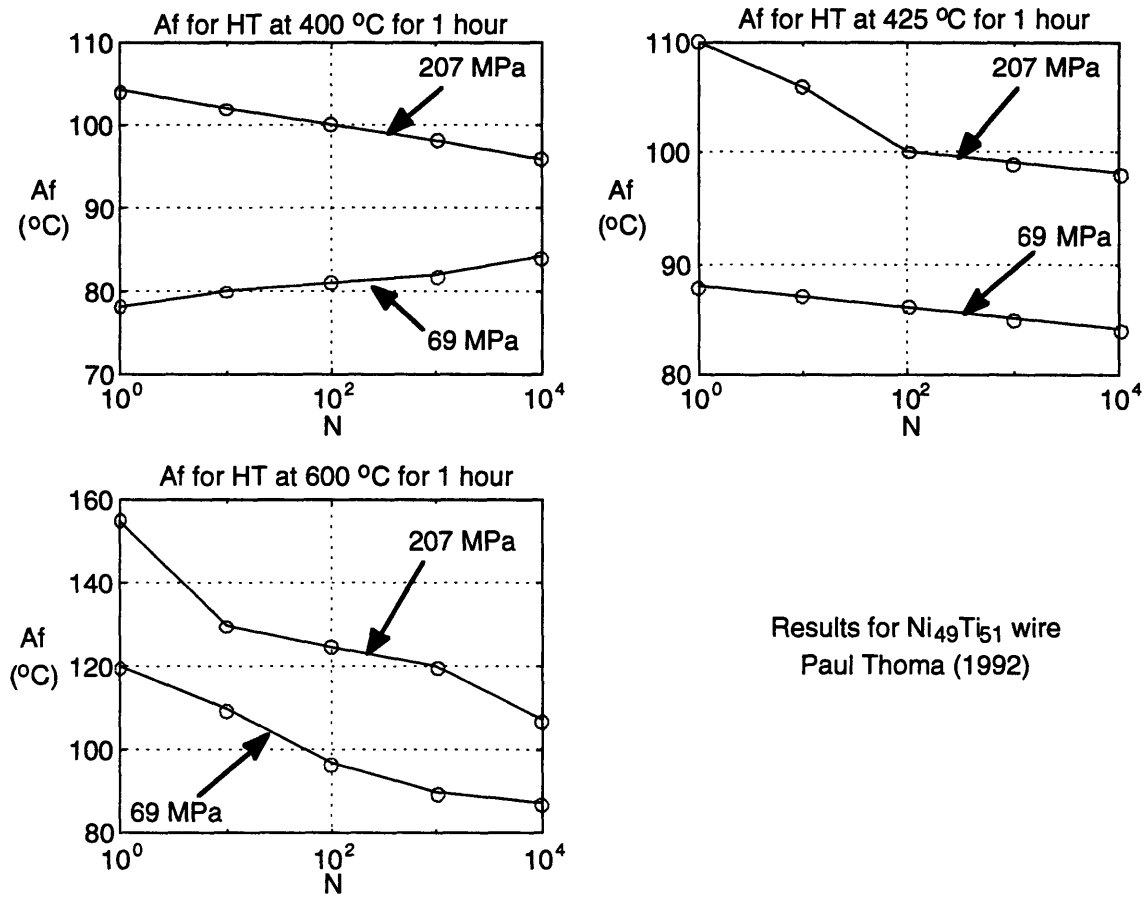


Figure B15. Austenite finish temperature-cycle curves for  $\text{Ni}_{49}\text{Ti}_{51}$  wires with different heat-treatments.

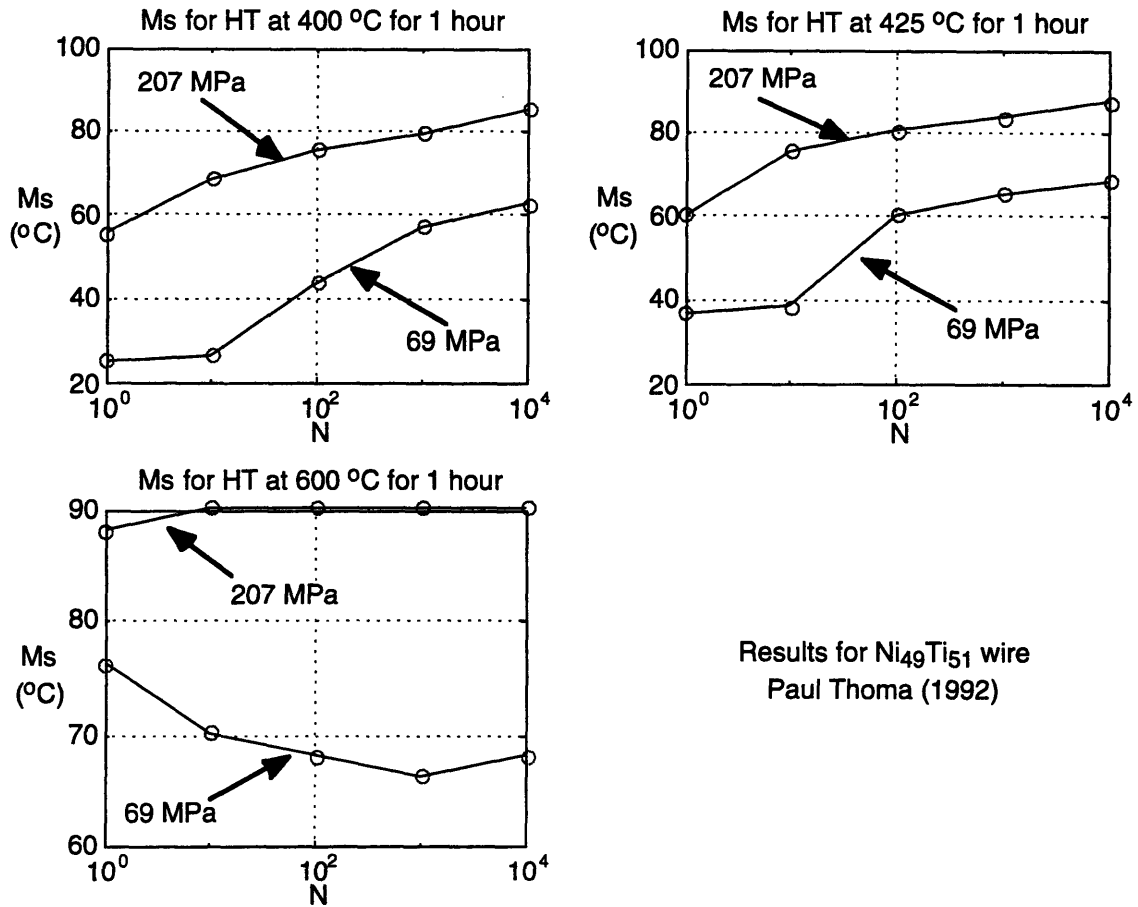


Figure B16. Martensite start temperature-cycle curves for  $Ni_{49}Ti_{51}$  wires with different heat-treatments.

Figures B15 and B16 show how  $A_f$  and  $M_s$  temperatures change due to cycling and heat treatment. Figure B15 shows that  $A_f$  tends to get smaller when cycled. Figure B16 shows that  $M_s$  tends to get larger when cycled. These Figures imply that the hysteresis curve of the SMA gets narrower when cycled. Note how all  $A_f$  and  $M_s$  temperatures, under the same stress but different heat-treatments, tend to reach the same point as the cycles increase. In Figures B15 and B16 the  $M_s$  curves having the same heat treatment but different bias stress tend to remain parallel. This implies that the slopes  $\alpha$  and  $\beta$  are relatively constant; however, the zero-stress transformation temperatures shift when cycled. Equation B9 can still be used; however,  $M_{s_0}$ ,  $M_{f_0}$ ,  $A_{s_0}$ ,  $A_{f_0}$  need to be modified to address the changing hysteresis loop.

$$\begin{aligned}
Ms_o &= Ms_{oo} + \Delta_M(HT, N) \\
Mf_o &= Mf_{oo} + \Delta_M(HT, N) \\
As_o &= As_{oo} - \Delta_A(HT, N) \\
Af_o &= Af_{oo} - \Delta_A(HT, N)
\end{aligned}
\tag{B10}$$

Variables such as  $Ms_{oo}$ , represent the transformation temperature at which the wire is under zero stress and has not yet been through a transformation cycle. The functions  $\Delta_M(HT, N)$  and  $\Delta_A(HT, N)$  are curves approximating the net transformation temperature change with respect to cycles for a given heat treatment.

Figures B6, B7, B10, B11 and B12 indicated that the SMA was unable to fully recover its shrunk length due to the low bias stress. This phenomenon will be modeled in by defining the unrecovered strain variable  $\epsilon_u$ . From Figures B6 and B7 a curve relating  $\epsilon_u$  to  $\sigma$  is created and shown in Figure B17.

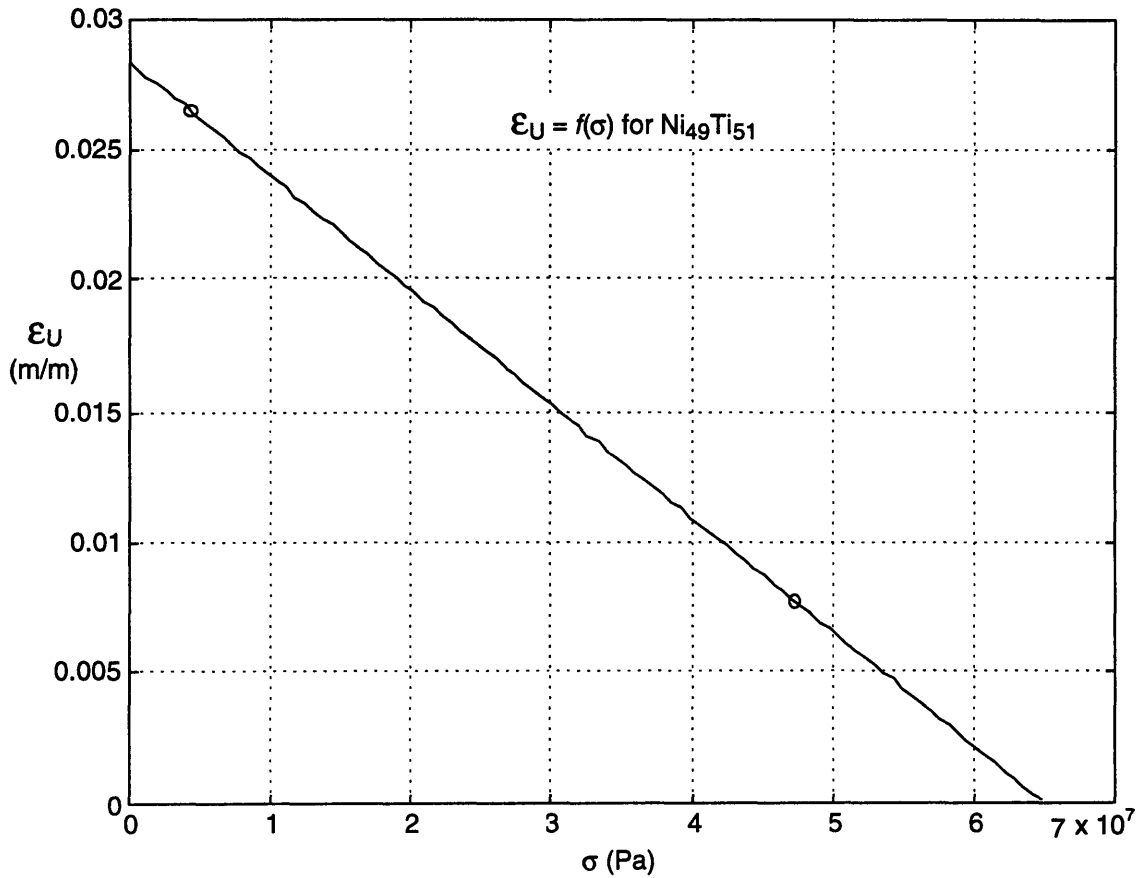


Figure B17. Unrecovered strain-stress curve for Ni<sub>49</sub>Ti<sub>51</sub> wire.

The unrecovered strain affects the temperature strain in the following manner:

First the unrecovered strain is determined for a given stress, using Equation B11. Equation B11 is a linear equation with zero unrecovered strain ( $\epsilon_{U_0}$ ) and slope ( $m$ ) known.

$$\epsilon_U = \epsilon_{U_0} - m\sigma \quad (\text{B11})$$

The desired temperature strain  $\epsilon_{Td}$  is determined, and the following comparison is implemented by using Equation B12.

$$\varepsilon_T(t) = \begin{cases} \varepsilon_{Td}(t) & \text{if } \varepsilon_{Td}(t) \geq \varepsilon_T(t-1) \text{ or } \varepsilon_{Td}(t) \geq \varepsilon_U(t) \\ \varepsilon_T(t-1) & \text{if } \varepsilon_{Td}(t) < \varepsilon_T(t-1) \text{ and } \varepsilon_T(t-1) \leq \varepsilon_U(t) \\ \varepsilon_U(t) & \text{if } \varepsilon_{Td}(t) < \varepsilon_T(t-1) \text{ and } \varepsilon_T(t-1) > \varepsilon_U(t) \text{ and } \varepsilon_{Td}(t) < \varepsilon_U(t) \end{cases} \quad (\text{B12})$$

The terms having (t-1) are interpreted as “states” with their most recent values. In the discrete domain they would be the most recently sampled value during a time step T. The loss of SMA ability to shrink due to cycling shall be modeled.

Thoma (1992), noted that Shape Memory Alloys when cycled, loose the ability to shrink. Figure B18 shows a curve relating the SMA’s shrink loss (SL) to cycles (N) for a Ni<sub>49</sub>Ti<sub>51</sub> wire.

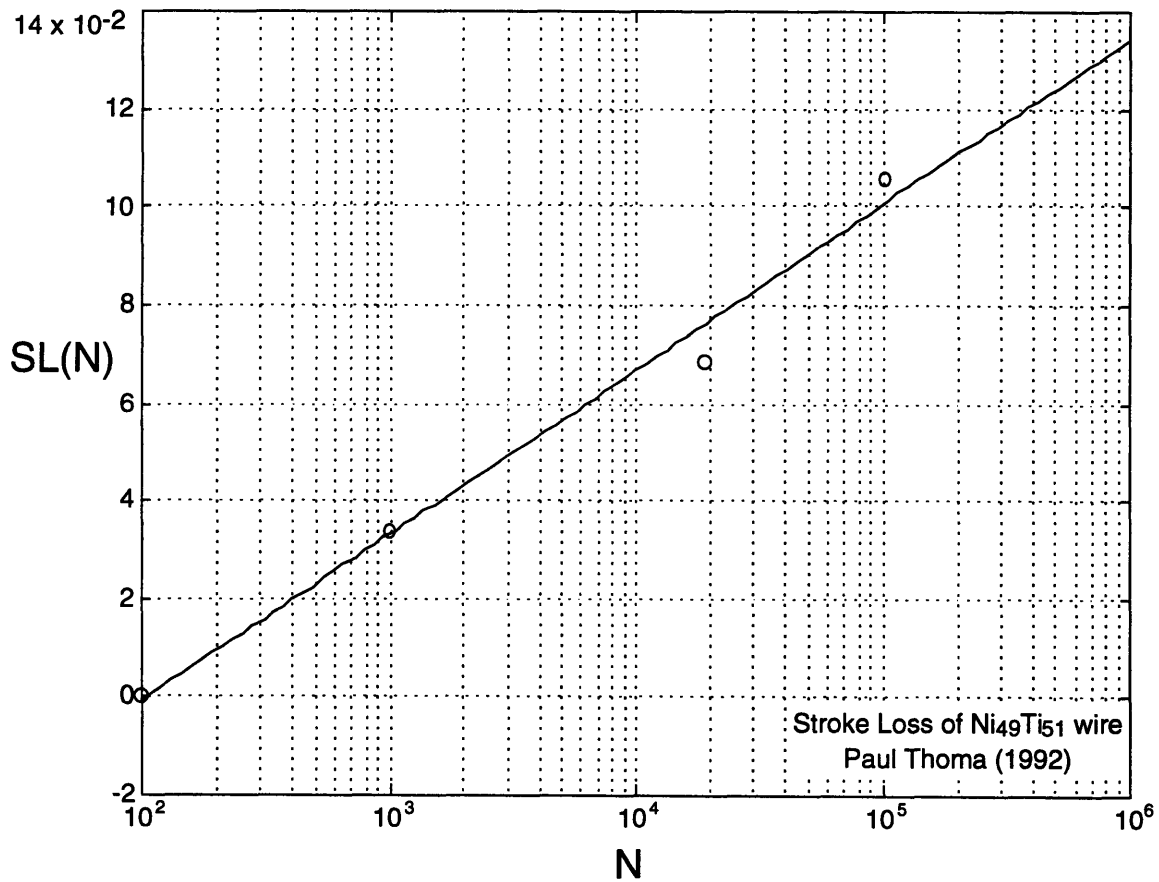


Figure B18. Shrink loss-cycle curve for Ni<sub>49</sub>Ti<sub>51</sub> wire.

With the shrink loss known, the  $\varepsilon_{\max}$  can be determined as follows:

$$\epsilon_{\max} = (1 - \text{SL}(N))\epsilon_{\max i} \quad (\text{B13})$$

Note that shrink loss is represented as being a function of the actuation cycle. With the model of the temperature-strain curve complete, the remaining effects due to creep and changing wire stiffness will be addressed.

### ***B.3 Modeling creep and changing stiffness of a SMA.***

As a Shape Memory Alloy wire is cycled under an applied stress, it elongates; this effect is termed creep. Thoma (1992) addresses the effects of creep on a SMA. He obtained experimental results relating the wire creep to an applied stress of 69.0 and 207.0 MPa. The SMAs he tested were Ni<sub>49</sub>Ti<sub>51</sub> wires heat-treated at 400°C, 425°C and 600°C for one hour after the annealed wires were cold-worked 40% (their cross sectional area was reduced 40%). Figures B19 and B20 show the resulting wire creep  $\epsilon_c$ , under stresses of 69.0 and 207.0 MPa, respectively.

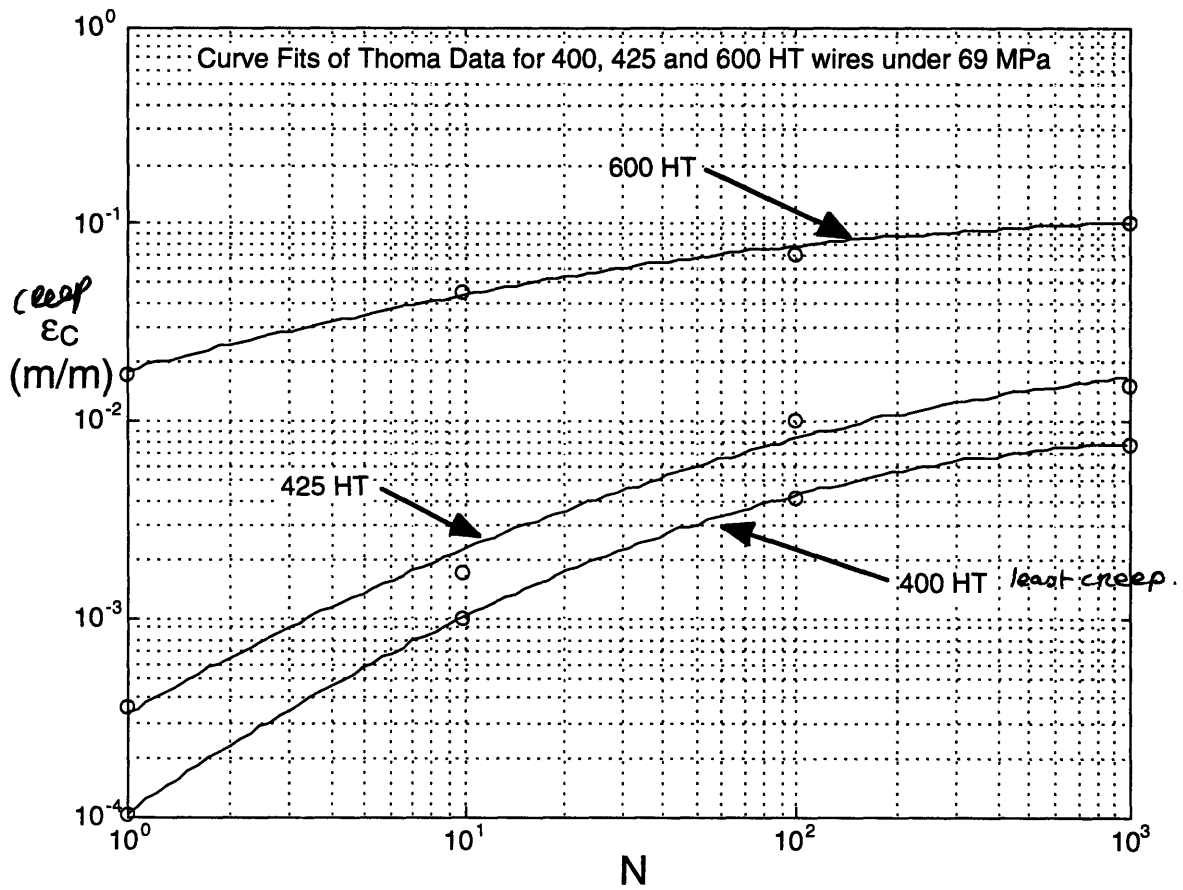


Figure B19. Creep-cycle curves of  $\text{Ni}_{49}\text{Ti}_{51}$  wires (400°C, 425°C and 600°C heat-treatments) under 69.0 MPa.

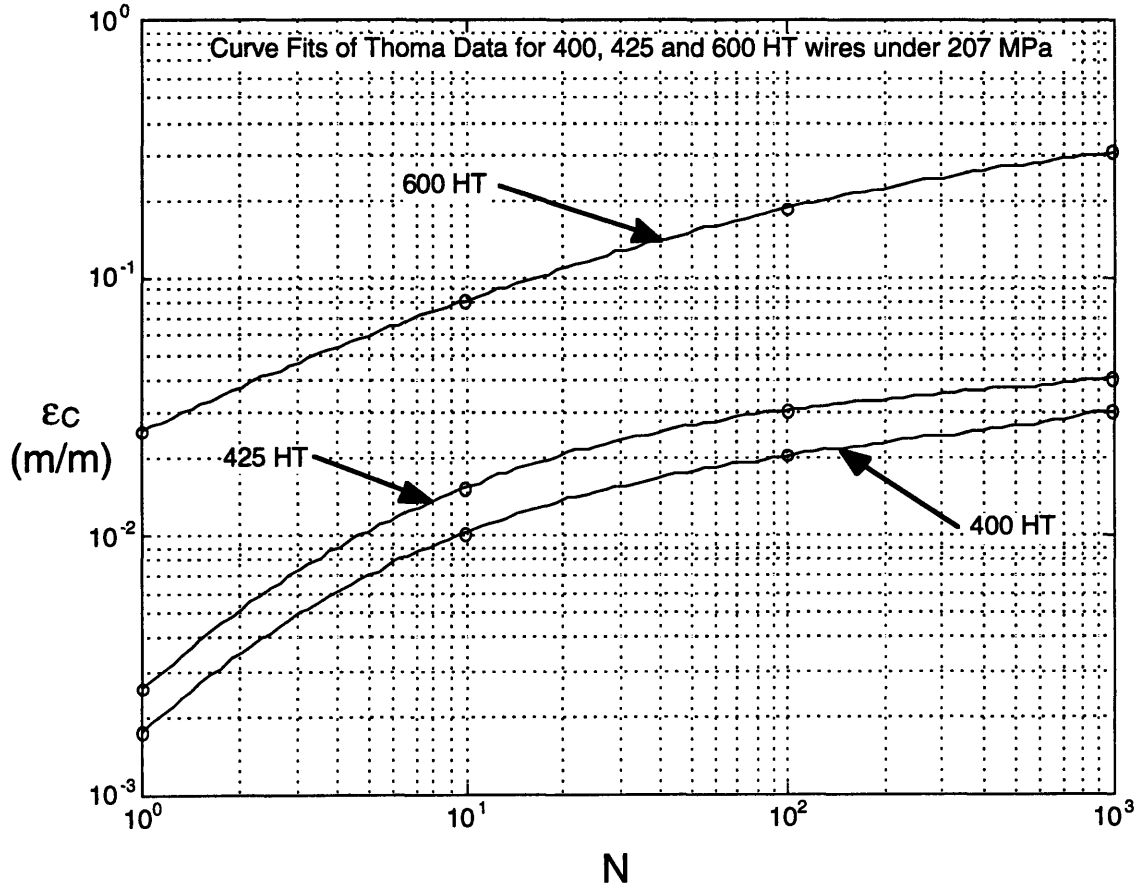


Figure B20. Creep-cycle curves of  $\text{Ni}_{49}\text{Ti}_{51}$  wires (400°C, 425°C and 600°C heat-treatments) under 207.0 MPa.

Thoma noted that a manufacturer could cycle a  $\text{Ni}_{49}\text{Ti}_{51}$  wire with a 400°C heat-treat 200 times under 207.0 MPa in order to pre-creep the wire. He then noted that the wire would contract when cycled under 69.0 MPa stress. Figure B21 illustrates this observation.

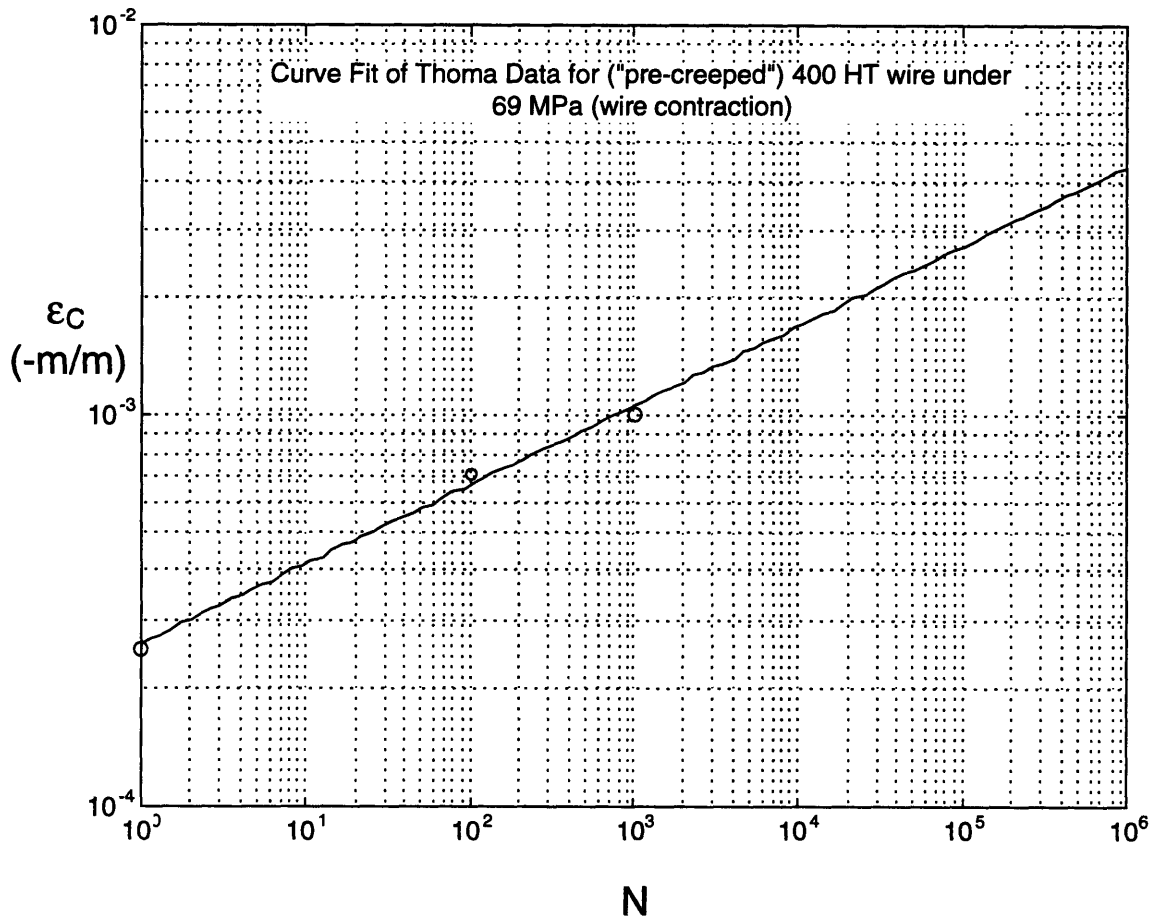


Figure B21. Contraction-cycle curve for pre-creeped  $\text{Ni}_{49}\text{Ti}_{51}$  wire under 69.0 MPa.

Figures B19-B21 show how many variables need to be considered when determining creep in the SMA. For example, in  $\text{Ni}_{49}\text{Ti}_{51}$  wires which have not been pre-creeped, the creep approximations would be based on:

1. curves for a given HT in Figure B19 with  $(55.0 \leq \sigma \leq 103.0 \text{ MPa})$ .
2. curves for a given HT in Figure B20 with  $(\sigma \geq 173.0 \text{ MPa})$ .
3. the average of the curves for a given HT in Figures B19 and B20 with  $(103.0 < \sigma < 173.0 \text{ MPa})$ .

If the wire was pre-creeped, then the creep approximations would be based on:

1. Figure B21 with ( $\sigma < 103.0$  MPa), the wire contracts.
2.  $\epsilon_c = 0$  with ( $103.0 < \sigma < 173.0$  MPa), the wire neither elongates nor contracts.
3. curves for a given HT in Figure B20 with ( $\sigma \geq 173.0$  MPa). The creep is calculated by ( $\epsilon_c(200) - \epsilon_c(200+N)$ ), and the wire continues to elongate.

With the completion of the methodology presented for modeling the wire creep, the model of the SMA's changing stiffness is presented.

The stiffness of the SMA ( $K_w$ ) can be calculated by using the wire's cross-sectional area ( $cA_w$ ), length ( $L_w$ ) and Young's Modulus ( $E_w$ ).

$$K_w = \frac{E_w cA_w}{L_w} \quad (\text{B14})$$

$E_w$  is dependent on the net phase of the SMA. As the wire contracts when heated, it undergoes a transformation from the Martensite to the Austenite phase. The percentage of the SMA in the Austenite phase ( $\xi_A$ ) can be estimated by taking the ratio of the temperature strain ( $\epsilon_T$ ) to the maximum temperature strain ( $\epsilon_{Tmax}$ ).

$$\xi_A = \frac{\epsilon_T}{\epsilon_{Tmax}} \quad (\text{B15})$$

The change in the modulus of the wire is proportional to the percentage of Austenite phase. Using Young's Modulus for Martensite and Austenite ( $E_M$  and  $E_A$  respectively), the wire's Young's Modulus can be calculated by incorporating Equation B15.

$$E_w = E_M + (E_A - E_M)\xi_A \quad (\text{B16})$$

Using Equation B14-B16, the changing stiffness of the SMA can be modeled.

## Appendix C: Shape Memory Alloy Experiments and Results

Two experiments involving SMAs are presented in this section. In the first experiment the temperature-strain curve was obtained for three different SMAs. The SMAs are  $\text{Ni}_{49}\text{Ti}_{51}$ ,  $\text{Ni}_{49}\text{Ti}_{44}\text{Cu}_7$  and  $\text{Ni}_{49}\text{Ti}_{44}\text{Hf}_7$  wires with diameters of 75 microns. Sections C.1, C.2 and C.3 explain the experimental apparatus, procedure and results respectively. In the second experiment an attempt to actuate a  $\text{Ni}_{49}\text{Ti}_{51}$  wire one million times under a peak stress of 160 MPa is described. Sections C.4, C.5 and C.6 explain the experimental apparatus, procedure and results, respectively.

**C.1 *Experimental materials and apparatus for obtaining temperature-strain curves***

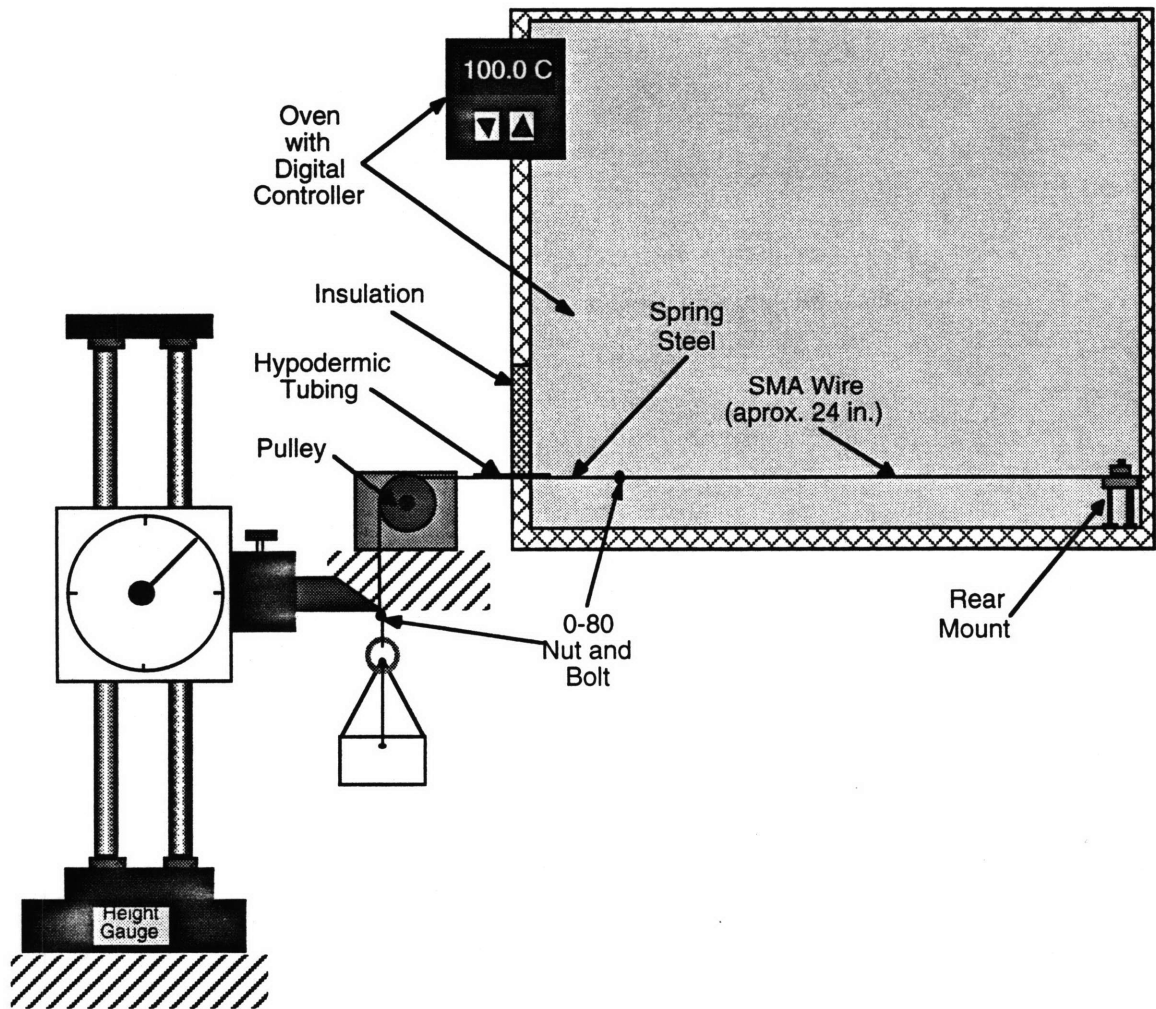


Figure C1. Experimental apparatus used to obtain temperature-strain curves.

Figure C1 shows the experimental apparatus to create the temperature-strain curves for the three SMA wires.

The following materials were used:

1. Spring steel wire
  - Diameter 0.005 inches
2. Ni<sub>49</sub>Ti<sub>51</sub> wire (“Flexinol 90-110”) manufactured by Dynalloy
  - Diameter 0.003 inches
  - Length 24.25 inches
3. Ni<sub>49</sub>Ti<sub>44</sub>Cu<sub>7</sub> wire (“Rk-Special”) manufactured by Dynalloy
  - Diameter 0.003 inches
  - Length 23.75 inches
4. Ni<sub>49</sub>Ti<sub>44</sub>Hf<sub>7</sub> wire (“Flexinol 120-140”) manufactured by Dynalloy
  - Diameter 0.003 inches
  - Length 24.125 inches
5. Calibrated gram mass set
6. Mass holding assembly weighing 2.0 grams

The following tools were used:

1. calibrated digital scale to weigh mass holding assembly
2. calibrated dial height gauge (+/- .0005 inches)
3. oven capable of heating and cooling (30” x 30” x 30” inside dimensions)
4. calibrated digital readout temperature controller for the oven (+/- 1° C)

## ***C.2 Experimental procedure to create temperature-strain curves.***

1. Attach SMA wire to rear mount and spring steel using appropriate fasteners.
2. Measure and record initial length of SMA under 2.0 gram load.
3. Proceed with steps 4-6 with a 2.0, 20.0, 40.0 and 70.0 gram load.
4. With the oven at 25°C, zero the dial gauge at the 0-80 nut which connects the mass holding assembly to the spring steel wire.
5. Increment the oven temperature to the temperatures indicated on the data tables.
6. When the desired temperature is reached, wait one minute before recording the position of the 0-80 nut.
7. Continue with steps 5 and 6 until all data is obtained.
8. Repeat steps 2-7 until all three SMA wires have been tested.

**C.3 Experimental results used to create temperature strain curves.**

<b>Load</b>	<b>2 grams</b>	<b>22 grams *</b>	<b>40 grams</b>	<b>70 grams</b>
<b>Temperature of Oven (Centigrade)</b>	<b>Change in Length (inches)</b>	<b>Change in Length (inches)</b>	<b>Change in Length (inches)</b>	<b>Change in Length (inches)</b>
70	0.060	0.085	0.075	0.085
75	0.100	0.085	0.085	0.095
80	0.165	0.140	0.125	0.135
85	0.870	0.570	0.295	0.160
90	1.030	0.925	0.755	0.210
95	1.040	0.930	0.940	0.460
100	1.050	0.930	0.940	1.045
105	1.050	0.930	0.950	1.070
110	1.050	0.935	0.950	1.075
115	1.050	0.935	0.950	1.090
120	1.050	0.940	0.950	1.090
125	1.050	0.940	0.950	1.090
130	1.050	0.940	0.950	1.090
125	1.050	0.940	0.950	1.090
120	1.050	0.940	0.950	1.090
115	1.050	0.940	0.950	1.090
110	1.050	0.940	0.950	1.090
105	1.050	0.940	0.950	1.090
100	1.050	0.940	0.950	1.090
95	1.050	0.940	0.950	1.090
90	1.050	0.940	0.950	1.090
85	1.050	0.940	0.950	1.090
80	1.050	0.940	0.950	1.080
75	1.050	0.940	0.945	1.060
70	1.050	0.940	0.940	1.035
65	1.050	0.925	0.925	0.490
60	1.050	0.925	0.675	0.330
55	1.050	0.890	0.385	0.145
50	1.050	0.500	0.260	0.095
45	0.980	0.380	0.160	0.070
40	0.820	0.295	0.055	0.040
35	0.730	0.245	0.025	0.020
30	0.685	0.190	0.000	0.000
25	0.640	0.185	0.000	0.000

Table C1. Experimental temperature-contraction results for Ni<sub>49</sub>Ti<sub>51</sub> wire.

\* Owing to an error during the procedure, a 22 gram load was used.

Table C1 displays the experimental results obtained for the  $\text{Ni}_{49}\text{Ti}_{51}$  wire. The wire which was cycled under the 2 gram load (4.3 MPa) required an 82 gram load (176 MPa) to return the wire to its initial length. The wire which was cycled under the 22 gram load (47 MPa) required a 62 gram load (133 MPa) to return to its initial length. Figures C2-C5 show the experimental temperature-strain curves for the  $\text{Ni}_{49}\text{Ti}_{51}$  wire. Figure C6 shows the relationships of  $M_s$ ,  $M_f$ ,  $A_s$  and  $A_f$  to wire stress by incorporating the experimental results plotted in Figures C2-C5.

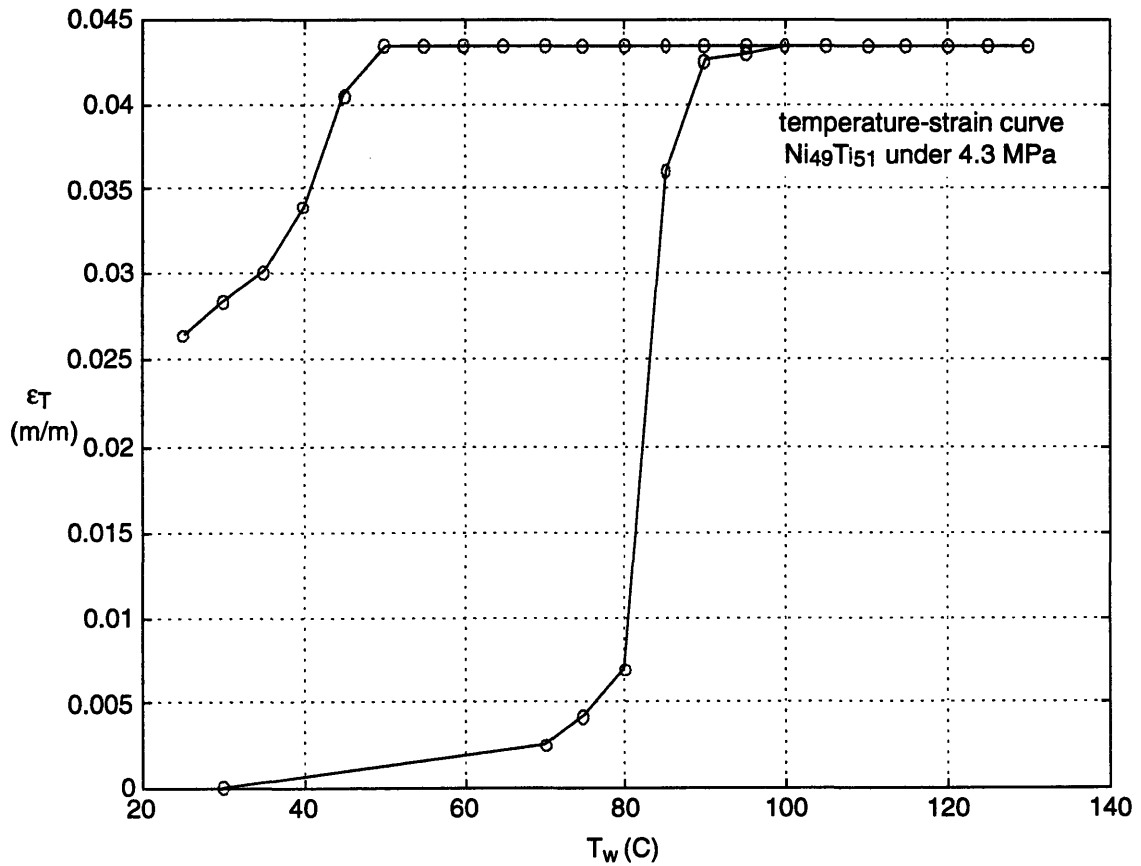


Figure C2. Experimental temperature-strain curve of a 4.3 MPa biased  $\text{Ni}_{49}\text{Ti}_{51}$  wire

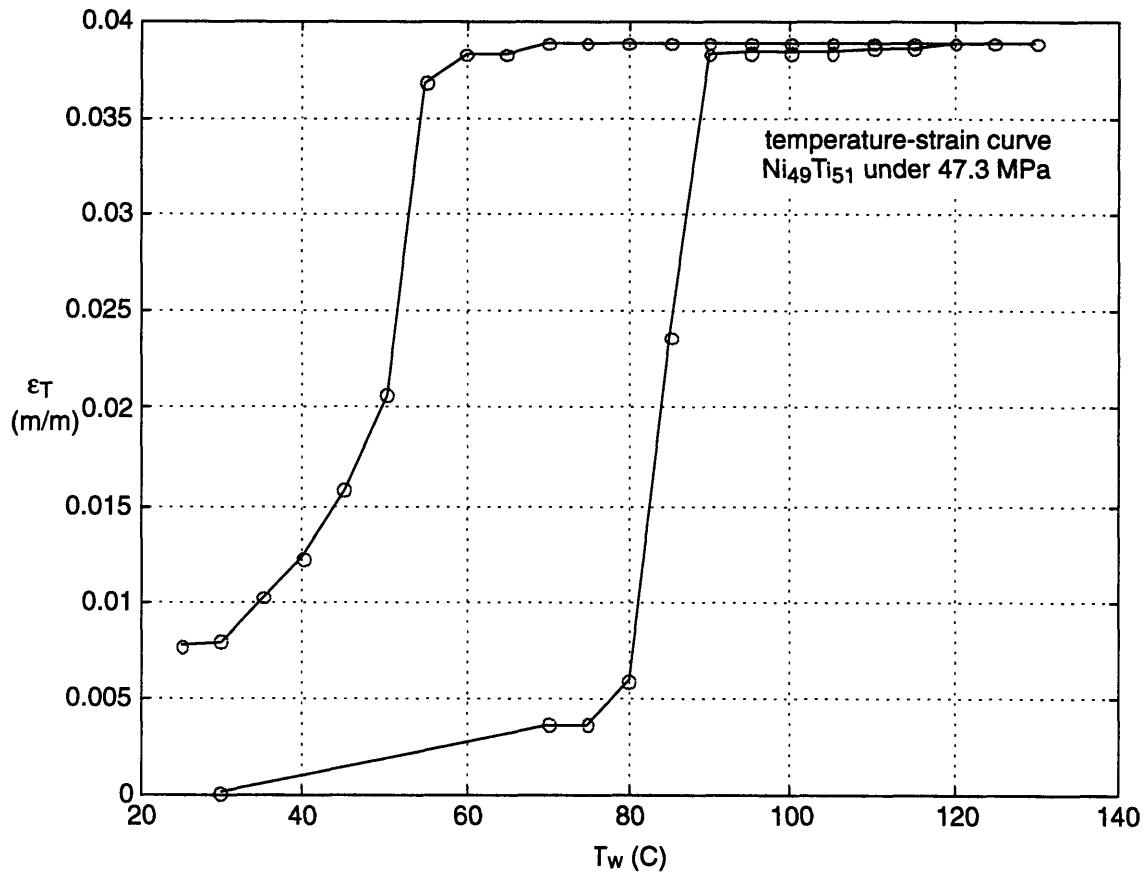


Figure C3. Experimental temperature-strain curve of a 47.3 MPa biased Ni<sub>49</sub>Ti<sub>51</sub> wire.

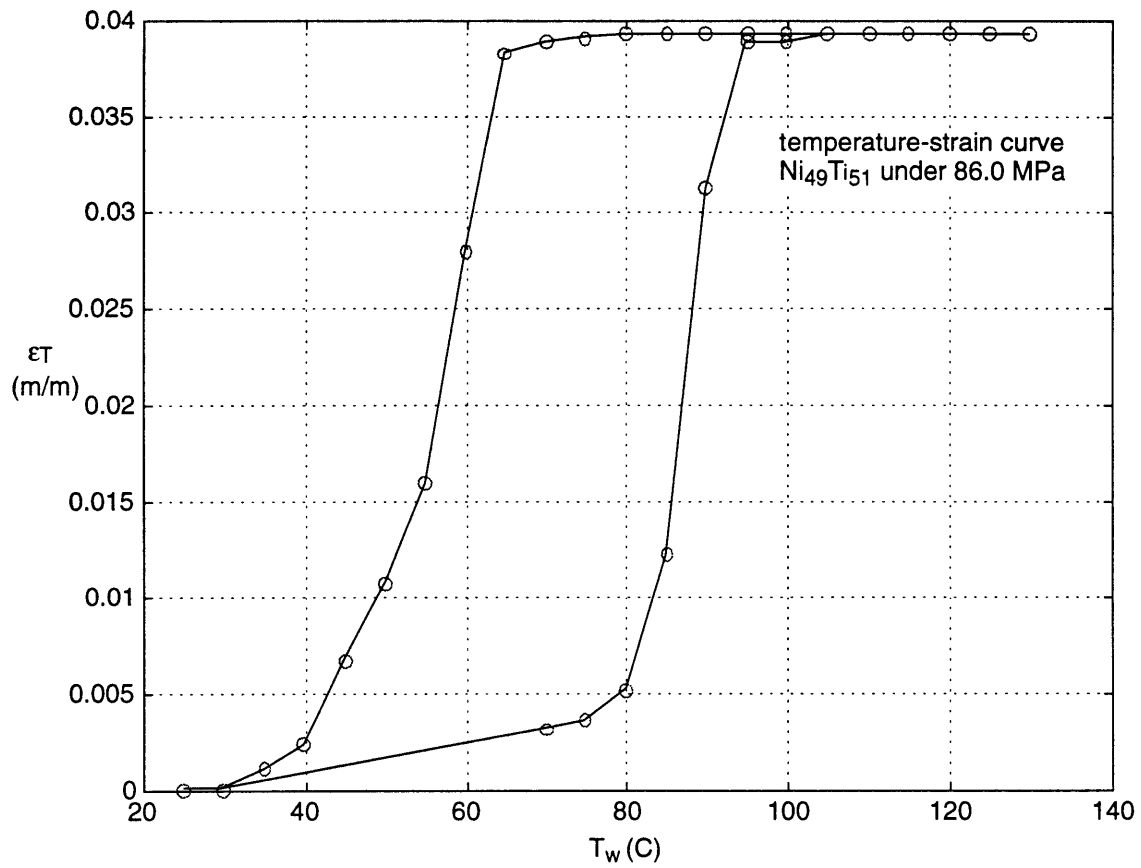


Figure C4. Experimental temperature-strain curve of a 86.0 MPa biased Ni<sub>49</sub>Ti<sub>51</sub> wire.

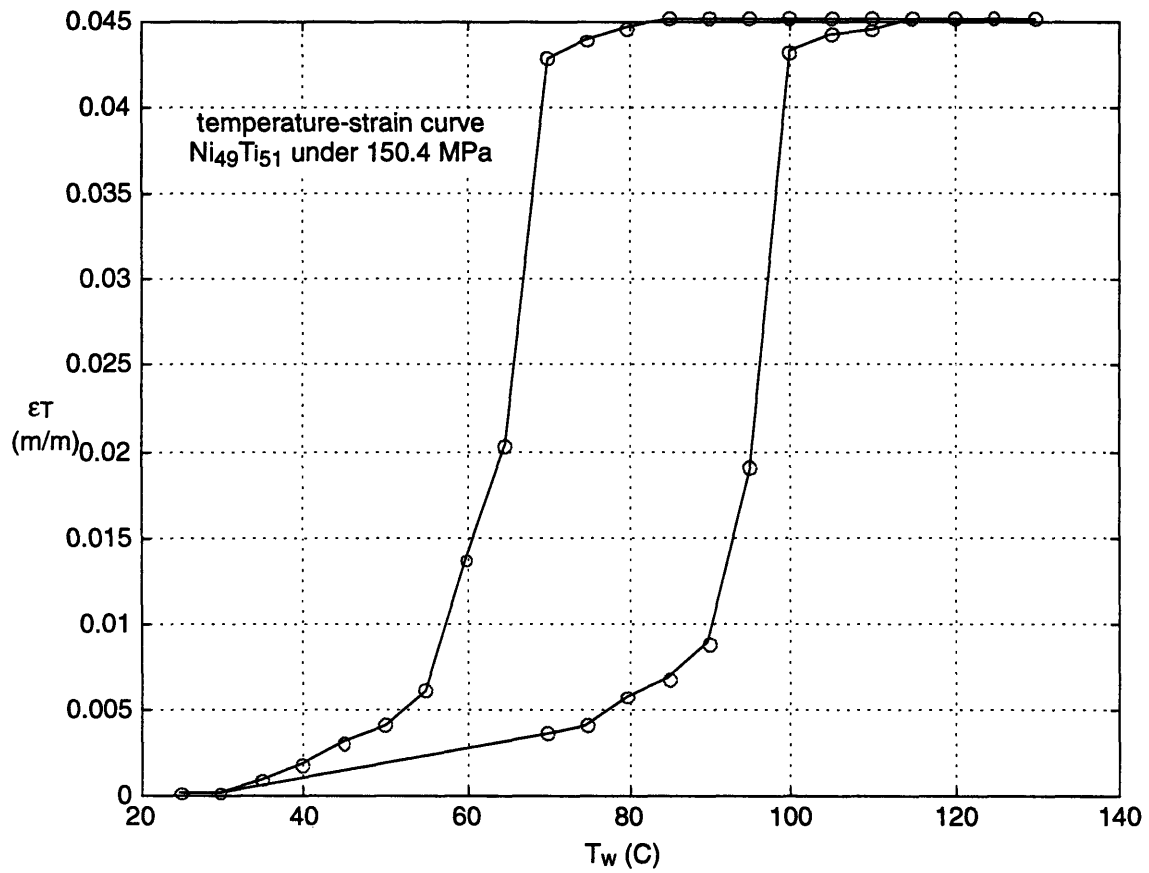


Figure C5. Experimental temperature-strain curve of a 150.4 MPa biased Ni<sub>49</sub>Ti<sub>51</sub> wire.

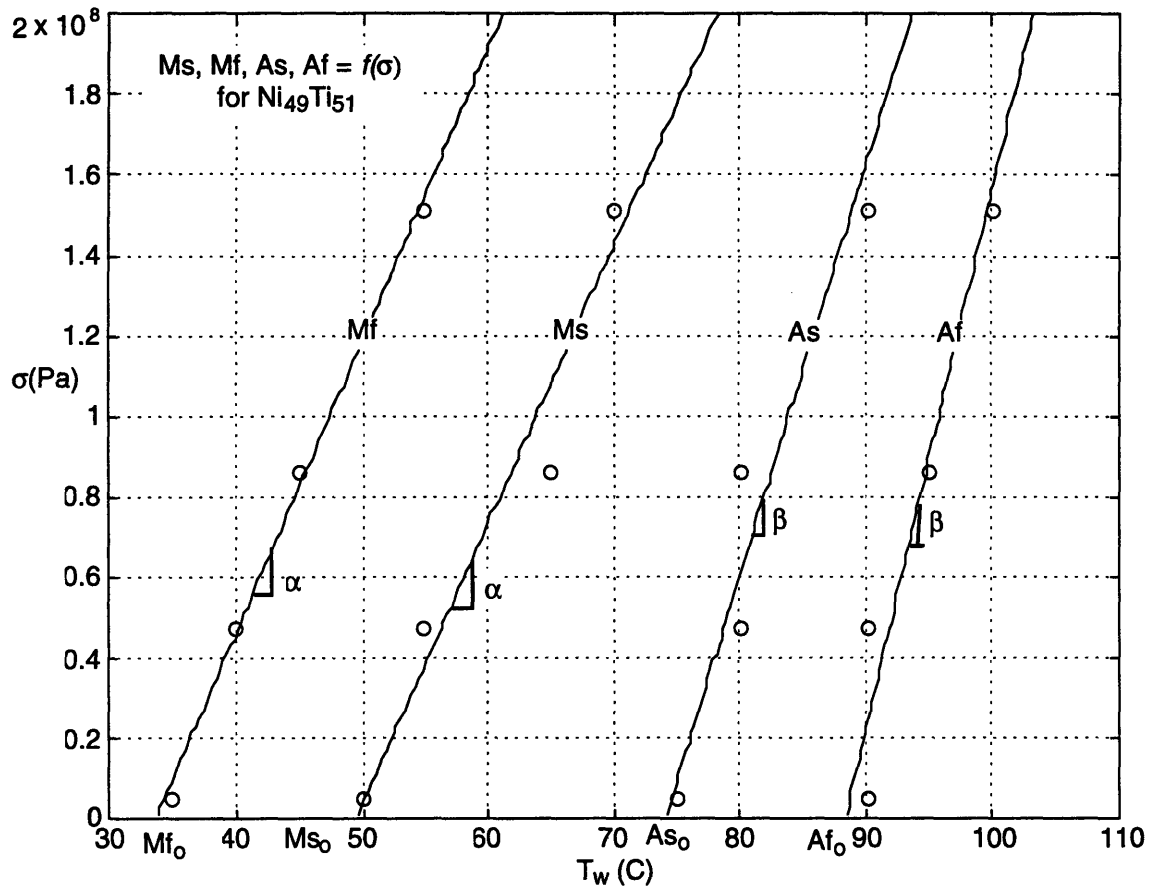


Figure C6. Transformation temperatures-stress curves (Ms, Mf, As, Af) for Ni<sub>49</sub>Ti<sub>51</sub> wire.

Load	2 grams	20 grams	40 grams	70 grams
Temperature of Oven (Centigrade)	Change in Length (inches)			
55	0.118	0.117	0.070	0.120
58	0.137	0.125	0.090	0.130
60	0.155	0.135	0.095	0.155
63	0.188	0.155	0.105	0.170
65	0.286	0.170	0.145	0.190
68	0.749	0.356	0.150	0.205
70	0.780	0.670	0.195	0.230
73	0.785	0.710	0.633	0.248
75	0.785	0.710	0.725	0.275
78	0.785	0.710	0.725	0.580
80	0.785	0.710	0.725	0.930
83	0.785	0.710	0.725	0.930
85	0.785	0.710	0.725	0.930
83	0.785	0.710	0.725	0.930
80	0.785	0.710	0.725	0.930
78	0.785	0.710	0.725	0.930
75	0.785	0.710	0.725	0.930
73	0.785	0.710	0.725	0.930
70	0.785	0.710	0.725	0.930
68	0.785	0.710	0.725	0.930
65	0.785	0.710	0.725	0.905
63	0.785	0.710	0.725	0.595
60	0.785	0.710	0.725	0.250
58	0.785	0.705	0.690	0.240
55	0.785	0.695	0.160	0.215
53	0.785	0.205	0.135	0.200
50	0.524	0.162	0.120	0.180
48	0.421	0.155	0.120	0.175
45	0.380	0.145	0.100	0.140
43	0.375	0.130	0.085	0.135
40	0.375	0.130	0.080	0.095
25	0.328	0.060	0.015	0.000

Table C2. Experimental temperature-contraction results for Ni<sub>49</sub>Ti<sub>44</sub>Cu<sub>7</sub> wire.

Table C2 displays the experimental results obtained for the Ni<sub>49</sub>Ti<sub>44</sub>Cu<sub>7</sub> wire. The wire which was cycled under the 2 gram load (4.3 MPa) required a 65 gram load (140 MPa) to return the wire to its initial length. The wire which was cycled under the 20 gram load (43 MPa) required a 65 gram load (140 MPa) to return to its initial length. The wire which was cycled under the 40 gram load (86 MPa) required a 65 gram load (140 MPa) to return to its initial length. Figures C7-C10 show the experimental temperature-strain curves for the Ni<sub>49</sub>Ti<sub>44</sub>Cu<sub>7</sub> wire. Figure C11 shows the relationships of Ms, Mf, As and Af to wire stress by incorporating the experimental results plotted in Figures C7-C10.

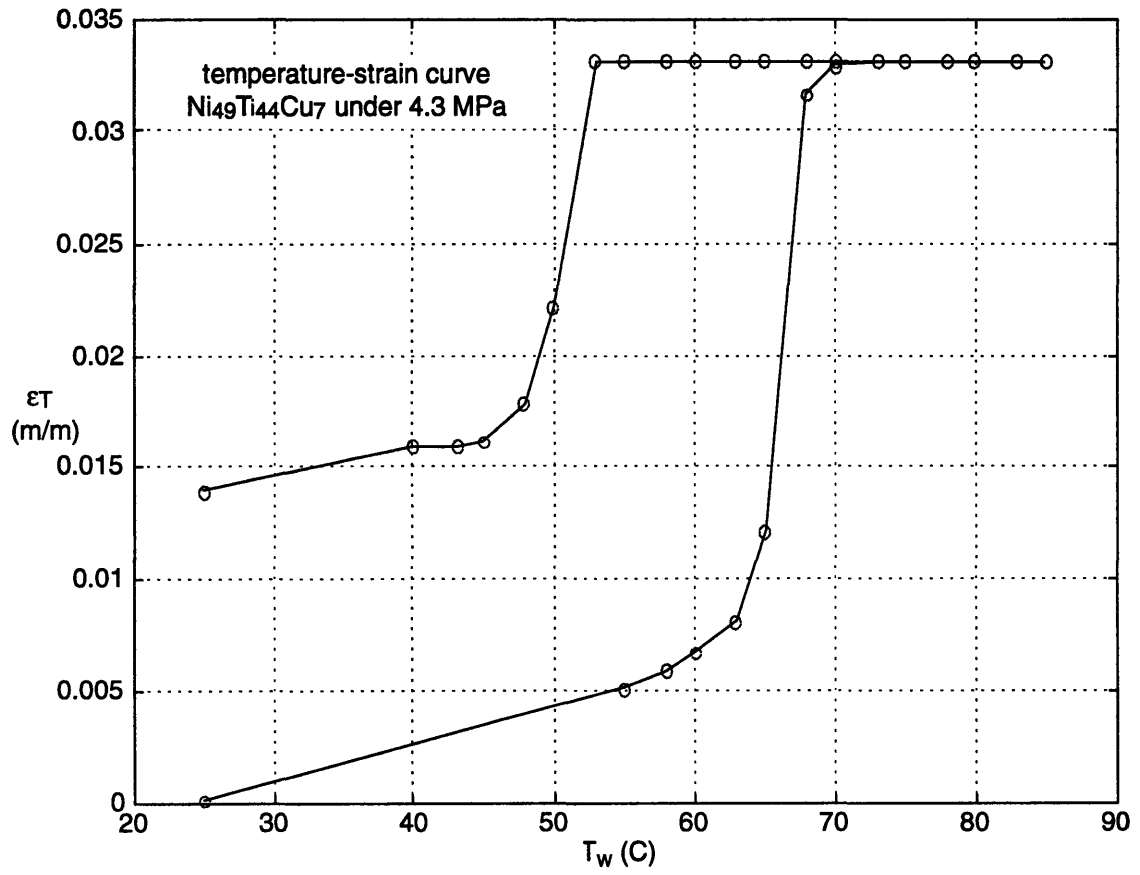


Figure C7. Experimental temperature-strain curve of a 4.3 MPa biased Ni<sub>49</sub>Ti<sub>44</sub>Cu<sub>7</sub> wire.

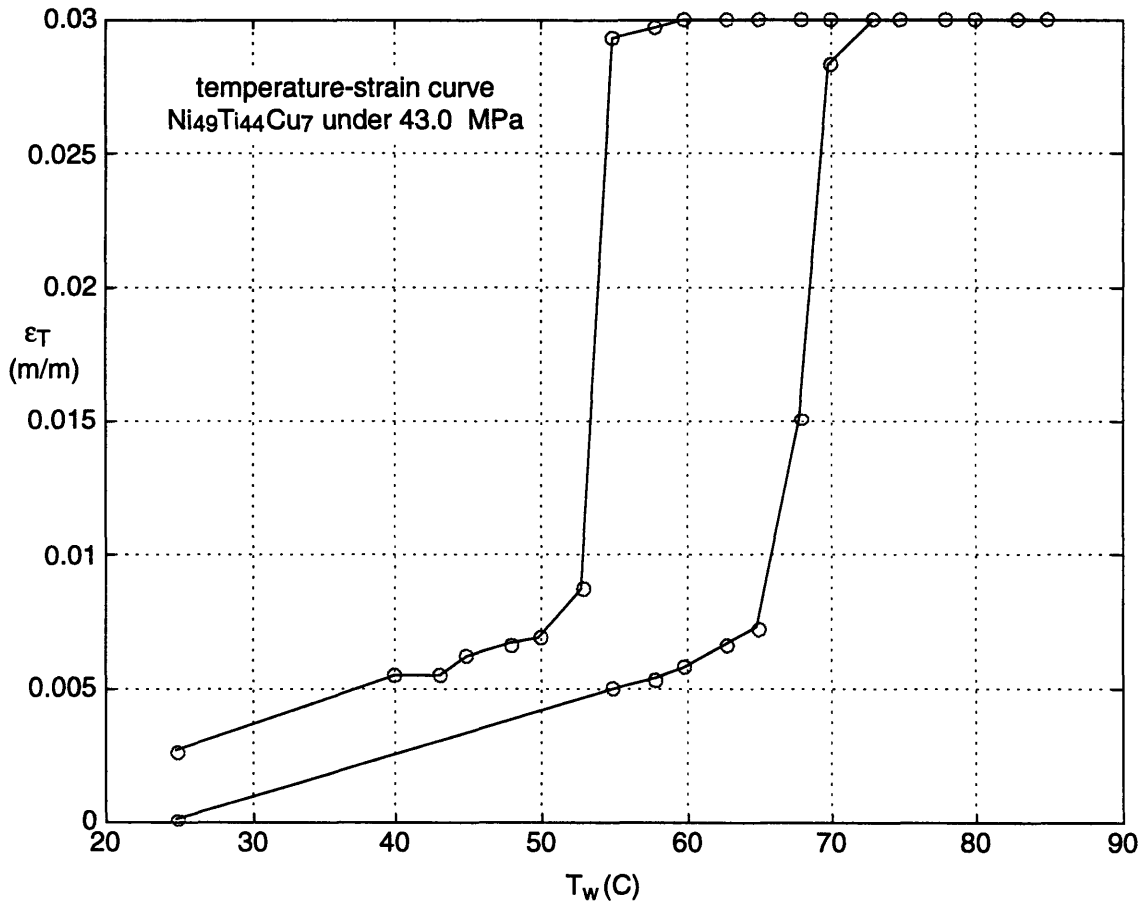


Figure C8. Experimental temperature-strain curve of a 43.0 MPa biased Ni<sub>49</sub>Ti<sub>44</sub>Cu<sub>7</sub> wire.

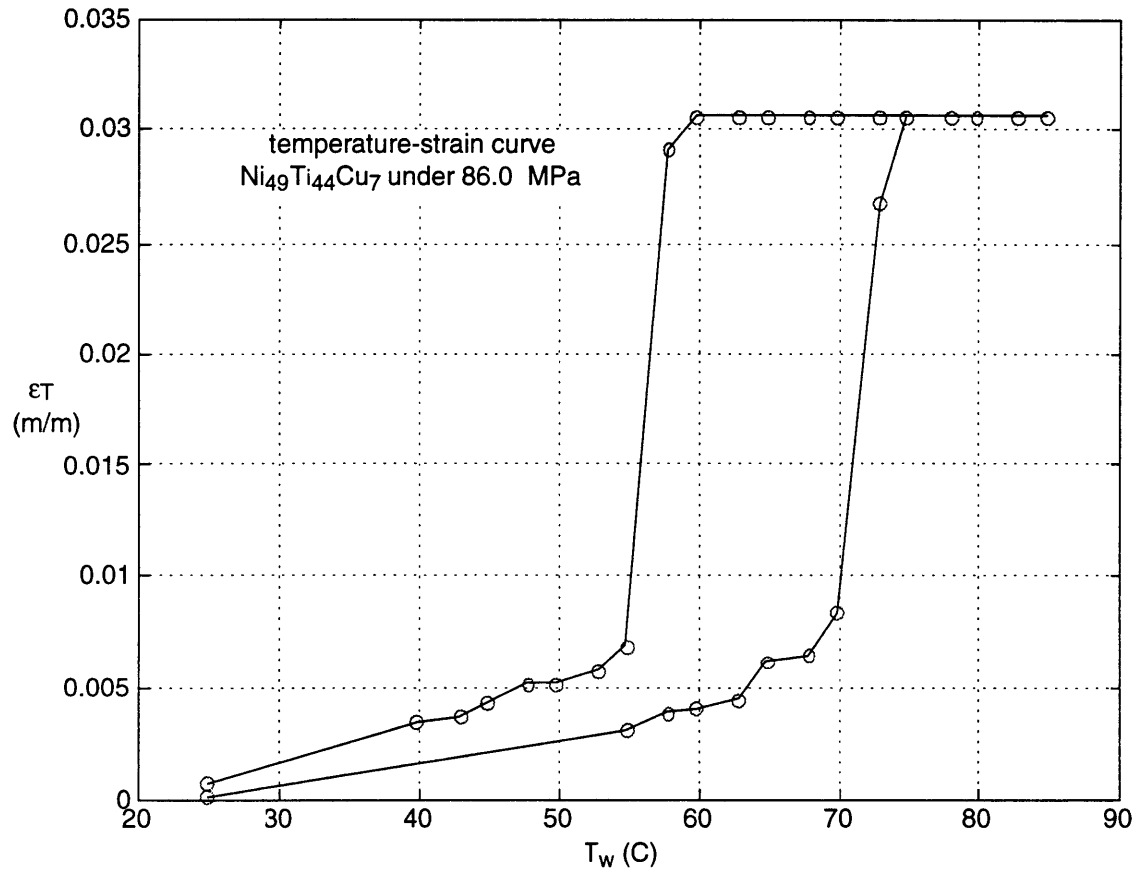


Figure C9. Experimental temperature-strain curve of a 86.0 MPa biased Ni<sub>49</sub>Ti<sub>44</sub>Cu<sub>7</sub> wire.

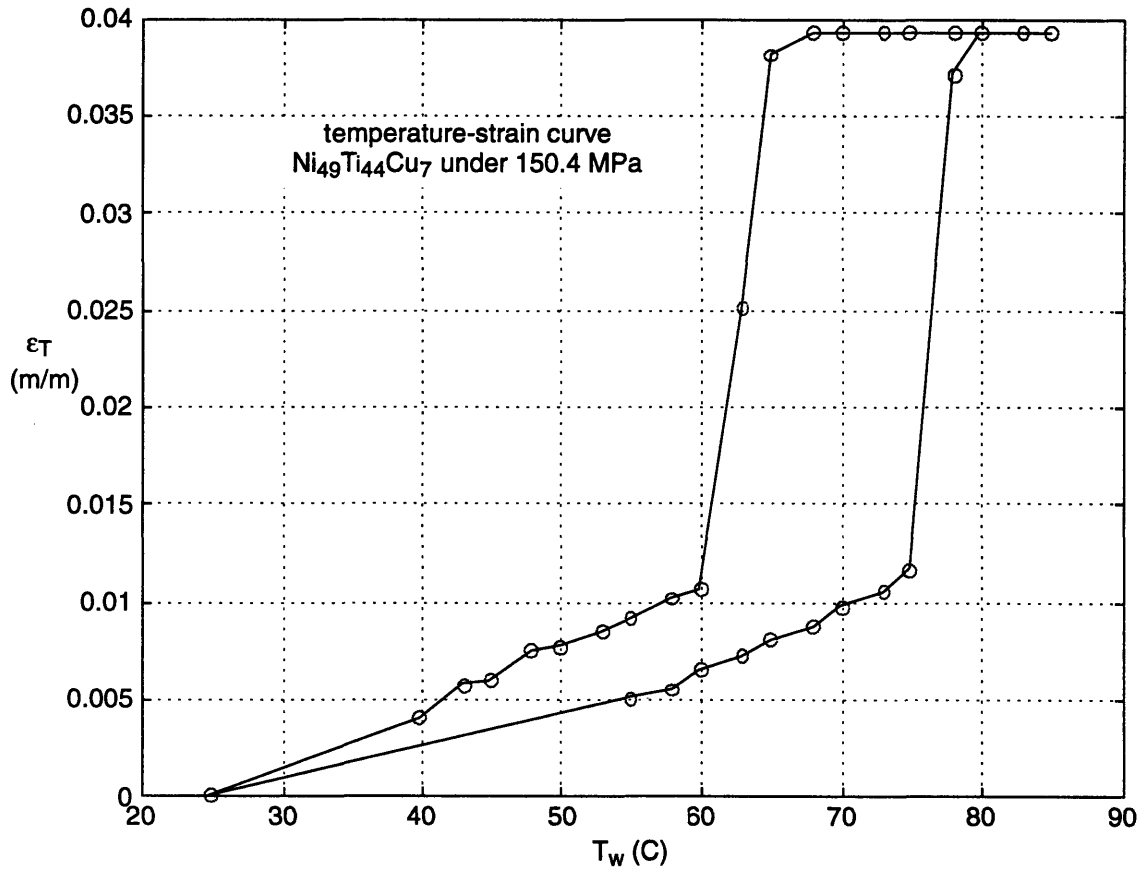


Figure C10. Experimental temperature-strain curve of a 150.4 MPa biased  $\text{Ni}_{49}\text{Ti}_{44}\text{Cu}_7$  wire.

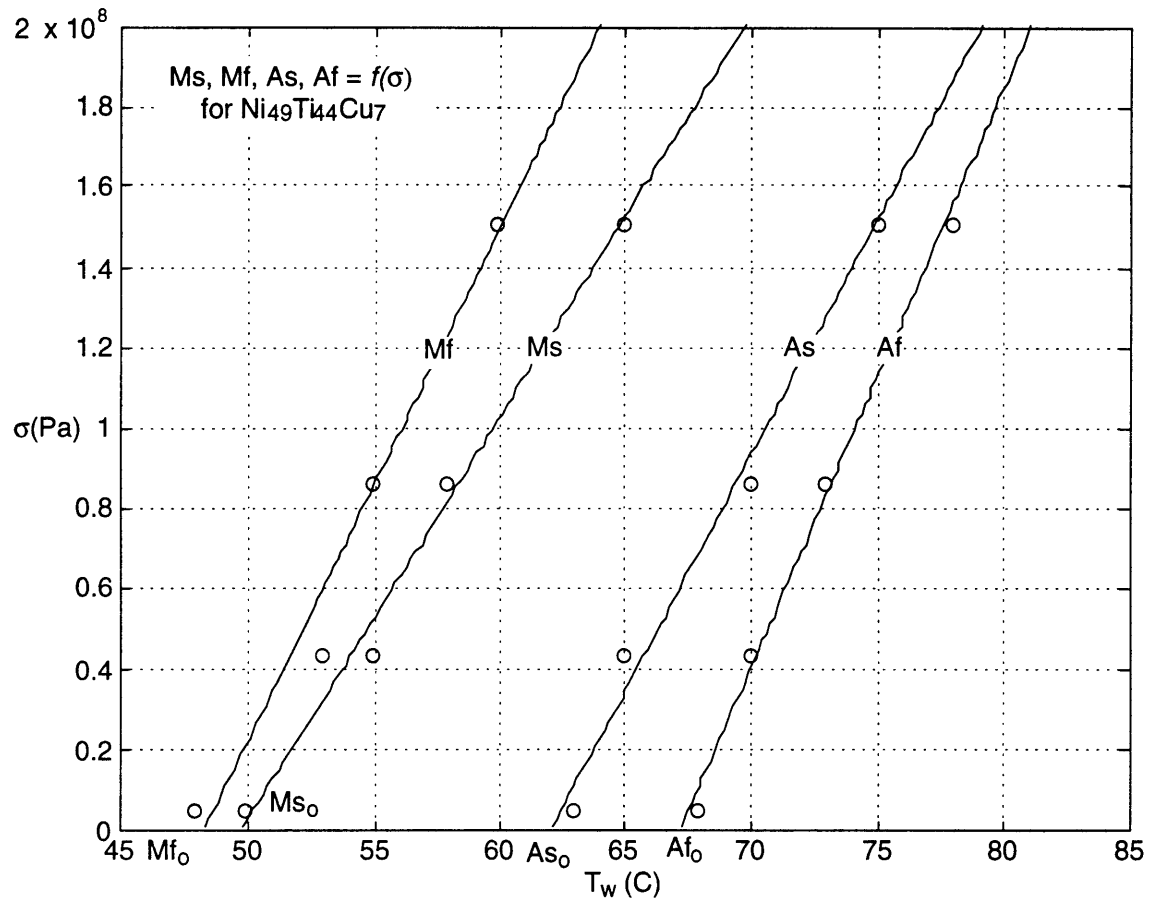


Figure C11. Transformation temperatures-stress curves  
(Ms, Mf, As, Af) for Ni<sub>49</sub>Ti<sub>44</sub>Cu<sub>7</sub> wire.

Load	2 grams	20 grams	40 grams	70 grams
Temperature of Oven (Centigrade)	Change in Length (inches)			
100	0.235	0.170	0.065	0.155
105	0.285	0.195	0.110	0.180
110	0.325	0.195	0.135	0.205
115	0.330	0.195	0.145	0.245
120	0.330	0.195	0.145	0.265
125	0.330	0.195	0.145	0.270
130	0.330	0.195	0.145	0.270
135	0.330	0.195	0.145	0.270
140	0.330	0.195	0.145	0.270
145	0.330	0.195	0.145	0.270
150	0.330	0.195	0.145	0.270
155	0.330	0.195	0.145	0.270
160	0.330	0.195	0.145	0.270
155	0.330	0.195	0.145	0.270
150	0.330	0.195	0.145	0.270
145	0.330	0.195	0.145	0.270
140	0.330	0.195	0.145	0.270
135	0.330	0.195	0.145	0.270
130	0.330	0.195	0.145	0.270
125	0.330	0.195	0.145	0.270
120	0.330	0.195	0.145	0.270
115	0.330	0.195	0.145	0.270
110	0.330	0.195	0.145	0.270
105	0.330	0.195	0.145	0.270
100	0.330	0.195	0.145	0.270
95	0.330	0.195	0.145	0.270
90	0.330	0.195	0.130	0.270
85	0.330	0.160	0.130	0.270
80	0.330	0.160	0.080	0.270
70	0.300	0.150	0.080	0.260
60	0.300	0.130	0.020	0.145
50	0.300	0.125	0.000	0.010
40	0.300	0.120	0.000	0.000

Table C3. Experimental temperature-contraction results for Ni<sub>49</sub>Ti<sub>44</sub>Hf<sub>7</sub> wire.

Table C3 displays the experimental results obtained for the Ni<sub>49</sub>Ti<sub>44</sub>Hf<sub>7</sub> wire. The wire which was cycled under the 2 gram load (4.3 MPa) was unable to return to its initial length, even when given a 92 gram load (198 MPa). The wire which was cycled under the 20 gram load (43 MPa) required a 65 gram load (140 MPa) to return to its initial length. The wire only contracted one-quarter of what was expected. Its Ms and Mf transformation temperatures seemed to be no greater than the Ni<sub>49</sub>Ti<sub>51</sub> wire. No attempt was made to correlate the transformation temperatures to the applied stress. Figures C12 and C13 show

the resulting temperature-strain curves under stresses of 4.3 MPa and 150.4 MPa respectively.

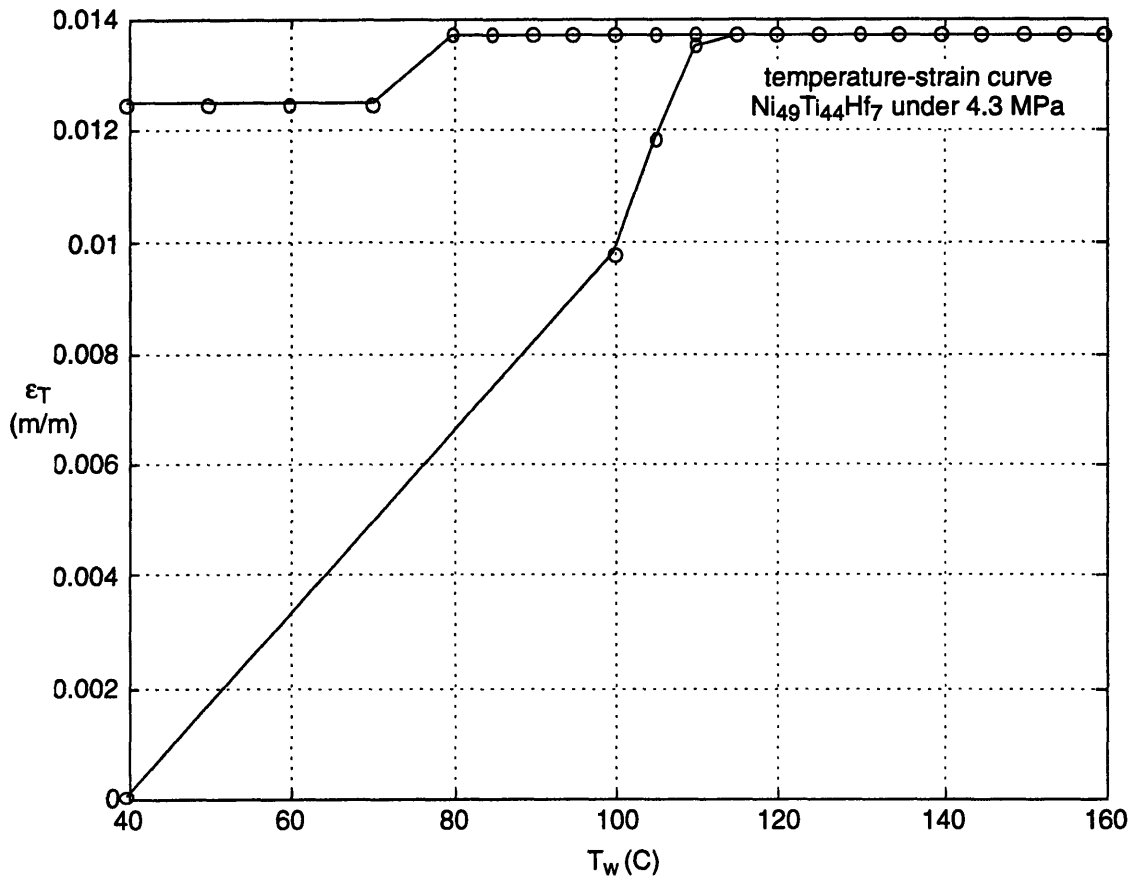


Figure C12. Experimental temperature-strain curve of a 4.3 MPa biased  $\text{Ni}_{49}\text{Ti}_{44}\text{Hf}_7$  wire.

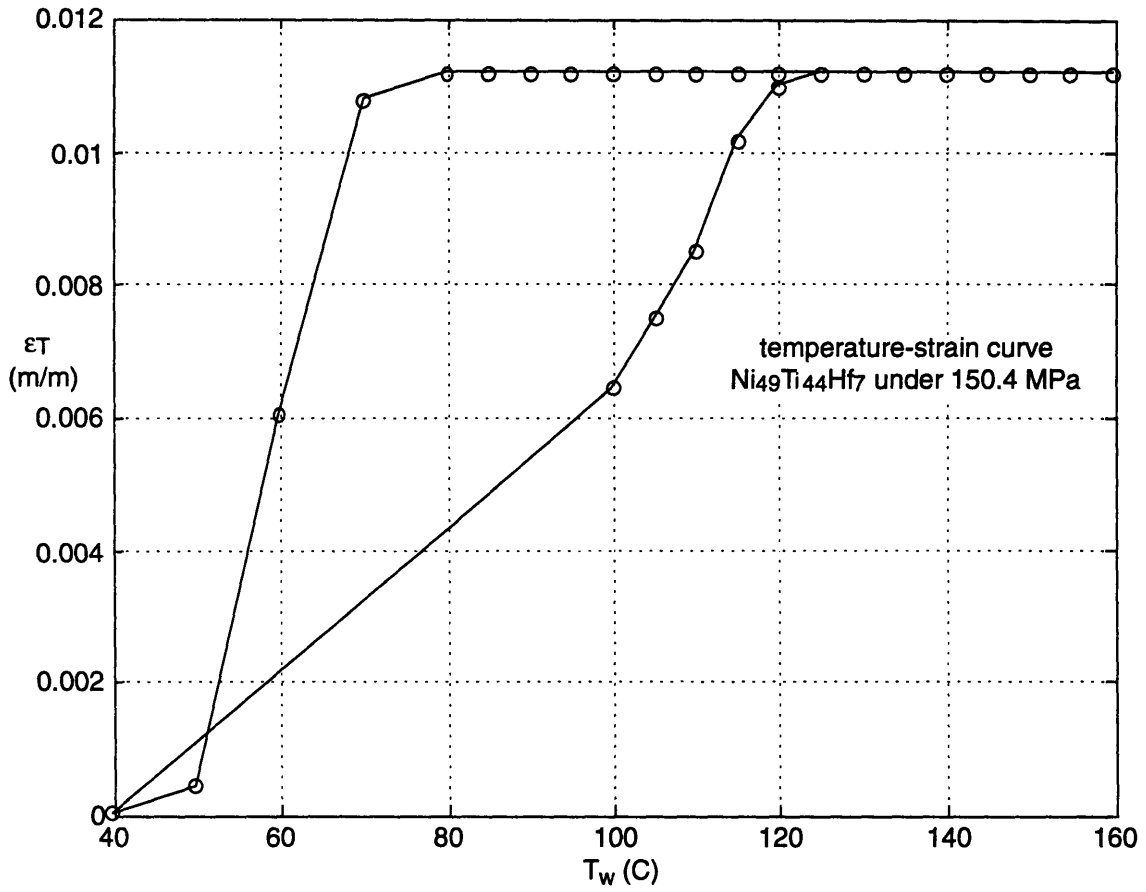


Figure C13. Experimental temperature-strain curve of a 150.4 MPa biased Ni<sub>49</sub>Ti<sub>44</sub>Hf<sub>7</sub> wire.

#### C.4 Experimental materials and apparatus for cycling $Ni_{49}Ti_{51}$ wire.

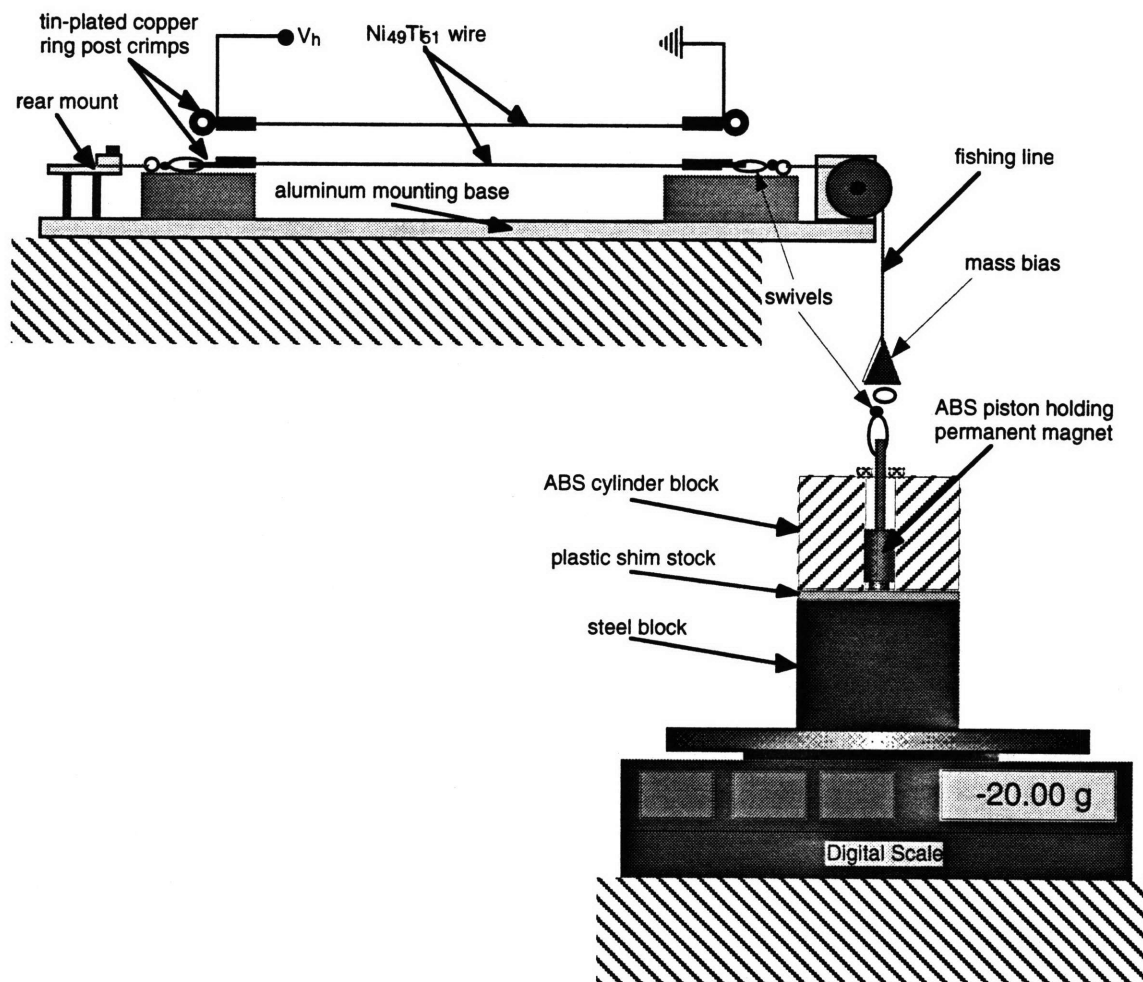


Figure C14. Experimental apparatus used for life-cycle testing of a  $Ni_{49}Ti_{51}$  wire.

Figure C14 illustrates the mechanical apparatus used to actuate a  $Ni_{49}Ti_{51}$  wire under stress. A digital scale is used to verify the peak stress in the wire. A mass is still needed to assist in returning the contracted wire to its original length. The mass was minimized in order to reduce force effects due to acceleration. This occurs because when the wire contracts, the magnetic bias force is near zero. The wire is fastened by two tin-plated copper ring post crimps. The electrical connections were made with .008"-diameter copper wire, also crimped onto the ring posts. Swivels and ABS blocks, which the connectors rested on, were used in order to minimize any constrained bending at the wire connector termination. Fishing line was chosen because it was not only stiffer than the  $Ni_{49}Ti_{51}$  wire, but also

more pliable. Spring steel was initially used for the system connections; however, the material work-hardened around the pulley and failed during life-cycle testing.

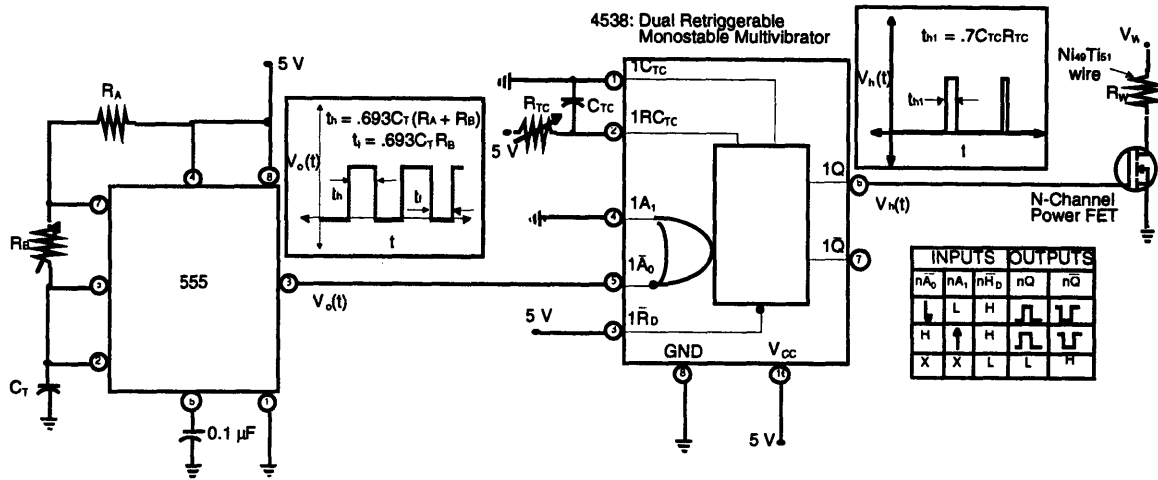


Figure C15. Digital electronic circuit used to thermally cycle Ni<sub>49</sub>Ti<sub>51</sub> wire.

Figure C15 shows the digital logic required to cycle the Ni<sub>49</sub>Ti<sub>51</sub> wire. The 555 timer is used to control the time when the wire should be electrically heated. Each time the square wave, generated by the 555 timer, goes from 5.0 volts to ground (high to low), the 4538 monostable multivibrator creates a 5.0-volt pulse which defines the heating period for the Ni<sub>49</sub>Ti<sub>51</sub> wire. This pulse is sent to the gate of the Power FET, which drives the drain to ground, causing current to flow through the Ni<sub>49</sub>Ti<sub>51</sub> wire. The wire voltage ( $V_w$ ) is set using the circuit illustrated in Figure C16.

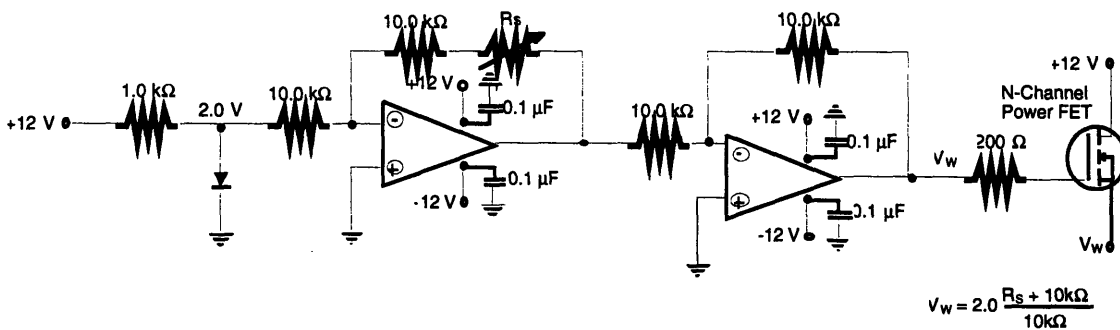


Figure C16. Adjustable voltage supply used to electrically heat Ni<sub>49</sub>Ti<sub>51</sub> wire.

Figure C16 illustrates the adjustable voltage supply for the Ni<sub>49</sub>Ti<sub>51</sub> wire. The light-emitting diode provides a 2.0-Volt potential, to be amplified and inverted by the first operational amplifier and variable resistor  $R_s$ . The desired voltage is then re-inverted using the second operational amplifier. The desired voltage is then sent to a voltage follower

created with the Power FET. Unlike a bipolar junction transistor, the field effect transistor does not need to compensate for a 0.6 Volt drop across the gate to source. The power transistor allows a greater level of current to be drawn through the  $\text{Ni}_{49}\text{Ti}_{51}$  wire than the low-power operational amplifiers could have supplied. The voltage can be set by using a digital voltage multi-meter readout, while adjusting the variable resistor.

The number of times the wire was electrically heated was obtained by using an analog switch in conjunction with a calculator. So long as the  $\text{Ni}_{49}\text{Ti}_{51}$  wire did not break, the potential at the FET's drain (Figure C15, the drain is immediately below the  $\text{Ni}_{49}\text{Ti}_{51}$  wire resistance) would cycle from high to low. This electrical cycle closed an analog switch, which completed a circuit that caused the calculator to increment its count. When the  $\text{Ni}_{49}\text{Ti}_{51}$  wire broke, the drain's potential would remain at ground and the calculator would stop counting. This apparatus allowed the experiment to run continuously.

The following materials were used:

1.  $\text{Ni}_{49}\text{Ti}_{51}$  wire ("Flexinol 90-110") manufactured by Dynalloy (4 wires). Effective lengths determined by measured resistance.
  - Diameter 75 microns
  - Length 1 19.9 centimeters (34.9  $\Omega$ )
  - Length 2 19.2 centimeters (33.7  $\Omega$ )
  - Length 3 20.2 centimeters (35.5  $\Omega$ )
  - Length 4 19.5 centimeters (34.2  $\Omega$ )
2. 555 timer
3. 4538 dual retriggerable monostable multivibrator
4. LM324 quadruple operational amplifier
5. two RFP15N05L N-channel power field-effect transistors
6. CD4053B analog multiplexer (analog switch)

7. Samarium Cobalt permanent magnet
  - Diameter .190 inches
  - Length .057 inches
8. plastic shim stock .025 inches thick
9. 2.0-gram mass bias
10. fishing line (10 lb. test)
11. fishing swivels
12. tin-plated copper ring post connectors
13. insulated copper wire for electromagnetic coil windings (.007-inch diameter)

The following tools and instruments were used:

1. calibrated digital scale (+/- .005 grams)
2. calibrated digital multi-meter (+/- .005 volts)
3. oscilloscope to calibrate square waves of 555 timer, and one-shot pulses of 4538
4. digital calculator
5. 125-Watt power supply (+12 V, -12 V, +5 V)

### **C.5 Experimental procedure for cycling $Ni_{49}Ti_{51}$ wire.**

1. Solder copper wires onto ring post connectors.
2. Crimp ring post connectors onto  $Ni_{49}Ti_{51}$  wire (actuating length approximately 20.0 centimeters).
3. Zero digital scale with steel block, shim stock and cylinder with piston assembly.
4. Record maximum break-away force of permanent magnet piston (72 grams).
5. Attach ring posts and wire to swivel assembly.
6. Use the rear mount and fishing line to fasten the system with approximately 0.2 Newtons tension (20 grams).
7. Set actuation voltage with digital multi-meter to 8.00 Volts.
8. Measure and record the resistance of the wire.
9. Adjust heating time as follows:
  - $t_h = .0066R_w$
  - $R_{TC} = t_h / (9 \times 10^{-7})$ , ( $C_{TC} = 1.3 \mu F$ )
10. Initialize calculator counter to zero.
11. Attach electrical connectors to copper wires.
12. Cycle until the wire breaks, and record the number of cycles.
13. Repeat steps 1-12 until all four wires have been broken, or have reached nearly one million cycles.

### **C.6 Experimental results from cycling $Ni_{49}Ti_{51}$ wire.**

1. The first wire tested broke at the edge of a ring post crimp.

- L 19.9 centimeters
- R 34.9  $\Omega$
- $t_h$  .2303 seconds
- $\sigma$  160 MPa
- final cycle 16,883

2. The second wire tested broke at the edge of a ring post crimp.

- L 19.2 centimeters
- R 33.7  $\Omega$
- $t_h$  .2224 seconds
- $\sigma$  160 MPa
- final cycle 8,161

3. The third wire tested did not break.

- L 20.2 centimeters
- R 35.5  $\Omega$
- $t_h$  .2343 seconds
- $\sigma$  160 MPa
- final cycle 1,215,777

4. The fourth wire tested did not break.

- L 19.5 centimeters
- R 34.2  $\Omega$
- $t_h$  .2257 seconds
- $\sigma$  160 MPa
- final cycle 908,942

## Appendix D: Model for Permanent Magnets

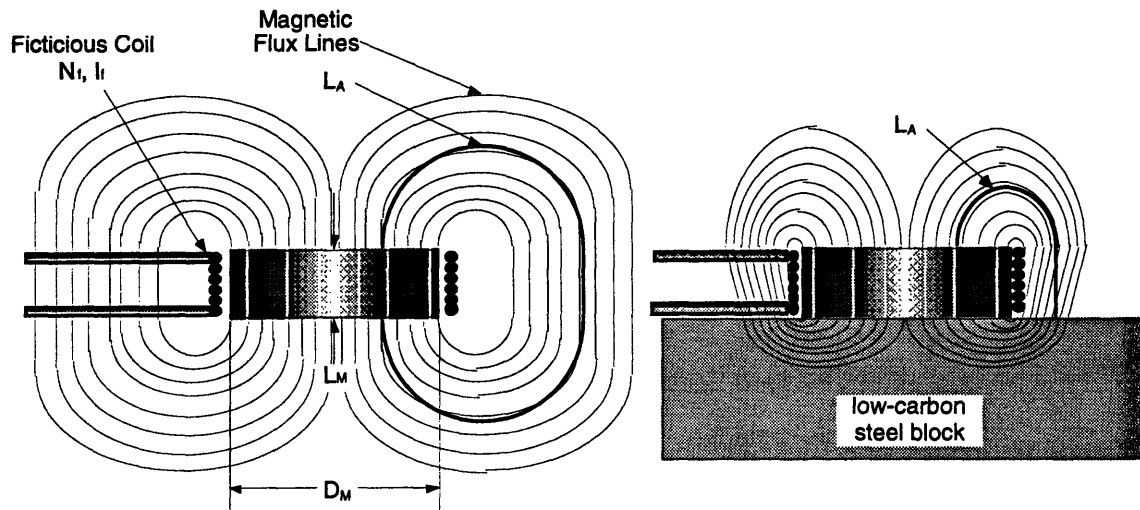


Figure D1. Magnetic fields for a permanent magnet located in free-space and on a low-carbon steel block.

Figure D1 illustrates an approximate sketch of how a permanent magnet's field changes when it is in contact with a low-carbon steel block. A fictitious coil is also placed around the magnet. This coil, along with the sketch of the changing flux paths, will be used to help correlate a method to determine the magnet's normal attractive force to the low-carbon steel block. Fitzgerald (1990) introduced the fictitious coil in order to determine the coenergy of the magnetic field. The partial derivative of the coenergy with respect to the changing distance between the magnet and steel bar ( $x$ ), yields the mechanical force-position ( $x$ ) relationship. The solution to this problem is presented in this Appendix. In Section D.1, Maxwell's Equations are applied in order to relate the flux density and magnetizing force of the permanent magnet to the flux density and magnetizing force of the air. In Section D.2, curves and formulas are presented in order to relate the flux densities to the magnetizing forces for air and permanent magnets. In Section D.3, the flux linkage is introduced as the magnetic field coenergy is determined. In Section D.4, the changing length of the flux path ( $L_A$ ) is related to the changing position ( $x$ ) in order to determine the magnet's attractive force. In Section D.5, the theoretical solution is plotted and compared to experimental results. In Section D.6, the theoretical plots are adjusted with two correction factors derived from the experimental results.

## D.1 Applying Maxwell's Equations

Fitzgerald (1990) refers to the following Equations as the “magneto-quasi-static” form of Maxwell's Equations:

$$\oint_C \mathbf{H} \cdot d\mathbf{l} = \oint_S \mathbf{J} \cdot d\mathbf{a} \quad (\text{D1})$$

$$\oint_S \mathbf{B} \cdot d\mathbf{a} = 0 \quad (\text{D2})$$

Equation D1 introduces the magnetizing force ( $\mathbf{H}$ ), the length of a closed path ( $l$ ), the current density ( $\mathbf{J}$ ), and the surface area through which the current flows ( $a$ ). Equation D1 states that the summed product of the magnetizing forces and the lengths along path  $C$ , is equal to the net current which passes through the surface ( $S$ ) created by  $C$ .

Equation D2 introduces the flux density ( $\mathbf{B}$ ) and the surface area through which the flux flows ( $a$ ). Equation D2 states that for a given sphere in space, the net flux going in and out of the sphere's surface ( $S$ ) will be zero.

Derived from Equation D1, Equation D3 is used to describe the magnet in free-space of Figure D1 as follows:

$$H_M L_M + H_A L_A = N_f I_f \quad (\text{D3})$$

The product of the magnetizing force and length of the mean flux path in the permanent magnet ( $H_M$  and  $L_M$ ), summed with the product of the magnetizing force and length of the mean flux path in the air ( $H_A$  and  $L_A$ ), equals the product of the fictitious coil turns ( $N_f$ ) and current ( $I_f$ ).

Derived from Equation D2, Equation D4 is used to describe the magnet in free-space of Figure D1 as follows:

$$B_M A_M = B_A A_A \quad (\text{D4})$$

The product of the magnet's flux density and cross-sectional surface area normal to flux flow ( $B_M$  and  $A_M$ ), equals the product of the air's flux density and cross-sectional surface

area normal to flux flow ( $B_A$  and  $A_A$ ). In Section D.2, the formulas and curves will be presented to allow Equations D3 and D4 to be combined and modified in order to define the magnetic flux as a function of the geometry and of the permanent magnet's properties.

## **D.2 Equations and curves relating flux density to magnetizing force**

When relating the flux density to magnetizing force in free-space, the following formula is used:

$$B_A = \mu_o H_A \quad (D5)$$

The constant of proportionality ( $\mu_o$ ) is  $4\pi \times 10^{-7}$  (T-m/A). Equation D5 is combined with Equation D4 to obtain the following expression:

$$H_A = \frac{B_M A_M}{\mu_o A_A} \quad (D6)$$

Equation D6 is then combined with Equation D3 to obtain the following expression:

$$H_M L_M + \frac{B_M A_M L_A}{\mu_o A_A} = N_f I_f \quad (D7)$$

In order to eliminate  $H_M$  from Equation D7, the demagnetization curves in Figure A2 are used.

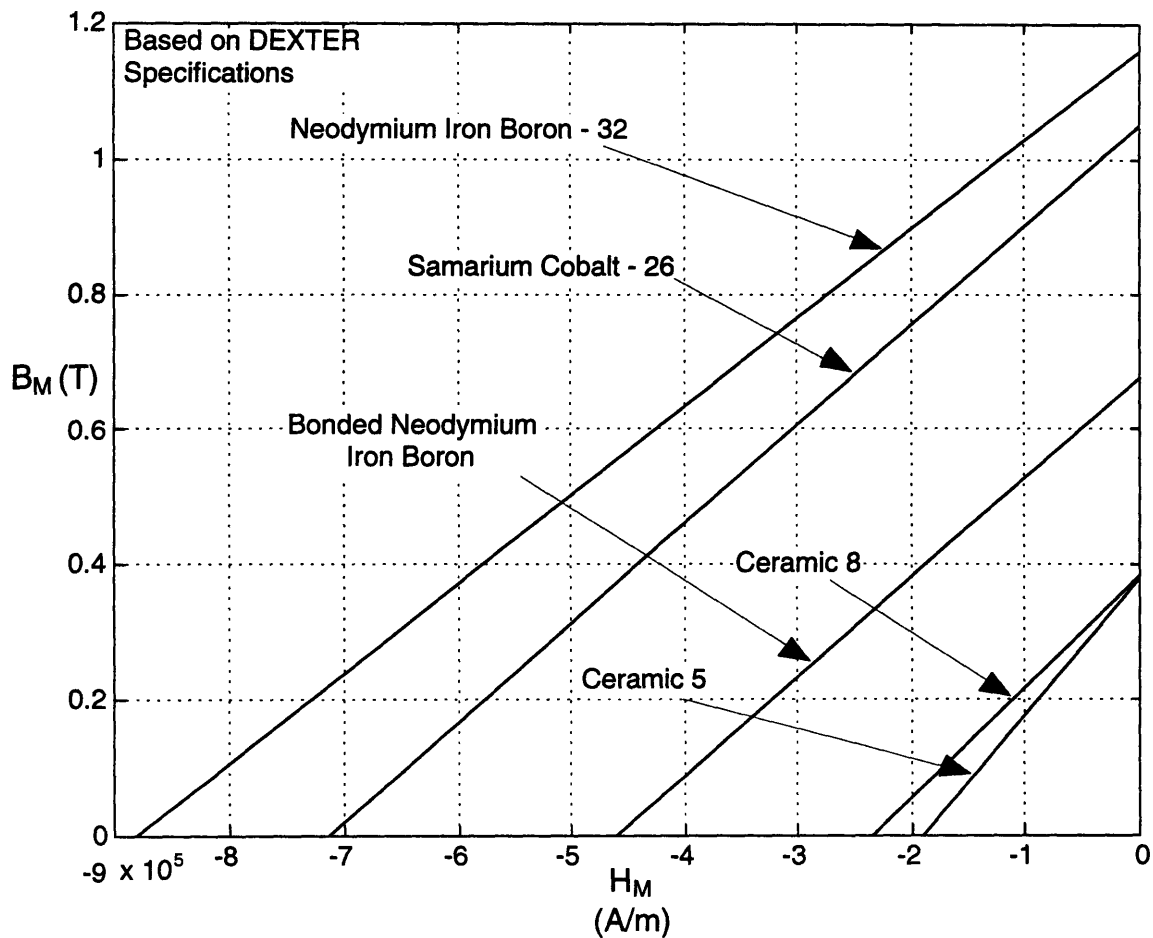


Figure D2. Demagnetization curves for permanent magnets.

The demagnetization curves illustrated can be described by the following formula:

$$B_M = B_r - \frac{B_r}{H_c} H_M \quad (D8)$$

The residual flux density or remanent magnetization ( $B_r$ ) is the flux density when the magnetizing force is zero. Conversely, the coercivity ( $H_c$ ) is the magnetizing force when the flux density is zero. Table D1 lists the residual flux density and coercivity corresponding to the demagnetization curves illustrated in Figure D2.

	Samarium Cobalt -26	Neodymium Iron Boron - 32	Ceramic 5	Ceramic 8	Bonded Neodymium Iron Boron
$B_r$ (T)	1.05	1.16	.380	.385	.68
$H_c$ (kA/m)	-714.0	-881	-191	-235	-460

Table D1. Residual flux densities and coercivities of permanent magnets.

Incorporating Equation D8 into Equation D7 allows the flux density of the magnet as follows:

$$B_M = \frac{N_f i_f - H_c L_M}{\left( \frac{A_M L_A}{\mu_o A_A} - \frac{H_c L_M}{B_r} \right)} \quad (D9)$$

Now that the flux density can be determined, the coenergy of the magnetic field can be determined.

### D.3 Calculating the magnetic coenergy of the permanent magnet field

In order to calculate the permanent magnet's field coenergy, the flux linkage ( $\lambda$ ) needs to be calculated. In order to obtain the flux linkage, the magnetic flux ( $\phi$ ) is calculated as follows:

$$\phi = B_M A_M \quad (D10)$$

With the flux determined, the flux linkage can be calculated as defined by Equation D11.

$$\lambda = N_f \phi = \int e dt \quad (D11)$$

Incorporating Equations D9, D10 and D11, the flux linkage is written as follows:

$$\lambda = A_M N_f \frac{N_f i_f - H_c L_M}{\left( \frac{A_M L_A}{\mu_0 A_A} - \frac{H_c L_M}{B_r} \right)} \quad (D12)$$

With the flux linkage known, the coenergy ( $E'$ ) is determined using the following formula (see Fitzgerald (1990)):

$$E'(i_f=0, x) = \int_0^x F(i_f=I_{f0}, x') dx' + \int_{I_{f0}}^0 \lambda(i_f, x) di_f \quad (D13)$$

Equation D13 has two specific paths for the integration to proceed, because the coenergy is a state function. As a result the integral involving mechanical work ( $Fdx'$ ) is zero. The integral of  $Fdx'$  is zero because the permanent magnet is moved away from the steel bar while the current in the wire is at  $I_{f0}$ . This current eliminates any flux in free-space by bringing the permanent magnet to its coercivity.

$$I_{f0} = \frac{H_c L_M}{N_f} \quad (D14)$$

Since the change in mechanical energy is zero, then Equation D13 can be simplified to:

$$E'(i_f=0, x) = \int_{I_{f0}}^0 \lambda(i_f, x) di_f \quad (D15)$$

Incorporating Equation D12 into Equation D15, the resulting solution is as follows:

$$E' = \frac{\frac{H_c^2 L_M^2 A_M}{2}}{\left( \frac{A_M L_A}{\mu_0 A_A} - \frac{H_c L_M}{B_r} \right)} \quad (D16)$$

Note that the fictitious coil has disappeared from the coenergy, which is to be expected. In order to calculate the resulting force ( $F$ ), the mean flux length in the air ( $L_A$ ) needs to be

related to the magnet's position relative to the top of the steel bar (x). Section D.4 addresses that issue, and determines the formula governing the resulting force (F).

#### **D.4 Determining the magnetic pulling force on a steel bar**

To obtain the resulting magnetic force (F), the following formula is used:

$$F = \frac{\partial \mathcal{E}'}{\partial x} \quad (\text{D17})$$

In order to solve Equation D17, the coenergy must be a function of x. The coenergy dependence on x is obtained by developing the relationships between  $L_A$  and x. Figure D1 shows that the initial mean length of the flux path in the air ( $L_{Ai}$ ) is defined as follows:

$$L_{Ai} = \pi D_M + L_M \quad (\text{D18})$$

When the magnet is in contact with the low-carbon steel bar, the final mean flux length of the flux path in the air ( $L_{Af}$ ) is defined as follows:

$$L_{Af} = \frac{\pi D_M}{4} + L_M \quad (\text{D19})$$

Using Equations D18 and D19, the following general formula for  $L_A$  is as follows:

$$L_A = \frac{\pi D_M}{4} + L_M + \frac{3\pi x}{2} \quad (\text{D20})$$

If the magnet is a distance  $x = DM/2$  away from the steel bar, Equation D20 equals Equation D18. Although Figure D1 indicates that the air surface area ( $A_A$ ) decreases when the magnet is in contact with the steel bar, the surface area will be held constant. The resulting air surface area through which the flux flows can be approximated as follows:

When a magnet is in free-space (Figure D1), the ratio of the magnetic flux density to the magnetizing force of the permanent magnet can be determined using the modified formula given by Moskowitz (1995):

$$\frac{B_M}{H_M} = -1.26 \times 10^{-6} \left[ \frac{L_M}{\left(\frac{D_M}{2}\right)^2} \sqrt{\frac{D_M}{2} \left(\frac{D_M}{2} + L_M\right)} \right] \quad (D21)$$

Using Equation D21 in conjunction with Equation D7 (setting the coil current to zero), the resulting surface area of the air in free-space is determined.

$$A_A = - \left( \frac{B_M}{H_M} \right) \frac{A_M L_M}{\mu_o L_M} \quad (D22)$$

Incorporating Equation D20 in to Equation D16 allows Equation D17 to be solved.

$$F = \frac{\frac{\pi H_c^2 L_M^2 A_M^2}{2 \mu_o A_A}}{\left( \frac{-H_c L_M}{B_r} + \frac{A_M L_M}{\mu_o A_A} + \frac{\pi D_M A_M}{4 \mu_o A_A} + \frac{3 \pi A_M}{2 \mu_o A_A} x \right)^2} \quad (D23)$$

With the theoretical method presented, the theoretical results are plotted alongside the experimental results. These results are presented in Section D.5.

### D.5 Theoretical and experimental magnetic force to gap results

Appendix E discusses the experiments performed on 5 different permanent magnets. The experimental results and the theoretical results are presented in Figures D3-D7.

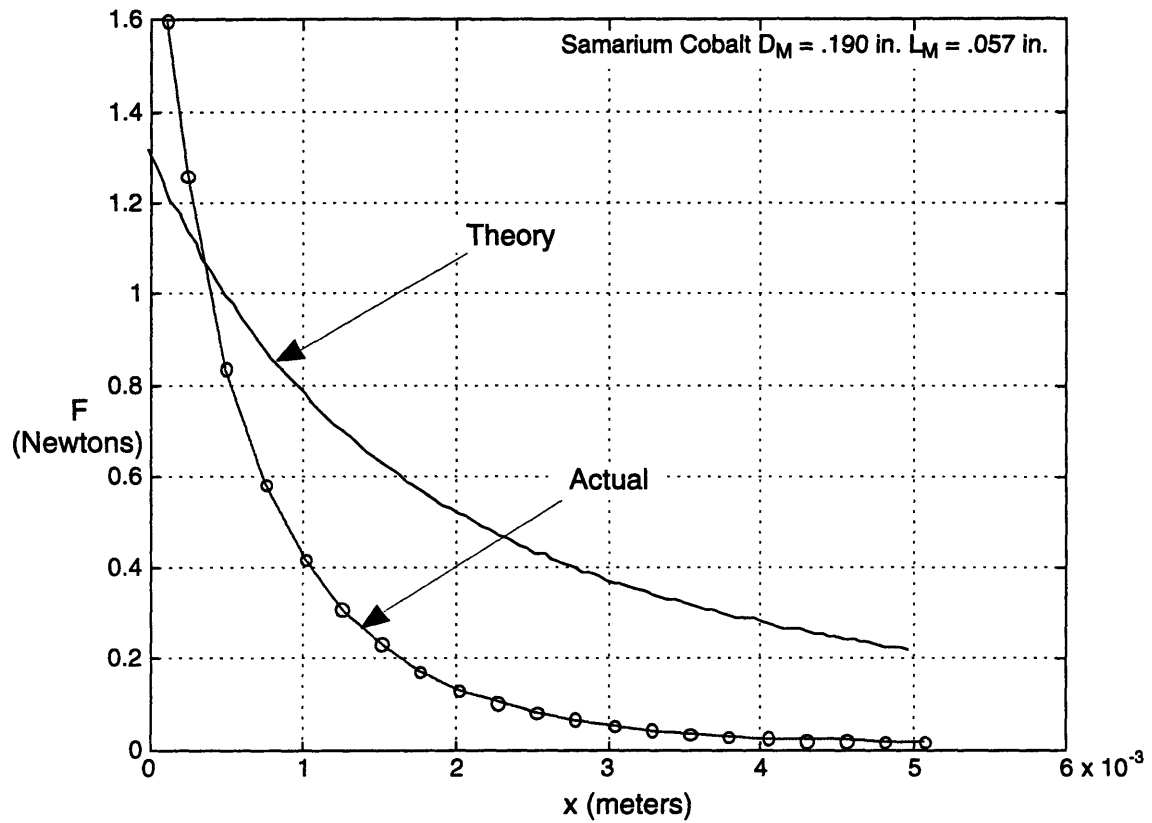


Figure D3. Force-gap curves for Samarium Cobalt.

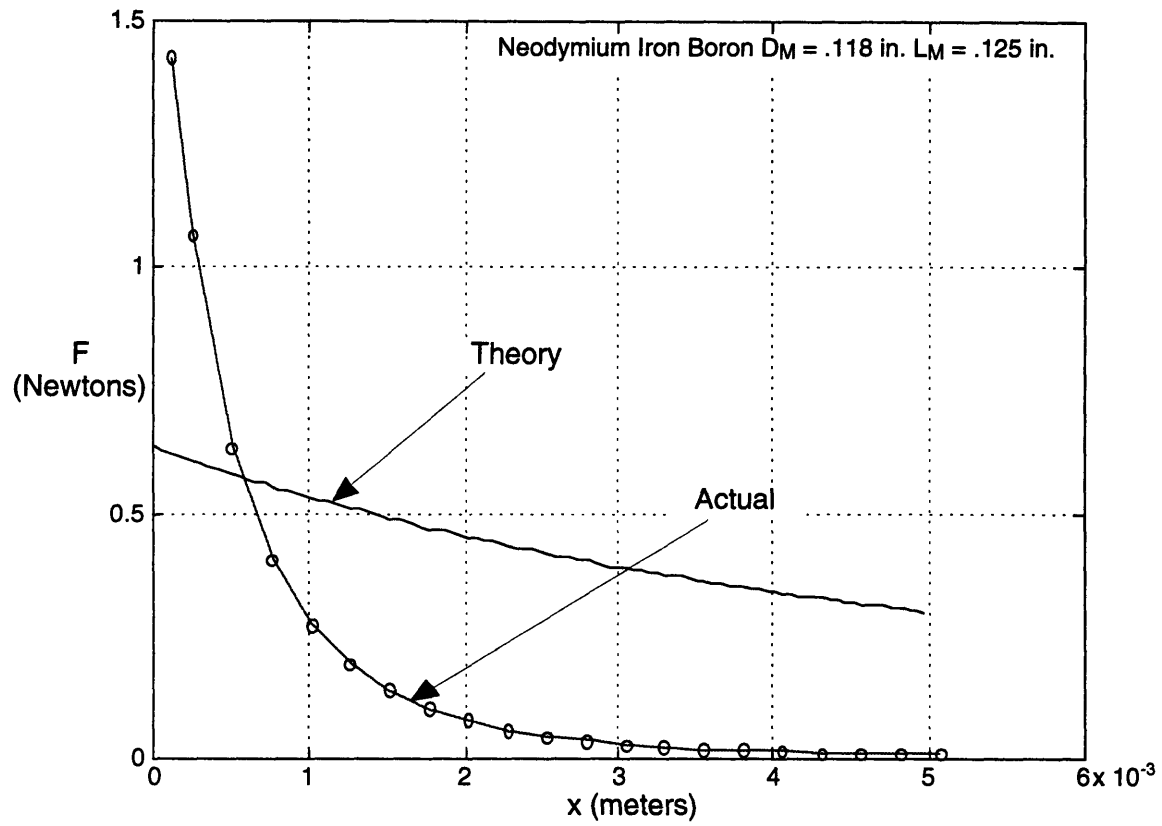


Figure D4. Force-gap curves for Neodymium Iron Boron.

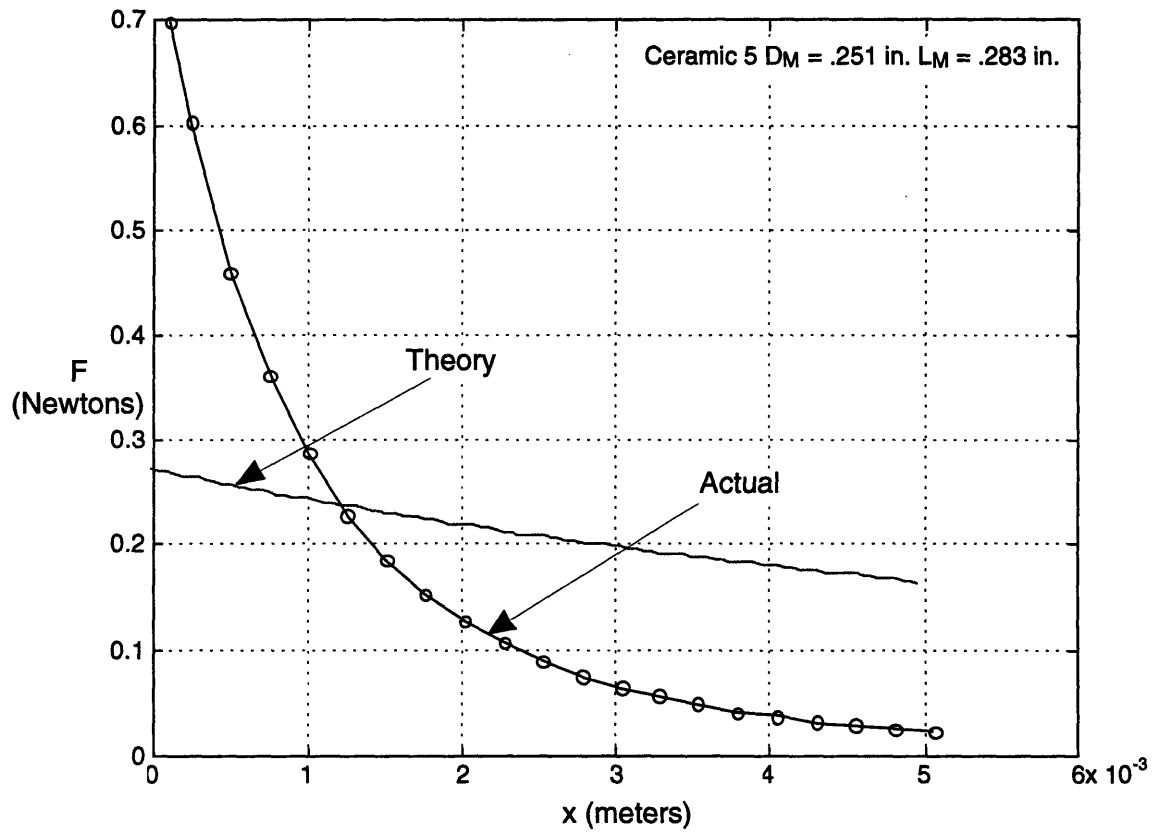


Figure D5. Force-gap curves for Ceramic 5.

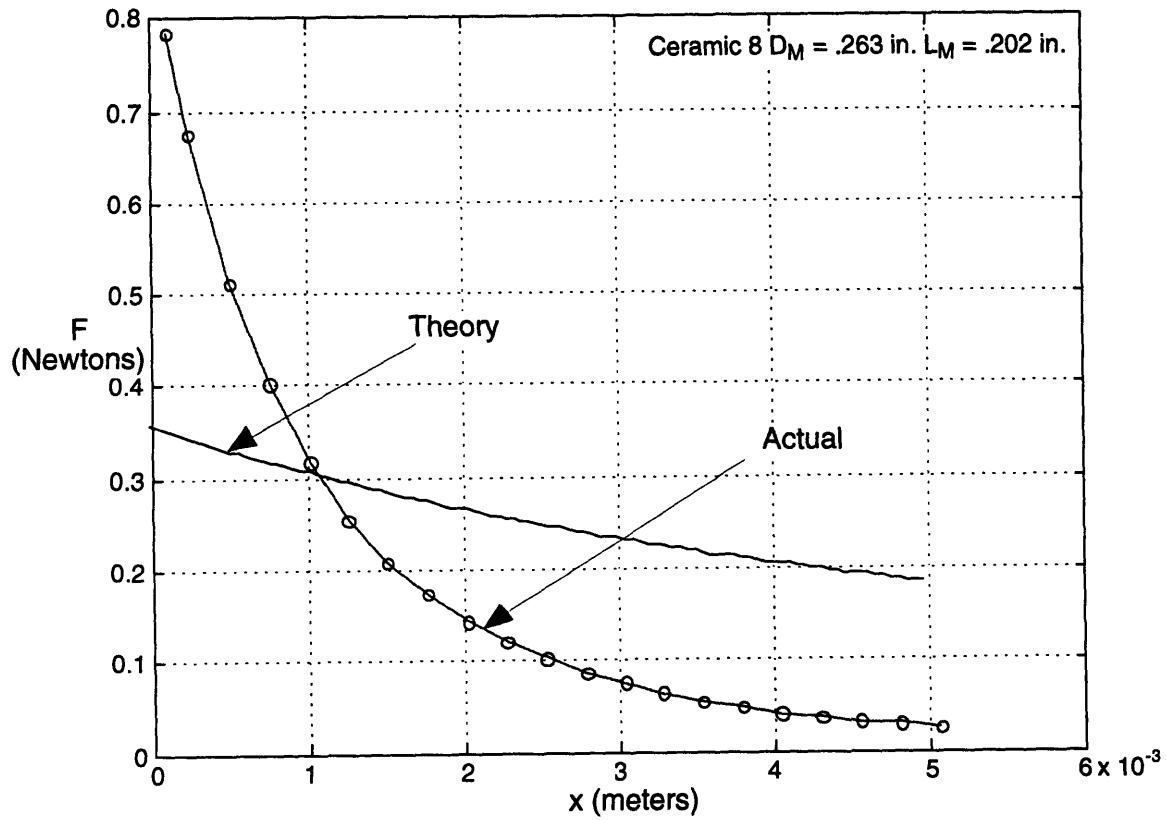


Figure D6. Force-gap curves for Ceramic 8.

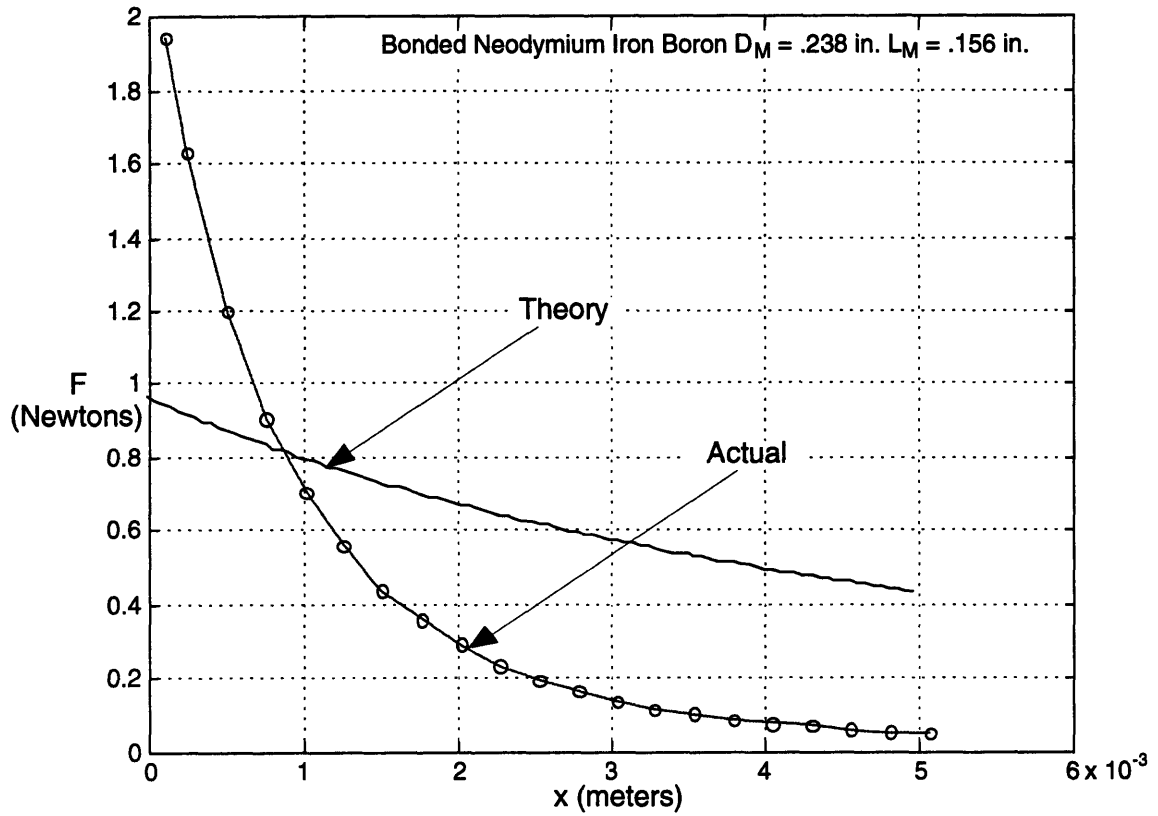


Figure D7. Force-gap curves for Bonded Neodymium Iron Boron.

Figures D3-D7 indicate that the theoretical curves need to be modified in order to match the experimental results. This modification is accomplished by determining two correction factors ( $Cf_1$  and  $Cf_2$ ). Section D.6 discusses the implementation of these correction factors.

## D.6 Theoretical results with correction factors.

In order to correct the theoretical force-gap curves in Section D.5, 2 correction factors ( $Cf_1$  and  $Cf_2$ ) are integrated into Equation D23 as follows:

$$F = \frac{Cf_1 \frac{\pi H_c^2 L_M^2 A_M^2}{2\mu_o A_A}}{\left( \frac{-H_c L_M}{B_r} + \frac{A_M L_M}{\mu_o A_A} + \frac{\pi D_M A_M}{4\mu_o A_A} + Cf_2 \frac{3\pi A_M}{2\mu_o A_A} x \right)^2} \quad (D24)$$

Each theoretical force-gap curve was adjusted so that its resulting correction factors could be correlated to the magnet's diameter-to-length ratio. Figures D8 and D9 indicate that the correction factors have a logarithmic relationship with the magnet's diameter-to-length ratio.

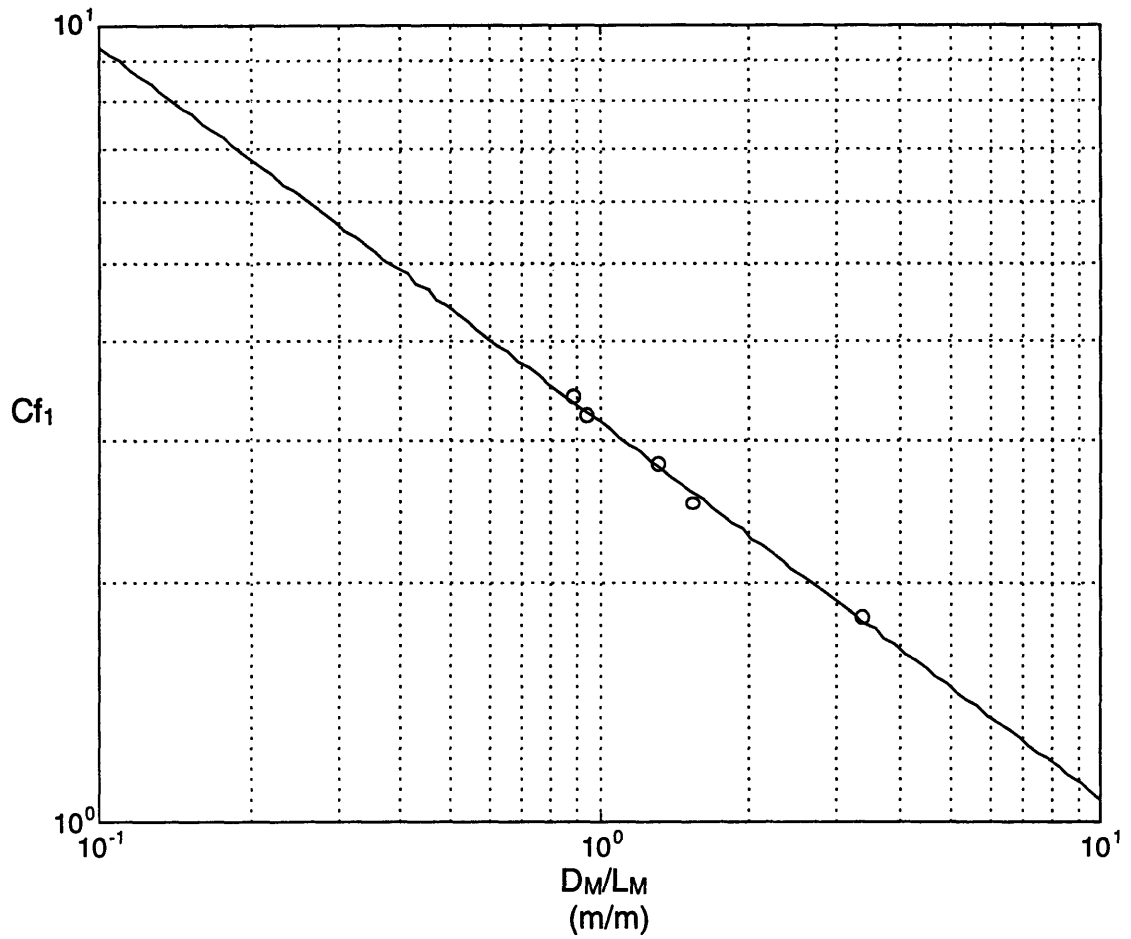


Figure D8. Experimental relationship between  $Cf_1$  to  $D_M/L_M$ .

The experimental data points used to create Figure D8 are as follows:

- $D_M/L_M$  is [0.8869 0.9440 1.3020 1.5256 3.3333]
- $Cf_1$  is [3.4000 3.2000 2.8000 2.5000 1.8000]

Equation D25 describes the relationship between correction factor 1 and the magnet's diameter-to-length ratio.

$$\log_{10}(Cf_1) = -.4721 \log_{10}\left(\frac{D_M}{L_M}\right) + .4976 \cdot (D25)$$

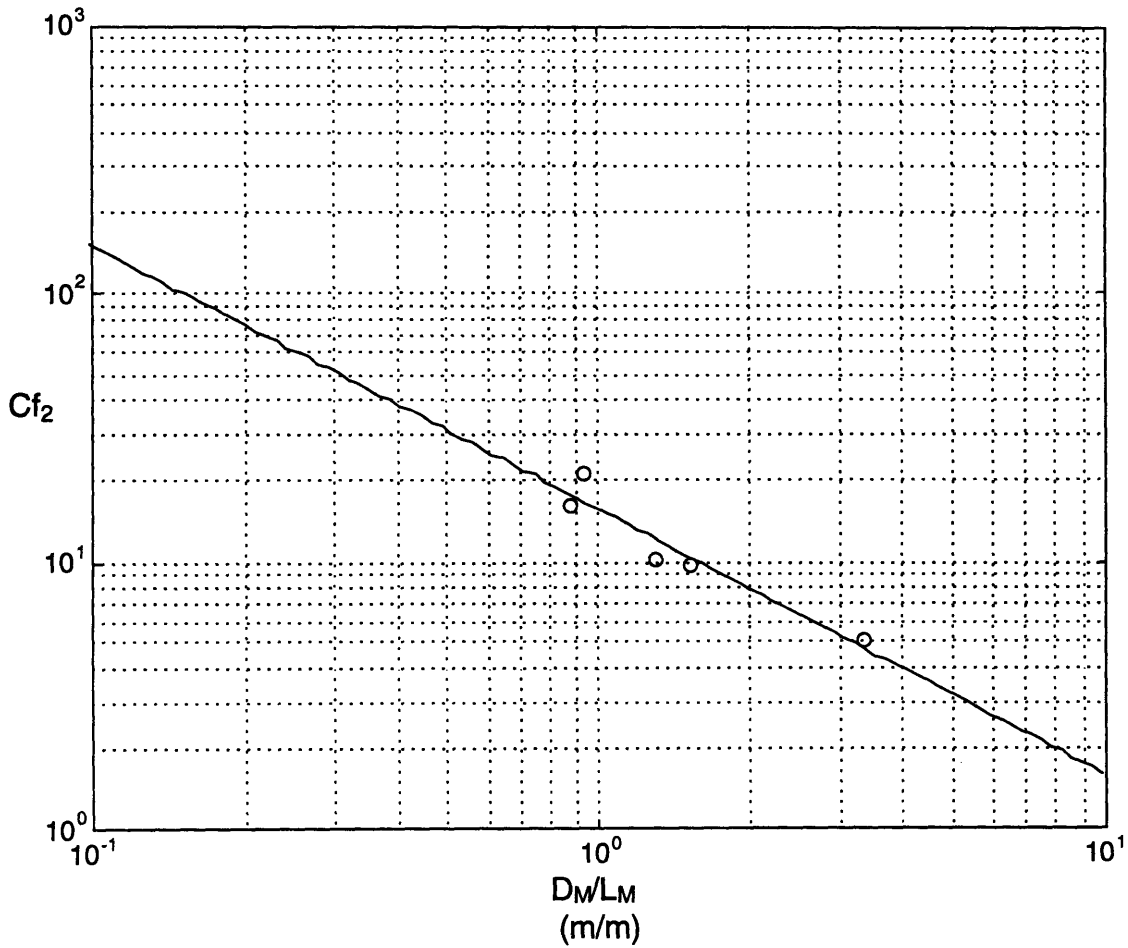


Figure D9. Experimental relationship between  $Cf_2$  to  $D_M/L_M$ .

The experimental data points used to create Figure D9 are as follows:

- $D_M/L_M$  is [0.8869 0.9440 1.3020 1.5256 3.3333]
- $Cf_2$  is [16.000 21.000 10.000 9.5000 5.0000]

Equation D26 describes the relationship between correction factor 2 and the magnet's diameter-to-length ratio.

$$\log_{10}(Cf_2) = -.9883 \log_{10}\left(\frac{D_M}{L_M}\right) + 1.1876 \quad (D26)$$

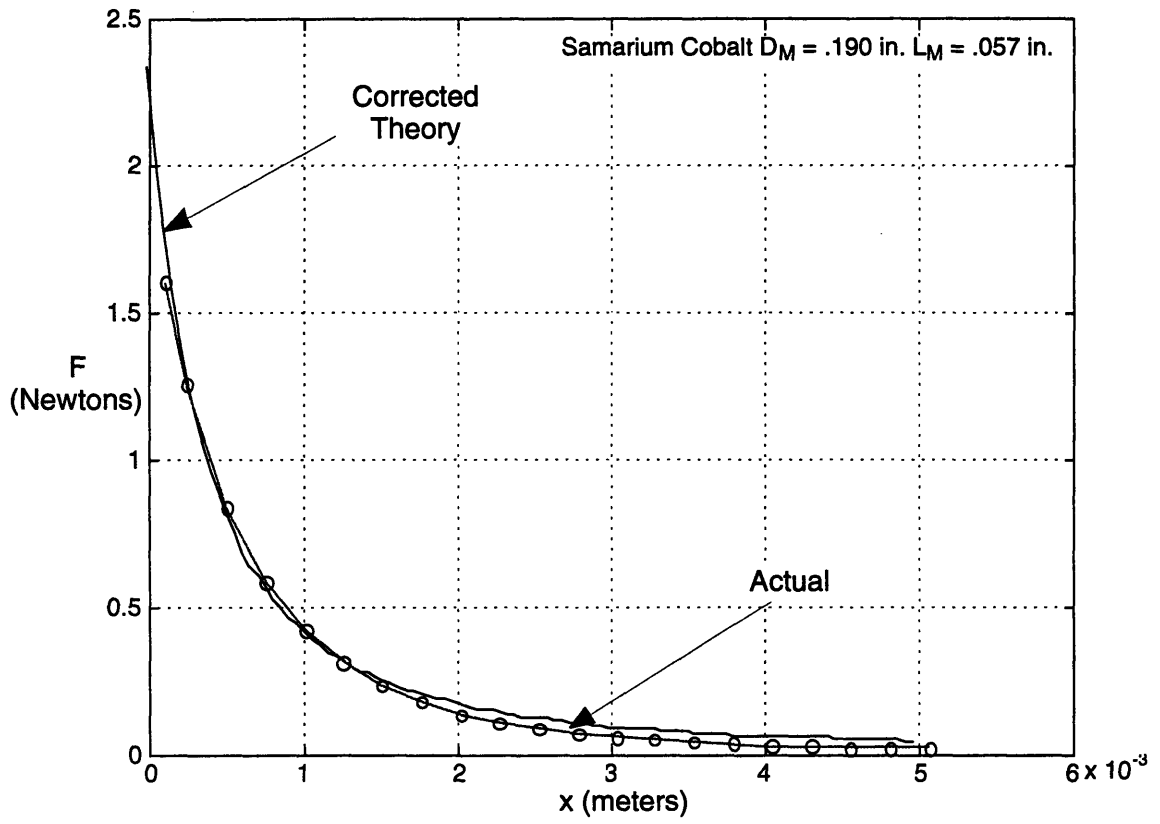


Figure D10. Corrected force-gap curves for Samarium Cobalt.

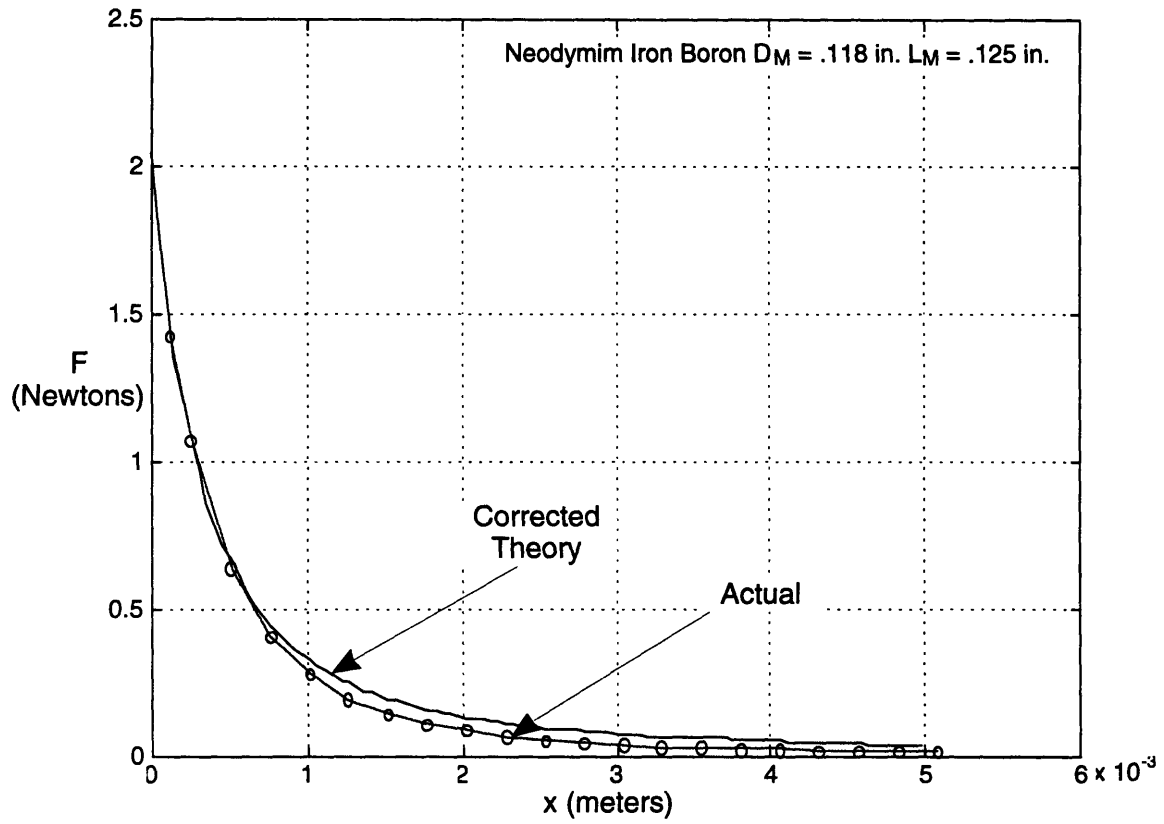


Figure D11. Corrected force-gap curves for Neodymium Iron Boron.

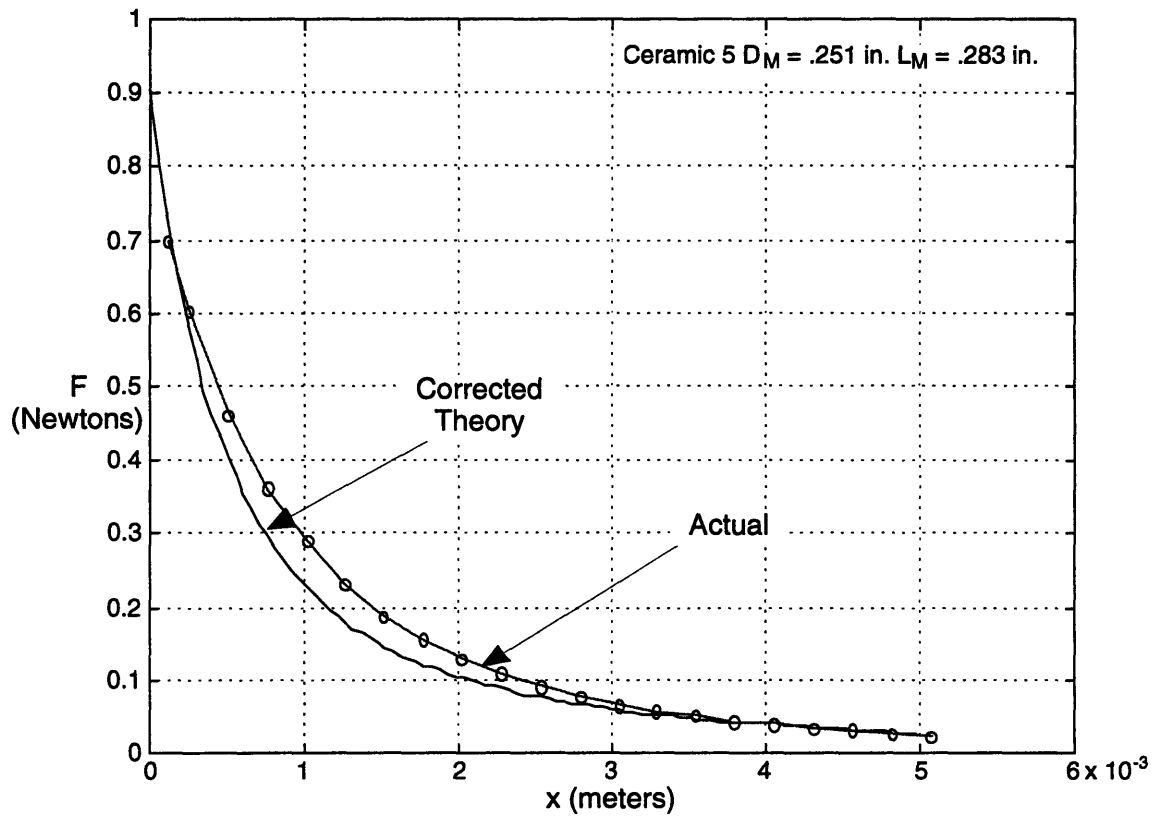


Figure D12. Corrected force-gap curves for Ceramic 5.

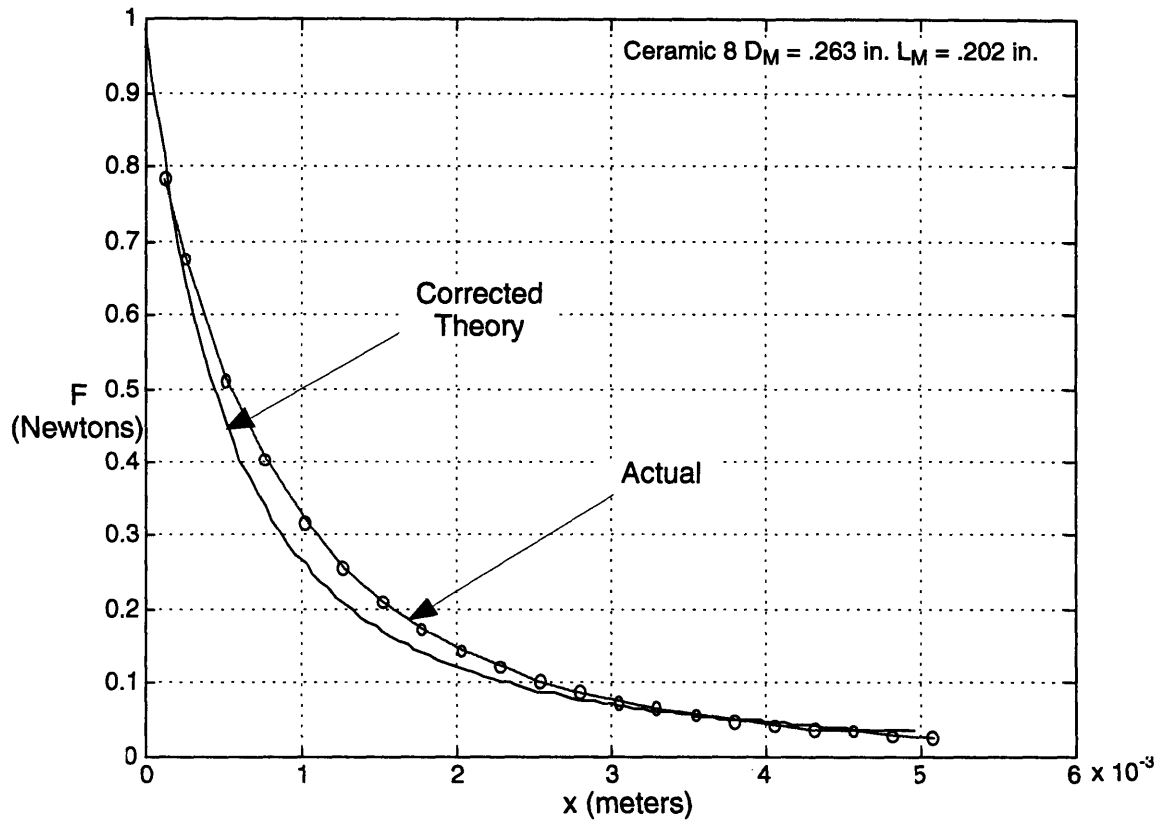


Figure D13. Corrected force-gap curves for Ceramic 8.

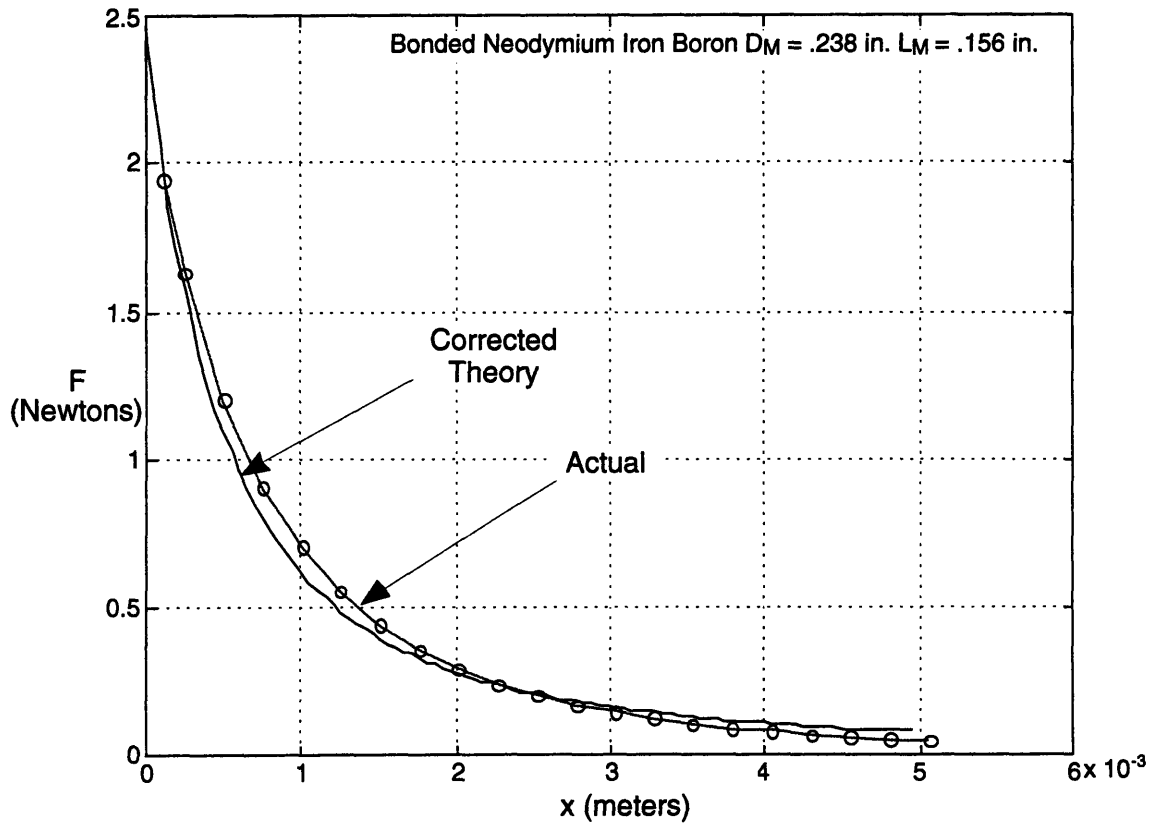


Figure D14. Corrected force-gap curves for Bonded Neodymium Iron Boron.

## **Appendix E: Permanent Magnet Experiments and Results**

As permanent magnets were pulled away from a steel block, the resulting force was recorded at corresponding normal distances between the steel block and the permanent magnet. This experiment obtained curves relating force to distance for the Ceramic, Samarium Cobalt, Neodymium Iron Boron, and Bonded Neodymium Iron Boron permanent magnets. This appendix contains three sections. In Section E.1, an illustration of the experimental apparatus and a description of the materials are given. In Section E.2, the experimental procedure is presented. In Section E.3, the experimental results are presented, along with the appropriate tables and curves.

E.1 *Experimental Materials and Apparatus*

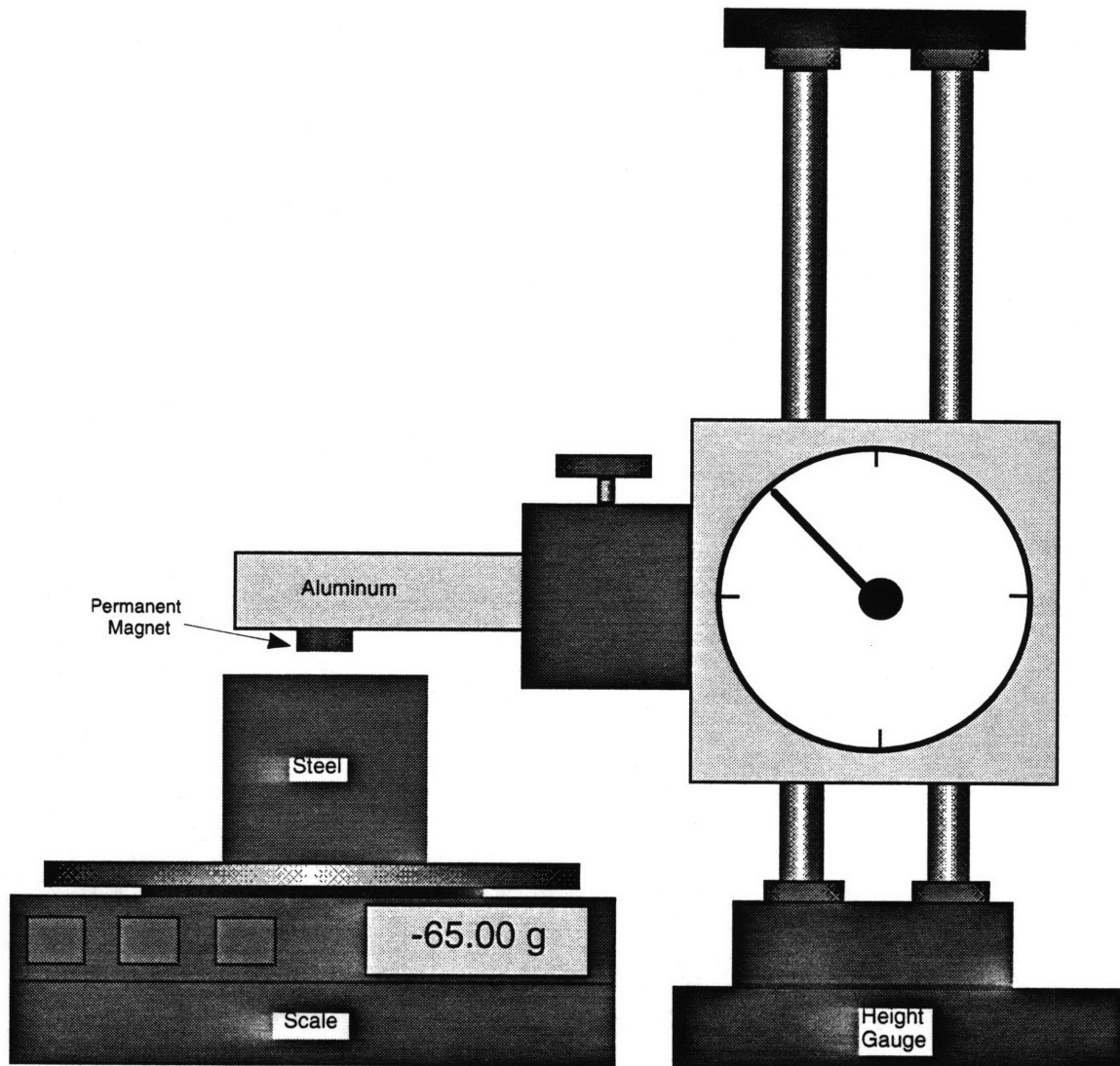


Figure E1. Experimental apparatus used for testing permanent magnets.

Figure E1 shows the experimental apparatus used to obtain force-gap curves.

The following materials were used:

1. low-carbon-steel block.
2. Samarium Cobalt cylindrical magnet
  - Diameter .190 inches
  - Length .057 inches
3. Neodymium cylindrical magnet
  - Diameter .118 inches
  - Length .125 inches
4. Ceramic 5 cylindrical magnet
  - Diameter .251 inches
  - Length .283 inches
5. Ceramic 8 cylindrical magnet
  - Diameter .263 inches
  - Length .202 inches
6. A Bonded Neodymium Iron Boron magnet
  - Diameter .238 inches
  - Length .156 inches

The following tools were used:

1. calibrated digital scale (+/- .005 grams)
2. calibrated dial height gauge (+/- .0005 inches)
3. calibrated digital caliper (+/- .0005 inches)

## **E.2 *Experimental Procedure***

1. Set digital scale, with low-carbon-steel block, to zero.
2. Attach permanent magnet to aluminum bar of the height gauge.
3. Using the height gauge, lower magnet until contact is made with the top of the low-carbon-steel block.
4. Set height gauge to zero.
5. Raise magnet .200 inches from the top of the low-carbon-steel block and record the scale reading (magnetic pulling force).
6. Lower magnet .010 inches and record the scale reading.
7. Repeat step 6 until the magnet is .010 inches above steel block.
8. Lower magnet to .005 inches above steel block and record scale reading.
9. Repeat steps 1-8 with each permanent magnet.

### E3. *Experimental Results*

Magnet Material	Samarium Cobalt	Neodymium Iron Boron	Ceramic 5	Ceramic 8	Bonded Neodymium Iron Boron
Diameter (inches)	0.190	0.118	0.251	0.263	0.238
Length (inches)	0.057	0.125	0.283	0.202	0.156
Air Gap (inches)	Force (grams)	Force (grams)	Force (grams)	Force (grams)	Force (grams)
0.200	1.23	0.66	2.15	2.39	3.98
0.190	1.43	0.77	2.43	2.70	4.59
0.180	1.70	0.91	2.76	3.06	5.29
0.170	2.00	1.08	3.14	3.51	6.15
0.160	2.40	1.27	3.63	4.02	7.09
0.150	2.90	1.53	4.13	4.64	8.26
0.140	3.45	1.85	4.80	5.39	9.63
0.130	4.21	2.28	5.61	6.29	11.29
0.120	5.16	2.82	6.49	7.37	13.42
0.110	6.39	3.56	7.59	8.66	15.95
0.100	8.05	4.54	8.93	10.16	19.25
0.090	10.21	5.84	10.65	12.07	23.43
0.080	13.18	7.64	12.86	14.36	28.80
0.070	17.36	10.07	15.50	17.28	35.66
0.060	23.00	13.72	18.80	21.08	44.22
0.050	30.96	18.95	23.14	25.76	56.10
0.040	42.22	27.22	29.12	32.14	71.02
0.030	58.94	40.90	36.60	40.73	91.44
0.020	84.79	64.46	46.55	51.93	121.79
0.010	127.22	108.35	61.12	68.65	165.66
0.005	162.85	145.13	70.93	79.75	197.62

Table E1. Experimental force-gap results for permanent magnets.

Table E1 displays the experimental results which are used to create Figures E2-E6. The curves in these figures plot the relationship between the magnetic force of each magnetic material tested, and the air gap measured in each test. These curves are used in Appendix D to determine the necessary correction factors for simulating force-gap curves.

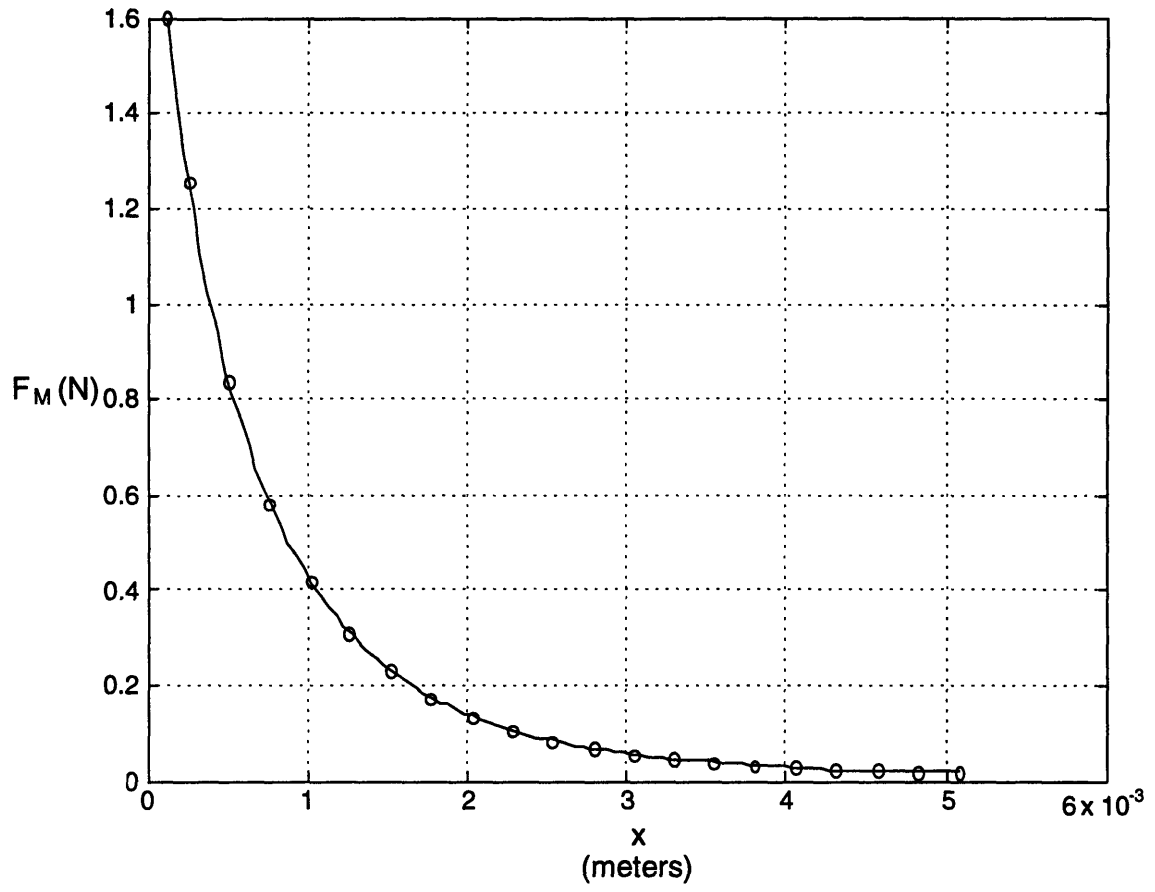


Figure E2. Experimental force-gap curve for Samarium Cobalt.

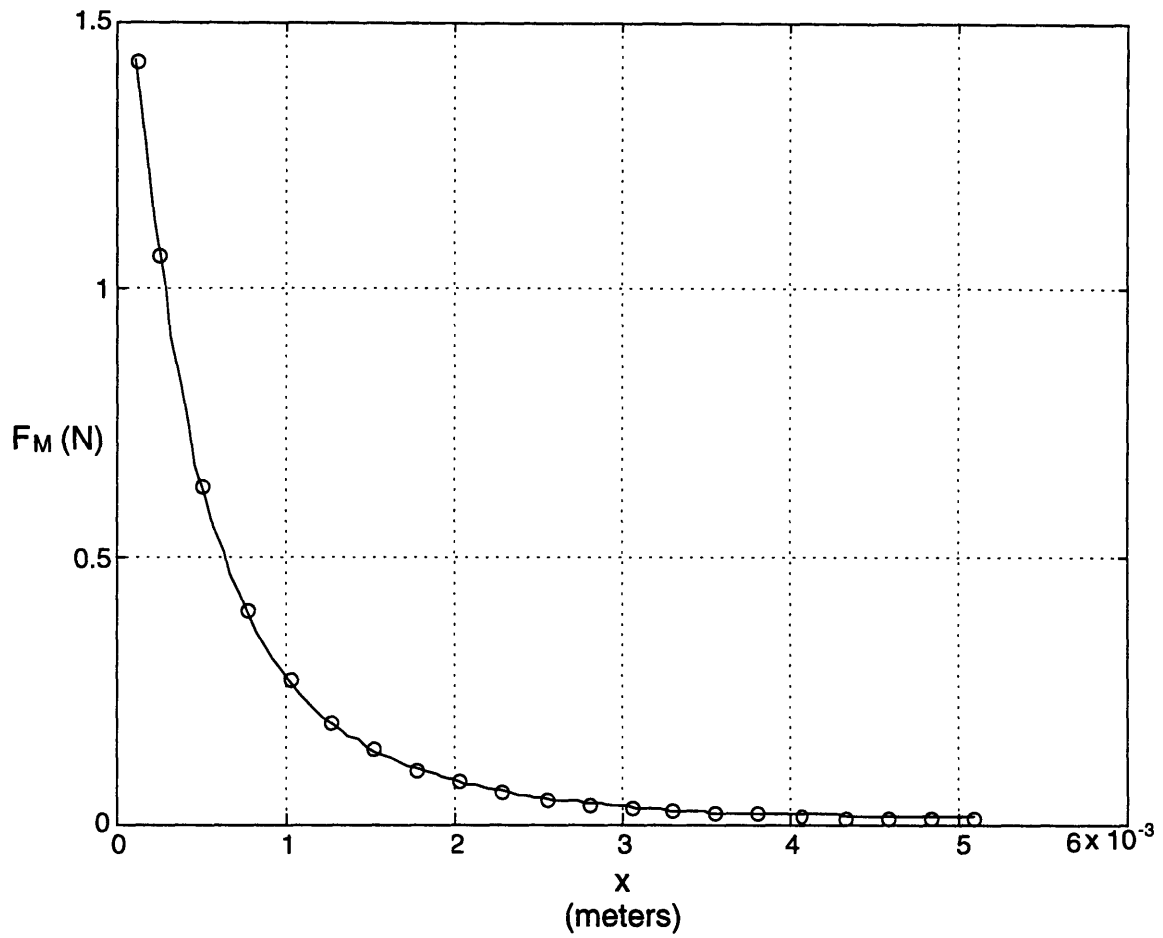


Figure E3. Experimental force-gap curve for Neodymium Iron Boron.

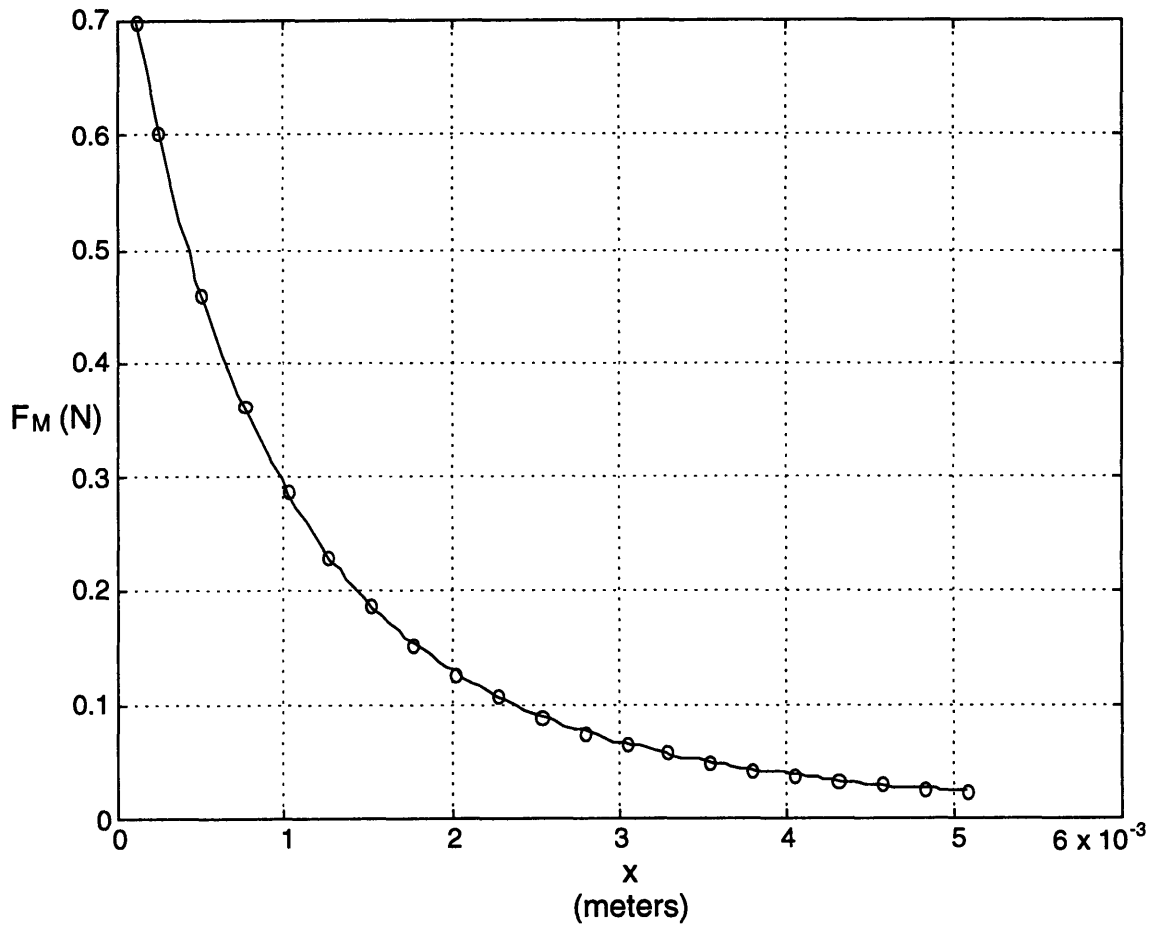


Figure E4. Experimental force-gap curve for Ceramic 5.

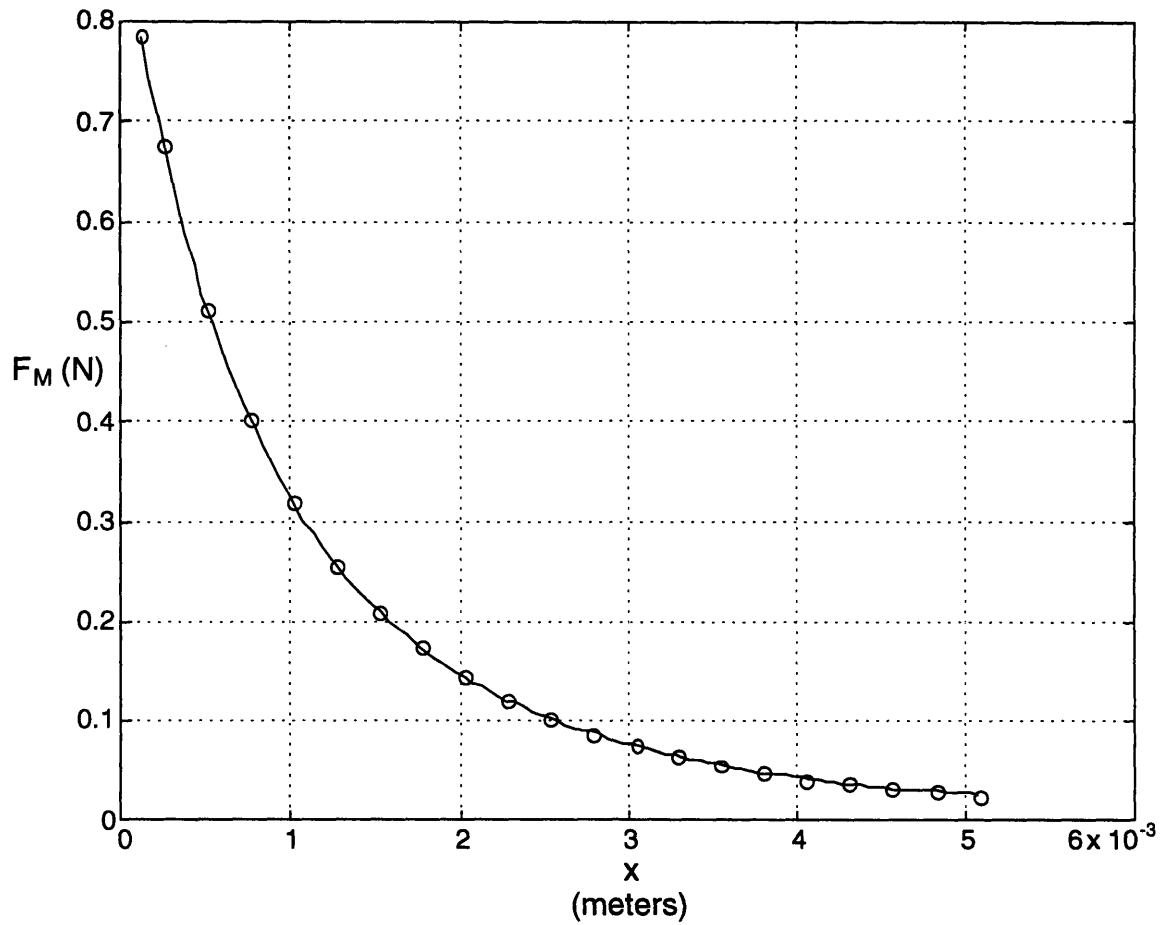


Figure E5. Experimental force-gap curve for Ceramic 8.

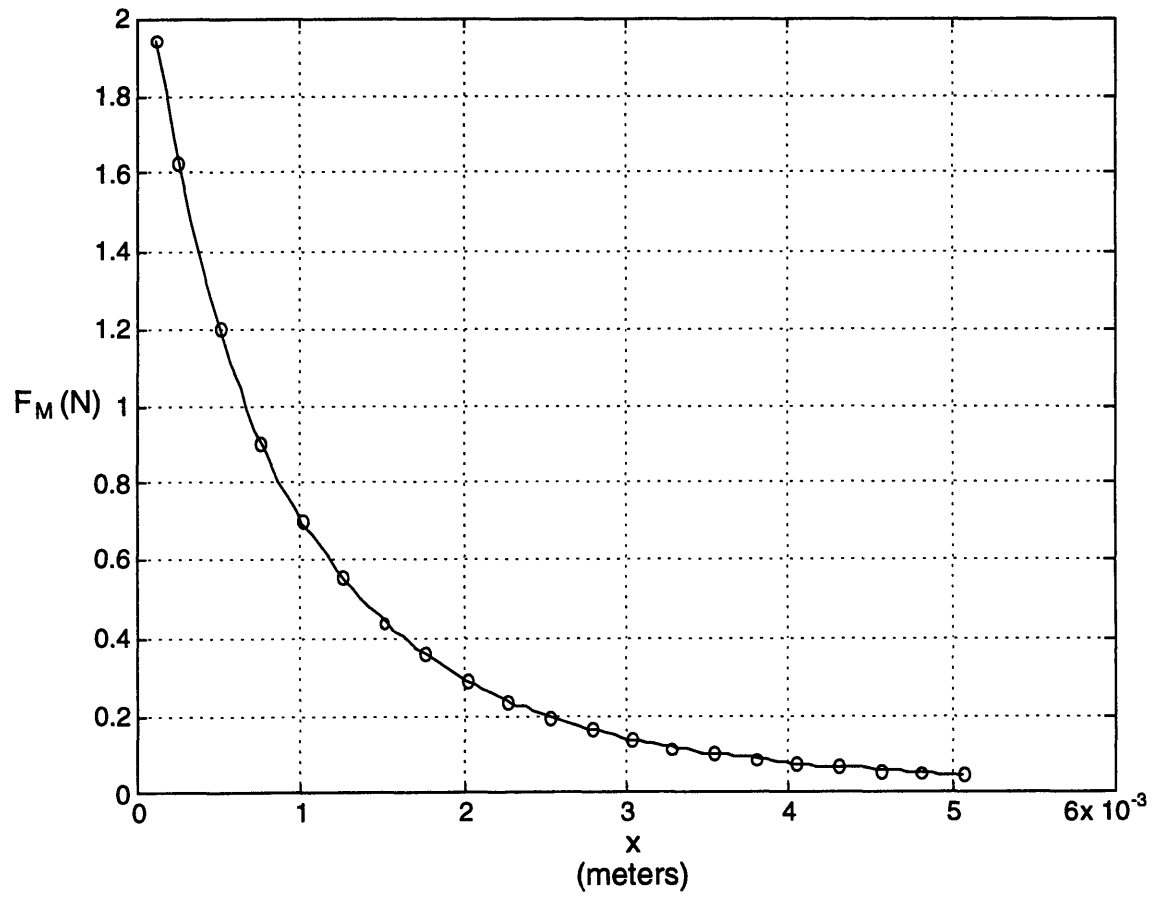


Figure E6. Experimental force-gap curve for Bonded Neodymium Iron Boron.

## Bibliography

Baz, A., Iman, K. and McCoy, J., 1990, "The Dynamics of Helical Shape Memory Actuators," *Journal of Intelligent Materials Systems and Structures*, 1:105-33 (1990).

Campbell, P., 1994, *Permanent Magnet Materials and Their Application*, Cambridge University Press, Great Britain, (1994).

Fitzgerald, A.E., Kingsley C.Jr., and Umans, S., 1990, *Electric Machinery*, McGraw-Hill Book Co., New York, pp. 1 - 146 (1990 fifth edition).

Gilbertson, R.G., 1994, *Muscle Wires Project Book*, Mondo-tronics, California, part 2 pp. 1-14 (1994). X

Liang, C., Rogers, C.A., 1990, "One-Dimensional Thermomechanical Constitutive Relations for Shape Memory Materials," *Journal of Intelligent Materials Systems and Structures*, 1:207-34 (1990).

Liang, C., Rogers, C.A., 1992, "Design of Shape Memory Alloy Actuators," *Journal of Mechanical Design*, 114:223-30 (1992). ✓

Lim, T.J., McDowell, D.L., 1994, "Degradation of an Ni-Ti alloy during cyclic loading," *Proceedings of The International Society of Optical Engineering for Smart Structures and Materials in Orlando, FL* (February 14-16, 1994), 2189:326-41 (1994).

Livingston, J.D., 1996, *Driving Force : The Natural Magic of Magnets*, Harvard University Press, Cambridge, Massachusetts, and London, England, (1996).

Malafeew, E., Vick, B., Liang, C., Rogers, C.A., 1992, "Distributed Electro-Thermo-Mechanical Analysis of Shape Memory Alloy Actuators," *Proceedings of the Conference on Recent Advances in Adaptive and Sensory Materials and Their Applications in Blacksburg, VA* (April 27-29, 1992), pp. 94-104 (1992).

McCaig, M., 1977, *Permanent Magnets in Theory and Practice*, John Wiley and Sons, Inc., New York, pp. 181-219 (1977).

Moskowitz, L.R., 1995, *Permanent Magnet Design and Application Handbook*, Krieger Publishing Company, Florida, (1995 second edition).

Parker, R.J., Studders, R.J., 1962, *Permanent Magnets and Their Application*, John Wiley and Sons, Inc., New York, pp. 101-209 (1962).

Thoma, P.E., Blok, A.M., Kao, M., 1992, "Pushing the Limit to Achieve NiTi SMA Actuating Members That are Dimensionally Stable and Have High Transformation Temperatures," *Shape Memory Materials and Phenomena-Fundamental Aspects and Applications, Materials Research Society Meeting in Boston, MA* (December 3-5, 1991), 246:321-30 (1992).

Thoma, P.E., Kao, M. and Schmitz, D.M., 1995, U.S. Patent 5,419,788, "Extended Life SMA Actuator," (1995).

Wayman, C.M., 1993, "Shape Memory Alloys," *MRS Bulletin/ Materials Research Society*, 18:4:49-56 (1993).

Zhang, C., Zee, R.H. and Thoma, P.E., 1996, "Development of Ni-Ti Based Shape Memory Alloys for Actuation and Control," *Proceedings of IECEC 96, 31st Intersociety Energy Conversion Engineering Conference in Washington, DC* (August 11-16, 1996), pp. 239-44 (1996).

6485.48